The evolution of strained turbulent plane wakes

By MICHAEL M. ROGERS

NASA Ames Research Center, Moffett Field, CA 94035, USA

Direct numerical simulations of ten turbulent time-evolving strained wakes have been generated using a pseudo-spectral numerical method. In all the simulations, the strain was applied to the same (previously generated) initial developed self-similar wake flow field. The cases include flows in which the wake is subjected to various orientations of the applied mean strain, including both plane and axisymmetric strain configurations. In addition, for one particular strain geometry, cases with differing strain rates were considered. Although classical self-similar analysis does yield a self-similar solution for strained wakes, this solution does not describe the observed flow evolution. Instead, the wake mean velocity profiles evolve according to a different 'equilibrium similarity solution', with the strained wake width being determined by the straining in the inhomogeneous cross-stream direction. Wakes that are compressed in this direction eventually exhibit constant widths, whereas wakes in cases with expansive cross-stream strain ultimately spread at the same rate as the distortion caused by the applied strain. The shape of the wake mean velocity deficit profile is nearly universal. Although the effect of the strain on the mean flow is pronounced and rapid, the response of the turbulence to the strain occurs more slowly. Changes in the turbulence intensity cannot keep pace with changes in the mean wake velocity deficit, even for relatively low strain rates.

1. Introduction

The effects of large-scale straining on turbulence have long been of interest. Early experiments designed to study isotropic turbulence led to the discovery that straining, applied to a flow by wind tunnel contractions, could significantly alter grid turbulence anisotropy. In order to more fully understand the effects of straining, experiments were devised to examine the impact of uniform straining on homogeneous grid turbulence. Townsend (1954) used a duct of constant cross-sectional area (after accounting for boundary layer growth) to study the impact of uniform plane strain on grid turbulence for total strains of up to 4. He compared the observed behaviour with the predictions of rapid distortion theory and found that this linear theory predicted the initial response of the turbulence to strain fairly well. The strain resulted in a slower turbulence decay, with the velocity component in the direction of compression being especially amplified relative to its value in the unstrained flow, while that in the direction of expansion decayed more rapidly. Similar results were observed by Tucker & Reynolds (1968) and Marechal (1972), who achieved total strains of 6.0 and 13.3, respectively, in their experiments. Unlike the results of Townsend (1954), however, their data suggested continued change of the Reynolds stress anisotropies rather than asymptotic structural equilibrium. Other strain configurations, such as

axisymmetric contraction (Uberoi 1956; Reynolds & Tucker 1975) and axisymmetric expansion (Reynolds & Tucker 1975) have also been investigated.

The impact of uniform irrotational straining on inhomogeneous flows has also been of interest. Reynolds (1962) used the distorting wind tunnel of Townsend (1954) to study the effect of a uniform and constant plane strain on the wakes of three circular cylinders of different diameters, placed at various streamwise locations relative to the distorting tunnel inlet. The primary goal of these experiments was to assess whether a mathematically derived self-similar solution was achieved in practice. The distorting section was placed such that the wakes were compressed in the cross-stream direction and expanded along their span. Reynolds (1962) felt that his data were consistent with self-similar evolution in some cases, depending on the organization of the turbulence at the point where the strain was applied and the relative importance of the shear and strain turbulence production terms. Later, however, Keffer (1965) repeated these experiments with more detailed turbulence measurements and concluded that a self-similar evolution was never observed. Keffer (1967) did similar experiments but changed the orientation of the distorting duct so as to achieve strain of the opposite sign. A similar strain configuration, but with non-negligible streamwise straining, was employed by Elliott & Townsend (1981). Self-similar evolution was not observed in these two experiments either.

Townsend (1954) selected his tunnel geometry in an attempt to produce the spatially evolving analogue of a time-evolving flow undergoing constant and uniform straining. Although well-suited for numerical simulation, time-evolving homogeneous flows are difficult to set up experimentally. Instead, experimentalists trade the strict streamwise inhomogeneity of the time-evolving problem for a statistically stationary spatially evolving flow with weak (hopefully negligible) streamwise inhomogeneity. The temporal evolution is replaced by a spatial evolution via a convective velocity down the experimental wind tunnel. For straining in a plane normal to the mean flow direction, as strived for in the above experiments, the convective velocity should be constant and the streamwise pressure gradient zero. In practice, there is streamwise variation in the mean streamwise velocity near the inlet and exit of the distorting duct, at least in part as a result of flow separation at these locations. Significant streamwise variations in the convective velocity are associated with local streamwise pressure gradients (as given by the Bernoulli equation) and cause departures from the idealized problem.

Streamwise pressure gradients in spatially evolving flows can be cast as streamwise strains in their temporally evolving analogues. In fact, other forms of 'strain', besides those in planes normal to the flow direction and constant in time, may be more closely related to problems of practical interest. Research on wakes in adverse pressure gradients has been of particular interest to the aircraft industry because of the occurrence of such flows in multi-component airfoils designed to produce high lift (see, for example, Smith 1975). Because of this, many experiments have been performed with this particular application in mind. Zhou & Squire (1985) studied not only wake development in an adverse pressure gradient, but also the wake's interaction with a nearby turbulent boundary layer. Hill, Schaub & Senoo (1963) and Hoffenberg, Sullivan & Schneider (1995) demonstrated that strong enough adverse pressure gradients can cause the mean wake velocity deficit to increase in magnitude, even to the point of causing local flow reversal or 'wake bursting', which limits the maximum lift obtainable by high-lift airfoils.

Several other experimental studies have investigated the impact of streamwise pressure gradients on the evolution of plane wakes. By 'appropriately tailoring' adverse

pressure gradients to have a power-law dependence on the streamwise coordinate, Gartshore (1967) was able to generate two 'nearly self-preserving' wakes that spread linearly with downstream distance. Narasimha & Prabhu (1972) and Prabhu & Narasimha (1972) studied the response of plane wakes to 'nearly impulsive' pressure gradients (favourable, adverse, and combinations of the two), as well as the ensuing 'slow relaxation' to equilibrium after the pressure gradient was removed (note, however, that the experimental results of Wygnanski, Champagne & Marasli (1986) and the computational results of Ghosal & Rogers (1997) and Moser, Rogers & Ewing (1998) suggest that a universal equilibrium may not exist). Narasimha & Prabhu concluded that such wakes did not follow their derived self-similar solution when the pressure gradient was not small. Instead they found that while the pressure gradient was applied, the turbulence responded to it as if to a sudden distortion, at least qualitatively.

All these experiments on wakes in pressure gradients have rather arbitrary streamwise pressure distributions, in some cases also poorly documented, making direct comparison with the simulations presented here difficult. By using a wind tunnel with adjustable sidewalls, Liu, Thomas, & Nelson (1999) examined the evolution of plane wakes in constant streamwise pressure gradients, both adverse and favourable. In this more fundamental model problem, the effects of a changing pressure gradient have been eliminated. Although not equivalent to the constant-strain-rate cases considered here (see Appendix A), the distorting tunnel geometry used by Liu *et al.* (1999) for some of their constant-pressure-gradient flows is not far from that required for constant strain rate and similarities between these two cases are apparent.

Other examples of 'strained' free shear layers have also been studied experimentally. These include strained mixing layers (Keffer *et al.* 1978), wakes subjected to curvature as well as pressure gradients (Nakayama 1987 and references therein), and wakes and mixing layers subjected to cross-plane shear (Atsavapranee & Gharib 1994, 1997, Nayeri *et al.* 1996 and Beharelle *et al.* 1996) among others.

Despite the practical relevance of strained free shear flows, there is a need for detailed data on these flows that is of general utility. The issue of whether such flows do or can evolve self-similarly still needs further clarification. If, as several experiments indicate, self-similar evolution is not typically observed, then an understanding of how the flows do respond to imposed strain needs to be developed. This should include not only the impact on turbulent statistics, but also on flow structure. If the flow evolution is not consistent with the classical self-similar solution, can a more general equilibrium similarity state describe the flow evolution?

Most inhomogeneous free shear flows of practical interest are spatially developing. However, numerical simulations of the corresponding time-evolving flows can achieve higher Reynolds numbers and more fully developed turbulence while using cleaner boundary conditions than those of the spatially evolving problem (e.g. Rogers & Moser 1994 and Moser *et al.* 1998). Although the temporally evolving problem possesses symmetries not found in the corresponding spatially evolving flow, the vortex dynamics of these two flows are similar (e.g. Rogers, Moser & Buell 1990). Because of these advantages, the time-evolving problem is chosen for the numerical simulations in this work.

Time-evolving plane wakes subjected to constant strain rates are conceptually the simplest form of strained free shear layer. They lack the complicating effects of streamwise inhomogeneity and time-varying strain rate, but maintain the fundamental character of strained free shear layers. Turbulence is produced both by shear and by strain, the relative importance of these two mechanisms not necessarily being the

same throughout the flow evolution. These simplified flows are well-suited for direct numerical simulations. Such simulations are in turn ideal for providing a complete description of the turbulence and precise control of the initial conditions. Unlike the experimental situation, the strain in the computations can be applied instantly, without local flow separation and other irregularities. The goal of the current investigation is to study the response of a developed self-similar plane wake to suddenly imposed strains of various orientations and magnitudes and to compare this response to that predicted by self-similar analysis. All terms in the Reynolds stress balance equations have been computed to provide a database helpful for turbulence model development and flow visualization has been employed to understand the impact of strain on the wake structure.

In §2 the governing equations for the time-evolving strained wake are developed and self-similar solutions of these equations are derived. Section 3 contains a description of the numerical method used to generate the numerical simulations (the mathematical details being relegated to an appendix), along with a description of the cases that are described in this paper. Results derived from the simulated flow fields, including flow visualization, and a comparison with results of experimental work in similar flows are given in §4. Conclusions are summarized in §5. Three appendices, which include the mathematical details of the numerical method, an exact solution for laminar strained free shear layers, and additional turbulence statistics from the simulated flows (anisotropy measures, terms in the Reynolds stress balance equation) are available from the JFM Editorial Office at Cambridge rather than being included here.

2. The strained time-evolving wake

2.1. *The governing equations*

The governing equations for the strained plane wakes simulated here are the incompressible Navier–Stokes equations given by

$$\frac{\partial U_i}{\partial x_i} = 0, \tag{2.1}$$

$$\frac{\partial U_i}{\partial t} + U_j \frac{\partial U_i}{\partial x_j} + \frac{1}{\rho} \frac{\partial P}{\partial x_i} = v \frac{\partial^2 U_i}{\partial x_j \partial x_j}, \tag{2.2}$$

where U_i represents the ith component of the velocity vector, P is the pressure, ρ the constant density, and v the constant kinematic viscosity. Decomposing the flow into mean ($\overline{U_i}$ and $\bar{P}$) and fluctuating (u_i' and p') parts, substituting into the Navier–Stokes equations, and averaging, yields the mean flow equations

$$\frac{\partial \overline{U_i}}{\partial x_i} = 0, \tag{2.3}$$

$$\frac{\partial \overline{U_i}}{\partial t} + \overline{U_j} \frac{\partial \overline{U_i}}{\partial x_j} + \frac{\partial \overline{u_i' u_j'}}{\partial x_j} + \frac{1}{\rho} \frac{\partial \bar{P}}{\partial x_i} = v \frac{\partial^2 \overline{U_i}}{\partial x_j \partial x_j}. \tag{2.4}$$

The time-evolving wakes studied here develop in time and are statistically homogeneous in the streamwise x_1 and spanwise x_3 directions, i.e. there are no spatial gradients of turbulent statistics in these coordinate directions. The cross-stream x_2 direction is inhomogeneous and thus mean statistics depend on the x_2 location. For a time-evolving plane wake, the mean velocity deficit is given by $\overline{U_1} = \overline{U_1}(x_2, t)$. The addition of a spatially uniform (but possibly varying in time) mean strain to the

mean velocity field adds another component given by $\partial \overline{U}_i / \partial x_j = a_{ij}(t)$. Considering irrotational mean strains where only a_{11}, a_{22}, and a_{33} may be non-zero, and using x, y, z, $\overline{U}$, $\overline{V}$, and $\overline{W}$ for x_1, x_2, x_3, $\overline{U}_1$, $\overline{U}_2$, and $\overline{U}_3$ (these two notations will be used interchangeably here), the mean velocity field is given by

$$\overline{U} = a_{11}(t)x + \overline{U}_w(y, t), \qquad (2.5a)$$

$$\overline{V} = a_{22}(t)y, \qquad (2.5b)$$

$$\overline{W} = a_{33}(t)z, \qquad (2.5c)$$

where the subscript w is used to denote the wake component of the mean velocity. Note that for the computations described here, the wake component of the spanwise velocity $\overline{W}_w$ is not forced to be zero, although it does remain small throughout all the computations. Given a larger statistical sample (or a bigger computational domain) this average would approach zero. In order to compare to this ideal case, the small 'average' spanwise velocity is considered here to be a fluctuation around a 'true' average of zero.

By substituting the above mean velocity field into the Navier–Stokes equations and taking advantage of statistical homogeneity in the x- and z-directions, the following mean field equations are obtained (with u', v', and w' being used in place of u'_1, u'_2, and u'_3)

$$\frac{\partial \overline{U}}{\partial x} + \frac{\partial \overline{V}}{\partial y} + \frac{\partial \overline{W}}{\partial z} = a_{11}(t) + a_{22}(t) + a_{33}(t) = 0, \qquad (2.6)$$

$$\frac{\partial a_{11}}{\partial t}x + \frac{\partial \overline{U}_w}{\partial t} + [a_{11}(t)x + \overline{U}_w]a_{11}(t) + a_{22}(t)y\frac{\partial \overline{U}_w}{\partial y} + \frac{\partial \overline{u'v'}}{\partial y} + \frac{1}{\rho}\frac{\partial \bar{P}}{\partial x} = v\frac{\partial^2 \overline{U}_w}{\partial y^2}, \quad (2.7a)$$

$$\frac{\partial a_{22}}{\partial t}y + a_{22}^2(t)y + \frac{\partial \overline{v'^2}}{\partial y} + \frac{1}{\rho}\frac{\partial \bar{P}}{\partial y} = 0, \qquad (2.7b)$$

$$\frac{\partial a_{33}}{\partial t}z + a_{33}^2(t)z + \frac{\partial \overline{v'w'}}{\partial y} + \frac{1}{\rho}\frac{\partial \bar{P}}{\partial z} = 0. \qquad (2.7c)$$

The last equation can be further simplified by noting that the Reynolds stress $\overline{v'w'}$ is zero because of flow symmetry. In the absence of a wake ($\overline{U}_w = 0$), the pressure field for the corresponding laminar strain problem is given by

$$P_s = P_0 - \frac{\rho}{2}\left[\left(\frac{da_{11}}{dt} + a_{11}^2\right)x^2 + \left(\frac{da_{22}}{dt} + a_{22}^2\right)y^2 + \left(\frac{da_{33}}{dt} + a_{33}^2\right)z^2\right], \qquad (2.8)$$

where P_0 is the pressure at the origin of the coordinate system. Defining $\bar{P}_w = \bar{P} - P_s$ and substituting into equations (2.7) yields

$$\frac{\partial \overline{U}_w}{\partial t} + a_{11}(t)\overline{U}_w + a_{22}(t)y\frac{\partial \overline{U}_w}{\partial y} + \frac{\partial \overline{u'v'}}{\partial y} + \frac{1}{\rho}\frac{\partial \bar{P}_w}{\partial x} = v\frac{\partial^2 \overline{U}_w}{\partial y^2}, \qquad (2.9a)$$

$$\frac{\partial \overline{v'^2}}{\partial y} + \frac{1}{\rho}\frac{\partial \bar{P}_w}{\partial y} = 0, \qquad (2.9b)$$

$$\frac{1}{\rho}\frac{\partial \bar{P}_w}{\partial z} = 0. \qquad (2.9c)$$

All terms in these three equations depend only on y and t, implying that the pressure $\bar{P}_w$ can be at most linear in x. However, for the boundary conditions of this problem,

the integrated (across the wake from $y = -\infty$ to $y = \infty$) mean momentum equation (2.9a) cannot balance unless $\bar{P}_w$ does not depend on x. Thus, for the flows considered here, $\partial \bar{P}_w / \partial x = 0$ and $\bar{P}_w = -\rho \overline{v'^2}$.

The time evolution of the area under the velocity deficit profile (proportional to the mass flux deficit) can be obtained by integrating equation (2.9a) from $y = -\infty$ to $y = \infty$. Defining

$$A_w(t) = \int_{-\infty}^{\infty} \overline{U}_w(y, t) \, dy, \tag{2.10}$$

taking advantage of both the vanishing Reynolds shear stress and wake mean velocity gradients at infinity, and noting that $\overline{U}_w$ decays faster than $1/y$ at large y, one can derive

$$A_w(t) = A_w^0 \exp \int_{t'=0}^{t'=t} [a_{22}(t') - a_{11}(t')] \, dt', \tag{2.11}$$

where $A_w^0 = A_w(t = 0)$. For the case of constant strain rate, this reduces to the simple exponential form

$$A_w(t) = A_w^0 e^{(a_{22} - a_{11})t}. \tag{2.12}$$

In the absence of strain, equation (2.11) reduces to the conservation of mass flux deficit for a time-evolving plane wake.

By subtracting the mean equations (2.3) and (2.4) from the full Navier–Stokes equations equations (2.1) and (2.2), the following equations governing the fluctuating velocity components are obtained (reverting to Cartesian tensor notation for compactness):

$$\frac{\partial u_i'}{\partial x_i} = 0, \tag{2.13}$$

$$\frac{\partial u_i'}{\partial t} + \overline{U}_j \frac{\partial u_i'}{\partial x_j} + u_j' \frac{\partial \overline{U}_i}{\partial x_j} + \frac{\partial u_i' u_j'}{\partial x_j} - \frac{\partial \overline{u_i' u_j'}}{\partial x_j} + \frac{1}{\rho} \frac{\partial p'}{\partial x_i} = \nu \frac{\partial^2 u_i'}{\partial x_j \partial x_j}. \tag{2.14}$$

Because of the mean strain, the second term in equation (2.14) has a coefficient on the fluctuating velocity derivative that has explicit dependence on the spatial coordinates x_i. The consequences of this for the numerical method are discussed in §3.1.

From the fluctuating equation (2.14), the equation for the evolution of the Reynolds stress tensor $R_{ij} = \overline{u_i' u_j'}$ can be derived:

$$\frac{\partial \overline{u_i' u_j'}}{\partial t} + \overline{U}_k \frac{\partial \overline{u_i' u_j'}}{\partial x_k} = - \left(\overline{u_i' u_k'} \frac{\partial \overline{U}_j}{\partial x_k} + \overline{u_j' u_k'} \frac{\partial \overline{U}_i}{\partial x_k} \right) - \frac{\partial \overline{u_i' u_j' u_k'}}{\partial x_k} + \overline{\frac{p'}{\rho} \left(\frac{\partial u_i'}{\partial x_j} + \frac{\partial u_j'}{\partial x_i} \right)}$$
$$- \frac{1}{\rho} \left(\frac{\partial \overline{p' u_i'}}{\partial x_j} + \frac{\partial \overline{p' u_j'}}{\partial x_i} \right) + \nu \frac{\partial^2 \overline{u_i' u_j'}}{\partial x_k \partial x_k} - 2\nu \overline{\frac{\partial u_i'}{\partial x_k} \frac{\partial u_j'}{\partial x_k}}. \tag{2.15}$$

Incorporating statistical homogeneity in x_1 and x_3 and the form of the mean velocity field (2.5) yields

$$\frac{\partial \overline{u_i' u_j'}}{\partial t} + a_{22}(t) x_2 \frac{\partial \overline{u_i' u_j'}}{\partial x_2} = \mathscr{P}_{ij} + \mathscr{T}_{ij} + \mathscr{W}_{ij} + \mathscr{V}_{ij} + \epsilon_{ij}, \tag{2.16}$$

where the production is given by

$$\mathscr{P}_{ij} = - \left(\overline{u_i' u_k'} \frac{\partial \overline{U}_j}{\partial x_k} + \overline{u_j' u_k'} \frac{\partial \overline{U}_i}{\partial x_k} \right), \tag{2.17}$$

the turbulent transport (both turbulent diffusion and pressure diffusion) by

$$\mathcal{T}_{ij} = -\frac{\partial}{\partial x_2} \left(\overline{u'_i u'_j u'_2} + \frac{1}{\rho}(\delta_{j2}\overline{p'u'_i} + \delta_{i2}\overline{p'u'_j}) \right), \tag{2.18}$$

the pressure–strain by

$$\mathcal{W}_{ij} = \overline{\frac{p'}{\rho} \left(\frac{\partial u'_i}{\partial x_j} + \frac{\partial u'_j}{\partial x_i} \right)}, \tag{2.19}$$

the viscous diffusion by

$$\mathcal{V}_{ij} = v \frac{\partial^2 \overline{u'_i u'_j}}{\partial x_2 \partial x_2}, \tag{2.20}$$

and the dissipation by

$$\epsilon_{ij} = -2v \overline{\frac{\partial u'_i}{\partial x_k} \frac{\partial u'_j}{\partial x_k}}. \tag{2.21}$$

The four non-zero production terms are

$$\mathcal{P}_{11} = -2a_{11}(t)\overline{u'^2} - 2\overline{u'v'}\frac{\partial \overline{U}_w}{\partial y}, \tag{2.22a}$$

$$\mathcal{P}_{22} = -2a_{22}(t)\overline{v'^2}, \tag{2.22b}$$

$$\mathcal{P}_{33} = -2a_{33}(t)\overline{w'^2}, \tag{2.22c}$$

$$\mathcal{P}_{12} = -(a_{11}(t) + a_{22}(t))\overline{u'v'} - \overline{v'^2}\frac{\partial \overline{U}_w}{\partial y}$$

$$= a_{33}(t)\overline{u'v'} - \overline{v'^2}\frac{\partial \overline{U}_w}{\partial y}. \tag{2.22d}$$

Note that the wake shear results in production of only $\overline{u'^2}$ and $\overline{u'v'}$, whereas the mean strain may, depending on the geometry of the strain, cause 'production' in any of the equations. Depending on the sign of the strain, these strain 'production' terms may actually decrease some of the Reynolds stresses rather than augment them. Twice the turbulent kinetic energy (per unit mass) is defined here as $q^2 = \overline{u'_i u'_i} = \overline{u'^2} + \overline{v'^2} + \overline{w'^2}$ and the dissipation rate of turbulent kinetic energy is denoted by $\epsilon = -\epsilon_{ii}/2$.

In all the simulations, the evolution of a passive scalar quantity is calculated along with the development of the hydrodynamic field. The governing equation for this passive scalar is given by

$$\frac{\partial T}{\partial t} + U_j \frac{\partial T}{\partial x_j} = \gamma \frac{\partial^2 T}{\partial x_j \partial x_j}, \tag{2.23}$$

where T is the passive scalar and γ is the molecular scalar diffusivity, which for all the simulations is chosen such that the Prandtl number $Pr = v/\gamma = 0.7$. Although many interesting scalar statistics can be computed from the scalar fields, up to this point the scalar has only been used for flow visualization, with the scalar marking the level of mixing between the two free streams ($T = 0$ below the wake and $T = 1$ above it).

2.2. Self-similarity

In the absence of strain, developed plane wakes are observed to evolve self-similarly. Such self-similar evolution was also observed in previous direct numerical simulations of plane wakes by Moser *et al.* (1998). Here we explore the possibility of self-similar

evolution for time-evolving strained plane wakes. The approach used is that developed by George (1989, 1995) and has been used previously for unstrained wakes by Moser *et al.* (1998). In §2.2.1 the classical self-similar solution, in which all terms in the governing equations except the viscous terms scale in the same way, is derived. Following this, in §2.2.2, more general equilibrium similarity solutions are sought. In these solutions, groups of terms in the governing equations combine together to scale like other groups or terms in the same equation. These more general similarity solutions exhibit more complex behaviour, such as the various Reynolds stresses scaling differently from each other and not necessarily like the square of the wake velocity deficit. Thus, unlike with the classical self-similar solution, the flow evolution is not characterized by a single velocity scale.

2.2.1. *Classical self-similarity*

Assuming that the wake mean velocity deficit profile can be described by a time-varying magnitude $U_s(t)$ and a characteristic profile shape of a specified width $\delta(t)$, it can be written as

$$\overline{U}_w(y,t) = -U_s(t)f(\eta), \qquad (2.24)$$

where $\eta = y/\delta(t)$ is the scaled cross-stream coordinate. Note that the velocity deficit goes to zero in the free streams in the time-evolving problem. Substituting into the definition of A_w (2.10) we have

$$A_w(t) = -U_s(t)\delta(t) \int_{-\infty}^{\infty} f(\eta)\,\mathrm{d}\eta \qquad (2.25)$$

and then from equation (2.11)

$$U_s(t)\delta(t) = U_s^0 \delta^0 \exp\left(\int_{t'=0}^{t'=t} [a_{22}(t') - a_{11}(t')]\,\mathrm{d}t'\right), \qquad (2.26)$$

where $U_s^0 = U_s(t=0)$ and $\delta^0 = \delta(t=0)$ are the values of U_s and δ at the virtual origin of the self-similar period required to match the observed evolution. Thus if the wake mean deficit profile is self-similar, the product of the deficit magnitude and the wake width must follow the above exponential evolution.

Substituting (2.24) into the mean momentum equation (2.9a) and defining $\overline{u'v'} = K_{12}(t)k_{12}(\eta)$ for the self-similar Reynolds shear stress profile yields

$$\left[\frac{U_s(t)}{\delta(t)}\frac{\mathrm{d}\delta}{\mathrm{d}t}\right]\eta\frac{\mathrm{d}f}{\mathrm{d}\eta} - \left[\frac{\mathrm{d}U_s}{\mathrm{d}t}\right]f(\eta) - [a_{11}(t)U_s(t)]f(\eta) - [a_{22}(t)U_s(t)]\eta\frac{\mathrm{d}f}{\mathrm{d}\eta}$$

$$+ \left[\frac{K_{12}(t)}{\delta(t)}\right]\frac{\mathrm{d}k_{12}}{\mathrm{d}\eta} = -\nu\left[\frac{U_s(t)}{\delta^2(t)}\right]\frac{\mathrm{d}^2 f}{\mathrm{d}\eta^2}, \quad (2.27)$$

where the bracketed terms contain all the time-dependent portions of the equation. Assuming none of the above terms is negligible, self-similarity will result if all the bracketed terms are proportional (it can also occur if a certain subset of the terms grow at a different rate but offset each other, as discussed later).

For complete self-similarity, all the terms in other derived transport equations must also exhibit self-similar behaviour (or they must be negligible in comparison to other terms in each equation). Here the Reynolds stress equation (2.16) will be examined to search for additional constraints on the possible self-similar evolution. Again reverting

to Cartesian tensor notation for compactness, and defining

$$\overline{u'_\alpha u'_\beta} = K_{\alpha\beta}(t)k_{\alpha\beta}(\eta), \tag{2.28a}$$

$$\mathcal{T}_{\alpha\beta} = -\frac{\partial}{\partial x_2}(Tr_{\alpha\beta}(t)tr_{\alpha\beta}(\eta)), \tag{2.28b}$$

$$\mathcal{W}_{\alpha\beta} = \Pi_{\alpha\beta}(t)\pi_{\alpha\beta}(\eta), \tag{2.28c}$$

and

$$\epsilon_{\alpha\beta} = D_{\alpha\beta}(t)d_{\alpha\beta}(\eta) \tag{2.28d}$$

(where there is no summation on repeated Greek indices†) the Reynolds stress transport equation (2.16) becomes

$$-\left[\frac{K_{\alpha\beta}(t)}{\delta(t)}\frac{\mathrm{d}\delta}{\mathrm{d}t}\right]\eta\frac{\mathrm{d}k_{\alpha\beta}}{\mathrm{d}\eta} + \left[\frac{\mathrm{d}K_{\alpha\beta}}{\mathrm{d}t}\right]k_{\alpha\beta} + [a_{22}(t)K_{\alpha\beta}(t)]\eta\frac{\mathrm{d}k_{\alpha\beta}}{\mathrm{d}\eta}$$

$$= \mathcal{P}_{\alpha\beta} - \left[\frac{Tr_{\alpha\beta}(t)}{\delta(t)}\right]\frac{\mathrm{d}tr_{\alpha\beta}}{\mathrm{d}\eta} + [\Pi_{\alpha\beta}(t)]\pi_{\alpha\beta}(\eta) - [D_{\alpha\beta}(t)]d_{\alpha\beta}(\eta) + v\left[\frac{K_{\alpha\beta}(t)}{\delta^2(t)}\right]\frac{\mathrm{d}^2k_{\alpha\beta}}{\mathrm{d}\eta^2}, \tag{2.29}$$

where $\mathcal{P}_{\alpha\beta}$ is given by

$$\mathcal{P}_{11} = -2[a_{11}(t)K_{11}(t)]k_{11}(\eta) + 2\left[\frac{K_{12}(t)U_s(t)}{\delta(t)}\right]k_{12}(\eta)\frac{\mathrm{d}f}{\mathrm{d}\eta}, \tag{2.30a}$$

$$\mathcal{P}_{22} = -2[a_{22}(t)K_{22}(t)]k_{22}(\eta), \tag{2.30b}$$

$$\mathcal{P}_{33} = -2[a_{33}(t)K_{33}(t)]k_{33}(\eta), \tag{2.30c}$$

$$\mathcal{P}_{12} = -[(a_{11}(t) + a_{22}(t))K_{12}(t)]k_{12}(\eta) + \left[\frac{K_{22}(t)U_s(t)}{\delta(t)}\right]k_{22}(\eta)\frac{\mathrm{d}f}{\mathrm{d}\eta}. \tag{2.30d}$$

Additionally, continuity imposes another constraint on the pressure–strain:

$$\mathcal{W}_{11} + \mathcal{W}_{22} + \mathcal{W}_{33} = 0 \tag{2.31a}$$

or

$$[\Pi_{11}(t)]\pi_{11}(\eta) + [\Pi_{22}(t)]\pi_{22}(\eta) + [\Pi_{33}(t)]\pi_{33}(\eta) = 0, \tag{2.31b}$$

which implies that the bracketed terms, if not negligible, are proportional for self-similarity.

In the experiments of Reynolds (1962), Keffer (1965) and Keffer (1967) and in all of the computations described here, the strain rate a_{ij} is constant in time. For such cases equation (2.26) yields

$$U_s(t)\delta(t) = U_s^0\delta^0\mathrm{e}^{(a_{22}-a_{11})t}. \tag{2.32}$$

Dividing equation (2.27) by the non-zero wake deficit $U_s(t)$ yields

$$\left[\frac{1}{\delta}\frac{\mathrm{d}\delta}{\mathrm{d}t}\right]\eta\frac{\mathrm{d}f}{\mathrm{d}\eta} - \left[\frac{1}{U_s}\frac{\mathrm{d}U_s}{\mathrm{d}t}\right]f(\eta) - [a_{11}]f(\eta) - [a_{22}]\eta\frac{\mathrm{d}f}{\mathrm{d}\eta} + \left[\frac{K_{12}}{U_s\delta}\right]\frac{\mathrm{d}k_{12}}{\mathrm{d}\eta} = -v\left[\frac{1}{\delta^2}\right]\frac{\mathrm{d}^2f}{\mathrm{d}\eta^2}. \tag{2.33}$$

† The analysis could be done using the tensorially correct expression $\overline{u'_i u'_j} = K_{ijmn}(t)k_{mn}(\eta)$, which replaces $\overline{u'_i u'_j}$ by the sum of nine terms. Equation (2.39) would then be generalized to $K_{ijmn}(t) \propto \exp(C_{ijmn}t)$ and the K_{12} term in equation (2.27) would be replaced by nine terms, all proportional to each other and thus replaceable by a single term as is done above. Similar reasoning applies to the analysis of the $K_{\alpha\beta}$ terms in the Reynolds stress transport equation (2.29).

For the case of constant strain rate examined here, the time-dependent portions of the third and fourth terms of equation (2.33) are constant. For self-similar solutions in which all the terms in this equation are important, all the bracketed time-dependent terms should be proportional and therefore also constant.† Thus the various scales must grow exponentially in time and can be defined as

$$\delta(t) \propto \exp(C_\delta t) \tag{2.34a}$$

$$U_s(t) \propto \exp(C_M t) \tag{2.34b}$$

$$K_{12}(t) \propto U_s(t)\delta(t) \propto \exp(C_{12} t). \tag{2.34c}$$

The bracketed portion of the viscous term is not, in general, constant. However, the moderately high Reynolds numbers of the simulations and the absence of any solid boundaries in these free shear flows result in viscous terms that are typically negligible. Because of this, self-similar evolution can be achieved for at least some time even if the time dependence of the viscous term is different from the rest of the terms in the mean momentum equation. Thus, this term imposes no constraint on the self-similar analysis. It should be noted, however, that when $C_\delta = 0$ (i.e. the strained wake is of constant width) the viscous terms will change in proportional to the other terms, even if they are small in magnitude. From equation (2.32) it is clear that

$$C_M + C_\delta = a_{22} - a_{11}. \tag{2.35}$$

Combined with the mean momentum equation result (2.34c) this yields

$$C_{12} = C_M + C_\delta = a_{22} - a_{11}. \tag{2.36}$$

Dividing the Reynolds stress transport equation (2.29) by the non-zero Reynolds stress magnitude $K_{\alpha\beta}(t)$ yields

$$-\left[\frac{1}{\delta}\frac{d\delta}{dt}\right]\eta\frac{dk_{\alpha\beta}}{d\eta} + \left[\frac{1}{K_{\alpha\beta}}\frac{dK_{\alpha\beta}}{dt}\right]k_{\alpha\beta} + [a_{22}]\eta\frac{dk_{\alpha\beta}}{d\eta}$$

$$= \tilde{\mathscr{P}}_{\alpha\beta} - \left[\frac{Tr_{\alpha\beta}}{K_{\alpha\beta}\delta}\right]\frac{dtr_{\alpha\beta}}{d\eta} + \left[\frac{\Pi_{\alpha\beta}}{K_{\alpha\beta}}\right]\pi_{\alpha\beta}(\eta) - \left[\frac{D_{\alpha\beta}}{K_{\alpha\beta}}\right]d_{\alpha\beta}(\eta) + v\left[\frac{1}{\delta^2}\right]\frac{d^2 k_{\alpha\beta}}{d\eta^2}, \tag{2.37}$$

where $\tilde{\mathscr{P}}_{\alpha\beta}$ is given by

$$\tilde{\mathscr{P}}_{11} = -2[a_{11}]k_{11}(\eta) + 2\left[\frac{K_{12}U_s}{K_{11}\delta}\right]k_{12}(\eta)\frac{df}{d\eta}, \tag{2.38a}$$

$$\tilde{\mathscr{P}}_{22} = -2[a_{22}]k_{22}(\eta), \tag{2.38b}$$

$$\tilde{\mathscr{P}}_{33} = -2[a_{33}]k_{33}(\eta), \tag{2.38c}$$

$$\tilde{\mathscr{P}}_{12} = -[(a_{11} + a_{22})]k_{12}(\eta) + \left[\frac{K_{22}U_s}{K_{12}\delta}\right]k_{22}(\eta)\frac{df}{d\eta}. \tag{2.38d}$$

The two bracketed terms in each equation that directly involve the strain rate a_{ij} are constant when the strain rate is constant, as is the bracketed portion of the first term, given the form of δ found above in equation (2.34a). Thus, if all the terms are proportional, the bracketed portions of the other terms should also be constant, implying

$$K_{ij}(t) \propto \exp(C_{ij} t). \tag{2.39}$$

† This differs from the self-similar evolution of an unstrained wake, in which the first two and last two bracketed terms in equation (2.33) are not constant, but proportional to $1/t$.

This is consistent with equation (2.34*c*), which resulted from analysis of the mean momentum equation. As with the mean momentum equation, the bracketed coefficient of the viscous term is generally not constant and can only evolve self-similarly for strained wakes of constant thickness. However, the simulations confirm that this viscous diffusion term is negligible in comparison to the other terms in the Reynolds stress balance, and this constraint on the similarity analysis can therefore be dropped.

Additional constraints on the self-similar solution result from the shear production terms in the $\overline{u_1'^2}$ and $\overline{u_1'u_2'}$ equations. For the bracketed portions of these terms to be constant,

$$C_{12} + C_M - C_{11} - C_\delta = 0 \tag{2.40}$$

and

$$C_{22} + C_M - C_{12} - C_\delta = 0. \tag{2.41}$$

Combined with the result from the mean momentum equation, $C_{12} = C_M + C_\delta$, the constraint from the $\overline{u_1'^2}$ equation becomes $2C_M = C_{11}$, indicating that for self-similarity $\overline{u_1'^2} \propto U_s^2$. Combining the same mean momentum equation result with the constraint from the $\overline{u_1'u_2'}$ equation yields $2C_\delta = C_{22}$. The time variation of the turbulent transport, pressure–strain, and dissipation terms can also be determined from equation (2.37) if these terms are evolving in proportion to the other terms in the equation.

Finally, the pressure–strain condition (2.31*b*) implies that

$$[\Pi_{11}(t)] \propto [\Pi_{22}(t)] \propto [\Pi_{33}(t)], \tag{2.42}$$

which, together with the scalings from the Reynolds stress transport equation, leads to

$$K_{11} \propto K_{22} \propto K_{33} \tag{2.43}$$

or

$$C_{11} = C_{22} = C_{33} \tag{2.44}$$

(unless some of the pressure–strain terms are negligible). With the previous results, this yields $C_\delta = C_M$. Thus, if only the viscous terms are negligible, the self-similar solution is

$$C_\delta = C_M = (a_{22} - a_{11})/2, \tag{2.45a}$$

$$C_{11} = C_{22} = C_{33} = C_{12} = a_{22} - a_{11}. \tag{2.45b}$$

Intuitively this makes sense, because for self-similar evolution one would expect the shear and strain to be in balance; thus the constant-strain-rate case considered here should also have constant shear rate for self-similarity, as implied by $C_M = C_\delta$. Note that the above solution also implies that all the Reynolds stresses grow at the same rate and that their anisotropy is constant. This solution is completely analogous to that found by Reynolds (1962) and Keffer (1965) for the spatially evolving case.

From equation (2.45*a*) it is clear that a constant-width strained wake ($C_\delta = 0$) is only consistent with the above self-similar solution when the strain is axisymmetric and of the form $a_{11} = a_{22}$ (implying $a_{33} = -2a_{11} = -2a_{22}$). For this case, the self-similar solution suggests the possibility of a statistically stationary turbulence. As noted above, in this case the viscous terms in the mean momentum and Reynolds stress equations can be retained in the self-similar analysis.

2.2.2. *Other equilibrium similarity states*

In this section more general 'equilibrium similarity solutions' for strained plane wakes are derived. These solutions result from the removal of some constraints imposed in the classical self-similar analysis of §2.2.1 and have greater generality than the classical solution, as they possess several free parameters. The solutions are derived by combining terms in the governing equations and/or eliminating terms that are zero from the analysis. Elements of the analysis presented below are thus similar to those in the work of George & Castillo (1997) and Castillo & George (2001) on turbulent boundary layers with and without streamwise pressure gradients.

There are some limitations on the range of applicability of the solution (2.45). These are best identified by regrouping terms in equations (2.33) and (2.37). Combining terms in the mean momentum equation yields

$$\left[\frac{1}{\delta}\frac{d\delta}{dt} - a_{22}\right]\eta\frac{df}{d\eta} - \left[\frac{1}{U_s}\frac{dU_s}{dt} + a_{11}\right]f(\eta) + \left[\frac{K_{12}}{U_s\delta}\right]\frac{dk_{12}}{d\eta} = -\nu\left[\frac{1}{\delta^2}\right]\frac{d^2f}{d\eta^2}. \quad (2.46)$$

Differentiating equation (2.32) with respect to time leads to

$$\frac{1}{\delta}\frac{d\delta}{dt} + \frac{1}{U_s}\frac{dU_s}{dt} = a_{22} - a_{11}, \quad (2.47)$$

which can be used to further reduce equation (2.46) to

$$\left[\frac{1}{\delta}\frac{d\delta}{dt} - a_{22}\right]\left(\eta\frac{df}{d\eta} + f(\eta)\right) + \left[\frac{K_{12}}{U_s\delta}\right]\frac{dk_{12}}{d\eta} = -\nu\left[\frac{1}{\delta^2}\right]\frac{d^2f}{d\eta^2}. \quad (2.48)$$

This result can be integrated in η and combined with the known boundary conditions to produce

$$\left[\frac{1}{\delta}\frac{d\delta}{dt} - a_{22}\right]\eta f(\eta) + \left[\frac{K_{12}}{U_s\delta}\right]k_{12} = -\nu\left[\frac{1}{\delta^2}\right]\frac{df}{d\eta}. \quad (2.49)$$

Terms in the Reynolds stress transport equation (2.37) can also be grouped together,

$$\left[a_{22} - \frac{1}{\delta}\frac{d\delta}{dt}\right]\eta\frac{dk_{\alpha\beta}}{d\eta} + \left[(a_{\alpha\alpha} + a_{\beta\beta}) + \frac{1}{K_{\alpha\beta}}\frac{dK_{\alpha\beta}}{dt}\right]k_{\alpha\beta}$$
$$= \tilde{\mathscr{P}}^w_{\alpha\beta} - \left[\frac{Tr_{\alpha\beta}}{K_{\alpha\beta}\delta}\right]\frac{dtr_{\alpha\beta}}{d\eta} + \left[\frac{\Pi_{\alpha\beta}}{K_{\alpha\beta}}\right]\pi_{\alpha\beta}(\eta) - \left[\frac{D_{\alpha\beta}}{K_{\alpha\beta}}\right]d_{\alpha\beta}(\eta) + \nu\left[\frac{1}{\delta^2}\right]\frac{d^2k_{\alpha\beta}}{d\eta^2}, \quad (2.50)$$

where $\tilde{\mathscr{P}}^w_{\alpha\beta}$ is the wake shear production given by

$$\tilde{\mathscr{P}}^w_{11} = 2\left[\frac{K_{12}U_s}{K_{11}\delta}\right]k_{12}(\eta)\frac{df}{d\eta}, \quad (2.51a)$$

$$\tilde{\mathscr{P}}^w_{22} = 0, \quad (2.51b)$$

$$\tilde{\mathscr{P}}^w_{33} = 0, \quad (2.51c)$$

$$\tilde{\mathscr{P}}^w_{12} = \left[\frac{K_{22}U_s}{K_{12}\delta}\right]k_{22}(\eta)\frac{df}{d\eta}. \quad (2.51d)$$

Substituting the self-similar solution (2.45) into equation (2.49) yields

$$-\left[\frac{a_{11} + a_{22}}{2}\right]\eta f(\eta) + \left[\frac{K^0_{12}}{U^0_s\delta^0}\right]k_{12} = -\nu\left[\frac{1}{(\delta^0)^2 e^{(a_{22} - a_{11})t}}\right]\frac{df}{d\eta}, \quad (2.52)$$

where $K^0_{ij} = K_{ij}(t = 0)$ is the value of K_{ij} at the virtual origin of the self-similar period

required to match the observed evolution. From this equation, it is apparent that the self-similar solution (2.45) cannot be valid for all strain geometries. Unless $a_{22} \geqslant a_{11}$ the viscous term will grow exponentially, ultimately making a balance with the other (constant) terms impossible.† Also, if $a_{11} + a_{22} = 0$, the first bracketed term is zero and the two remaining terms cannot balance ($a_{11} = a_{22}$ is not possible for non-zero applied strain when $a_{11} + a_{22} = 0$). Substituting the solution (2.45) into equation (2.50) and requiring that the viscous diffusion terms be balanced by the left-hand-side terms and $\tilde{\mathscr{P}}^w_{\alpha\beta}$ also requires that $a_{22} \geqslant a_{11}$. Thus alternative similarity solutions must be sought for cases in which $a_{22} < a_{11}$ or $a_{11} + a_{22} = 0$.

Other possible similarity solutions may exist in which some of the terms that constrained the above self-similar analysis are zero, or in which certain combinations of the terms combine to be zero. The analysis leading to the 'classical' solution (2.45) is invalid when the first term of equations (2.49) and (2.50) is zero, which occurs when $\delta(t) = \delta^0 \exp(a_{22}t)$ or $C_\delta = a_{22}$.‡ With this spreading rate, equation (2.32) leads to $U_s(t) = U_s^0 \exp(-a_{11}t)$. In this case the viscous term in the mean momentum equation (2.49) cannot be negligible, as it is the only term remaining to balance the Reynolds shear stress. Requiring that the two non-zero bracketed terms be proportional yields

$$K_{12}(t) = K_{12}^0 e^{-(a_{11}+a_{22})t} \quad \text{and} \quad k_{12}(\eta) = \frac{-\nu U_s^0}{\delta^0 K_{12}^0} \frac{\mathrm{d}f}{\mathrm{d}\eta}, \tag{2.53}$$

which is different from the results in equations (2.36) and (2.52). Ensuring that the left-hand side of the $\overline{u_1'^2}$ transport equation scales like $\tilde{\mathscr{P}}^w_{11}$ then determines the form of K_{11}. The pressure–strain condition (2.42) and the transport equations for $\overline{u_2'^2}$ and $\overline{u_3'^2}$ fix the forms of K_{22} and K_{33}. The solution is

$$\frac{\delta(t)}{\delta^0} = e^{a_{22}t}, \quad \frac{U_s(t)}{U_s^0} = e^{-a_{11}t}, \quad \frac{K_{12}(t)}{K_{12}^0} = e^{-(a_{11}+a_{22})t}, \tag{2.54a}$$

$$\frac{K_{11}(t)}{K_{11}^0} = e^{-2a_{11}t}(1 + D_1(1 - e^{-2a_{22}t})) \quad \text{if} \quad a_{22} \neq 0, \tag{2.54b}$$

$$= e^{-2a_{11}t}(1 + D_1 at) \quad \text{if} \quad a_{22} = 0, \tag{2.54c}$$

$$\frac{K_{22}(t)}{K_{22}^0} = e^{-2a_{22}t}(1 + D_2(1 - e^{-2a_{11}t})) \quad \text{if} \quad a_{11} \neq 0, \tag{2.54d}$$

$$= e^{-2a_{22}t}(1 + D_2 at) \quad \text{if} \quad a_{11} = 0, \tag{2.54e}$$

$$\frac{K_{33}(t)}{K_{33}^0} = e^{-2a_{33}t}(1 + D_3(1 - e^{4a_{33}t})) \quad \text{if} \quad a_{33} \neq 0, \tag{2.54f}$$

$$= 1 + D_3 at \quad \text{if} \quad a_{33} = 0, \tag{2.54g}$$

where D_1, D_2, and D_3 are parameters that arise from the removal of the constraints previously imposed to ensure that the first term in equations (2.49) and (2.50) scales like the others; this term is now zero and no longer imposes such constraints. The magnitude of the strain rate in the two strained directions, a, is used to make D_1, D_2 and D_3 dimensionless in the special plane strain cases where $a_{22} = 0$, $a_{11} = 0$, and $a_{33} = 0$ (equations 2.54*c, e, f*). Note that for this similarity solution the bracketed

† Note that Reynolds (1962) recognized this and speculated that for the strain geometry he considered the flow might eventually relaminarize.

‡ Examination of the simulations indicates that this does indeed occur for developed strained wakes when $a_{22} > 0$, e.g. cases B, C, FC, SC and H described later.

terms in equations (2.33) and (2.37) are not all proportional; instead combinations of the left-hand-side terms cancel each other out.

The equilibrium similarity solution (2.54) does not satisfy equation (2.43) and the individual normal Reynolds stress components grow or decay at different rates, unlike for the classical solution (2.45). This is possible because the non-zero bracketed coefficients in equation (2.50) are no longer constant and the pressure–strain term $\Pi_{\alpha\beta}$ is thus not required to be proportional to $K_{\alpha\beta}$. Also, because the first term in equation (2.50) is zero, the bracketed terms in the transport equation for any one component of the Reynolds stress tensor are not, in general, proportional to the bracketed terms in the equations for the other components. Therefore, the ratios $\Pi_{\alpha\beta}/K_{\alpha\beta}$ are not necessarily proportional to each other and the pressure–strain condition (2.42) no longer implies that equation (2.43) must be valid.

Given the above family of solutions, there are now many possible similarity solutions to choose from for the normal Reynolds stresses. For these solutions to be sustained, they must be maintained at large times. This places certain restrictions on the values of D_1, D_2 and D_3 that can be used while still maintaining positive normal Reynolds stresses. In particular, if $a_{22} > 0$ then $D_1 \geqslant -1$, if $a_{22} = 0$ then $D_1 \geqslant 0$, and if $a_{22} < 0$ then $D_1 \leqslant 0$. Similarly, if a_{11} is positive, zero, or negative, then D_2 is $\geqslant -1$, $\geqslant 0$, or $\leqslant 0$, respectively, and if a_{33} is positive, zero, or negative, then D_3 is $\leqslant 0$, $\geqslant 0$, or $\geqslant -1$, respectively.

The classical self-similar solution (2.45) predicts that all the Reynolds stress components change at the same rate and therefore that the Reynolds stress anisotropy and the shear stress correlation coefficient $\overline{u_1'u_2'}/(\sqrt{\overline{u_1'}^2}\sqrt{\overline{u_2'}^2})$ are constant in time. For the equilibrium similarity solution (2.54), the various Reynolds stress components will evolve differently from each other. This implies that the anisotropy is not constant and the shear stress correlation coefficient is only constant if $D_1 = D_2 = 0$. In fact, to satisfy the Schwarz inequality for arbitrary initial correlation coefficients, it is necessary to impose stricter limitations on the values of D_1, D_2, and D_3 than those outlined in the previous paragraph, namely the conditions $D_i \geqslant -1$ must be replaced by $D_i \geqslant 0$ to ensure that the correlation coefficient remains less than or equal to 1 when it is initially 1.

In high-Reynolds-number flows away from walls, such as the strained wakes considered here, the viscous diffusion terms are negligible. They are thus often neglected in the similarity analysis of such flows. If, on the other hand, one insists that these terms must remain small, or at least not grow more rapidly than the other terms in the balance, then certain restrictions are imposed on the strain geometries for which the similarity solution (2.54) can be sustained. For all strain geometries, the viscous diffusion of $\overline{u_1'u_2'}$ does not grow faster in time than the shear production of $\overline{u_1'u_2'}$ and thus no restrictions are imposed by this balance (note that for this similarity solution all of the terms on the left-hand side of equation (2.50) for $\overline{u_1'u_2'}$ are zero). On the other hand, balancing the viscous diffusion of $\overline{u_1'}^2$ requires that $a_{22} \geqslant 0$ and if $a_{22} = 0$ then D_1 must be zero, again resulting in all the terms of the left-hand side of equation (2.50) being zero. Balancing the viscous diffusion of $\overline{u_2'}^2$ requires that $a_{22} \geqslant a_{11}$ when $a_{11} \geqslant 0$ and $a_{22} \geqslant 0$ when $a_{11} \leqslant 0$. Balancing the viscous diffusion of $\overline{u_3'}^2$ is the most limiting requirement of all, only being possible when $a_{22} \leqslant -2a_{11}$ and $a_{22} \geqslant 0$. Only two of the eight strain geometries simulated fall within this range (those of cases C and E).

More terms can be eliminated from the similarity analysis if the second term

of the Reynolds stress transport equation (2.50) is also zero, which happens when $C_{11} = -2a_{11}$, $C_{22} = -2a_{22}$, $C_{33} = -2a_{33}$, and $C_{12} = -(a_{11} + a_{22})$, corresponding to $D_1 = D_2 = D_3 = 0$ in the solution (2.54). (Note that the C_{12} result agrees with that derived from the mean momentum equation previously). In this case, the entire left-hand side of equation (2.50) is zero and the left-hand-side terms should not have an impact on the self-similar analysis. Unlike with the mean momentum equation, it is not necessary to maintain the viscous terms in equation (2.50) to preserve a balance, which can be provided by the turbulent transport, pressure–strain, and dissipation terms. Thus it is possible for the viscous diffusion terms to be negligible for this similarity solution. On the other hand, it is also possible to retain these terms in the analysis because when $D_1 = D_2 = 0$ the viscous diffusion terms in the $\overline{u_1'^2}$ and $\overline{u_1'u_2'}$ equations scale like $\tilde{\mathscr{P}}_{11}^w$ and $\tilde{\mathscr{P}}_{12}^w$, respectively. If, as expected, the viscous diffusion terms are negligible, then each of the equations for the four non-zero Reynolds stress components in this case is simply a balance between production by the wake shear, turbulent transport, pressure–strain, and dissipation.

Even if the first term of equation (2.49) is not zero, a second equilibrium similarity solution is possible when the first two bracketed terms in this equation and (2.50) are proportional without both being constant, thus no longer requiring the exponential solutions of equations (2.34) and (2.39). In particular, the three-parameter family (E_1, E_2 and E_3) of solutions given by

$$\frac{\delta(t)}{\delta^0} = h(t)^{E_2} e^{a_{22}t}, \quad \frac{U_s(t)}{U_s^0} = \frac{e^{-a_{11}t}}{h(t)^{E_2}}, \quad \frac{K_{12}(t)}{K_{12}^0} = \frac{e^{-(a_{11}+a_{22})t}}{h(t)}, \tag{2.55a}$$

$$\frac{K_{11}(t)}{K_{11}^0} = \frac{e^{-2a_{11}t}}{h(t)^{2E_2}}, \quad \frac{K_{22}(t)}{K_{22}^0} = \frac{e^{-2a_{22}t}}{h(t)^{2(1-E_2)}}, \quad \frac{K_{33}(t)}{K_{33}^0} = \frac{e^{-2a_{33}t}}{h(t)^{E_3}}, \tag{2.55b}$$

$$h(t) = 1 + E_1(1 - e^{-2a_{22}t}) \quad \text{if} \quad a_{22} \neq 0 \tag{2.55c}$$

$$= 1 + E_1 at \quad \text{if} \quad a_{22} = 0 \tag{2.55d}$$

satisfies all constraints except the pressure–strain condition (2.43). As for the previous similarity solution (2.54), the bracketed terms in equations (2.33) and (2.37) are not all proportional; instead it is combinations of the left-hand-side terms (two groups of two each in the mean momentum and Reynolds stress equations) that are proportional to the other terms in the equations, as indicated in (2.49) and (2.50). With the solution (2.55), the bracketed terms on the left-hand sides of equations (2.49) and (2.50) and $\tilde{\mathscr{P}}_{\alpha\beta}^w$ are all proportional to $\exp(-2a_{22}t)/h(t)$. If $E_2 = \frac{1}{2}$ the viscous terms also have the same time dependence. After dividing by the common factor $\exp(-2a_{22}t)/h(t)$, equation (2.49) reduces to

$$[2E_1 E_2 a_{22}]\eta f(\eta) + \left[\frac{K_{12}^0}{U_s^0 \delta^0}\right] k_{12} = -v\left[\frac{h(t)^{1-2E_2}}{(\delta^0)^2}\right]\frac{df}{d\eta}, \tag{2.56}$$

where the first bracketed term is replaced by $E_1 E_2 a$ if $a_{22} = 0$. This relationship between $k_{12}(\eta)$ and the mean profile shape $f(\eta)$ can be contrasted with the corresponding expressions (2.52) and (2.53) derived from the classical similarity analysis and the similarity analysis leading to the equilibrium similarity solution (2.54), respectively.

As with the previous equilibrium similarity solution, the Reynolds stress components in equation (2.55) change at different rates. Even though the anisotropy is

thus not constant, the shear stress correlation coefficient $\overline{u_1' u_2'}/(\sqrt{\overline{u_1'^2}}\sqrt{\overline{u_2'^2}})$ is indeed constant, unlike with equation (2.54). Ensuring that the correlation coefficient remains less than or equal to 1 thus does not constrain the possible choices of E_1, E_2, and E_3.

Because the first bracketed term of equation (2.50) is the same for all α and β and is not equal to zero (as was the case for solution (2.54)), the terms $\Pi_{\alpha\beta}/K_{\alpha\beta}$ should be proportional to each other to ensure a balance with the other terms in the equation. This, combined with the pressure–strain condition (2.42), then implies that the normal Reynolds stresses K_{11}, K_{22}, and K_{33} should be proportional, as derived for the classical case (equation (2.43)). The only values of E_1, E_2, and E_3 that satisfy condition (2.43) are

$$E_1 = -1, \quad E_2 = \frac{(a_{11} + a_{22})}{4a_{22}}, \quad E_3 = \frac{-(3a_{11} + a_{22})}{2a_{22}} \quad \text{if} \quad a_{22} \neq 0, \qquad (2.57)$$

(no solution when $a_{22} = 0$ because then $h(t)$ is not of exponential form), which reduces the solution (2.55) to that given in equation (2.45). However, the pressure–strain condition (2.43) is also satisfied in the limit of large times for all E_1 when a_{22} is negative if E_2 and E_3 have the values given in equation (2.57). In this case the Reynolds stresses approach those of the classical solution (2.45) for large times.

Other self-similar solutions of the form (2.55) arising from different values of E_1, E_2 and E_3 may indeed be possible, however, as it is possible that the pressure–strain condition (2.43) may not always be satisfied. In particular, a secondary balance may be set up between the pressure strain, dissipation, and transport terms, whereby only their combination scales like the other terms in the Reynolds stress transport equation, allowing the pressure–strain terms $\Pi_{\alpha\beta}/K_{\alpha\beta}$ to scale differently from each other, while still permitting equation (2.42) to be satisfied. If this is indeed the case, then the additional generality of equation (2.55) may help to describe the observed evolution of the flow.

If this kind of secondary balance between the pressure–strain, the turbulent transport and the dissipation does indeed occur, then the previous equilibrium similarity solution (2.54) can be generalized even further. In particular, the similarity analysis for that case then imposes no constraints on the forms of the functions K_{22} and K_{33} because there is no wake shear production for these Reynolds stresses. Without the limitations on the forms of K_{22} and K_{33}, it is possible to balance the viscous diffusion terms whenever $a_{22} \geqslant 0$, implying that this would be possible for the strain geometries of cases B, F, and H, in addition to those of cases C and E.

For some values of E_1, the solution (2.55) reduces to those already derived above. If $E_1 = 0$ then $h(t) = 1$ and the solution reduces to the previous similarity solution (2.54) with $D_1 = D_2 = D_3 = 0$. If $E_1 = -1$ and $a_{22} \neq 0$ (when $a_{22} = 0$, the coefficient E_1 must be non-negative to prevent $h(t)$ from becoming negative and K_{12} from changing sign at large times) then $h(t) = \exp(-2a_{22}t)$, yielding

$$C_\delta = a_{22}(1 - 2E_2), \quad C_M = 2a_{22}E_2 - a_{11}, \quad C_{12} = a_{22} - a_{11}, \qquad (2.58a)$$

$$C_{11} = -2a_{11} + 4a_{22}E_2, \quad C_{22} = 2a_{22} - 4a_{22}E_2, \quad C_{33} = -2a_{33} + 2a_{22}E_3. \qquad (2.58b)$$

This is a purely exponential solution of the form given in equations (2.34) and (2.39) and thus reduces to the classical solution (2.45) when E_2 and E_3 are given by the values in equation (2.57).

For other values of E_1, E_2 and E_3, the long-time behaviour (the period of interest for sustained self-similar evolution) of the solution (2.55) is different depending on whether a_{22} is positive, zero or negative. For positive a_{22}, $h(t)$ approaches a constant

value of $1 + E_1$ and E_1 must be greater than or equal to -1 to ensure that $h(t)$ does not change sign. When $a_{22} > 0$, the solution (2.55) approaches that given by the previous similarity solution (2.54) for large times† (unless $E_1 = -1$). Also, the viscous terms scale like the other terms in the governing equations for any value of E_2 (except when $E_1 = -1$, in which case they only scale if $E_2 = \frac{1}{2}$).

When a_{22} equals zero, $h(t)$ approaches $E_1 at$ ($E_1 \geqslant 0$ for positive $h(t)$) and the width, deficit and Reynolds stresses approach the non-exponential behaviour given by equation (2.55) with $h(t)$ replaced by at, a_{22} replaced by zero, and the equalities replaced by proportionalities. Balancing the viscous terms requires that $E_2 \geqslant \frac{1}{2}$ or $E_1 = 0$.

When a_{22} is negative, $h(t)$ approaches $-E_1 \exp(-2a_{22}t)$ ($E_1 < 0$ for positive $h(t)$) and for large times the solution (2.54) approaches pure exponentials with exponents given by equation (2.58), as when $E_1 = -1$. It seems unlikely that a wake being compressed in the cross-stream direction could increase in width, implying that $E_2 \leqslant \frac{1}{2}$ when $a_{22} < 0$. However, examination of equations (2.49) and (2.50) indicates that $E_2 \geqslant \frac{1}{2}$ for the viscous terms to be balanced by other terms in these equations when $a_{22} \leqslant 0$. Thus when $a_{22} < 0$ it is likely that for physical solutions $E_2 = \frac{1}{2}$; indeed the numerical results indicate that this is correct. For this value of E_2, the viscous terms scale like the other terms in the governing equations (they approach a constant). Note that the long-time solution mentioned above with E_2 and E_3 given by the values in equation (2.57) only satisfies $E_2 = \frac{1}{2}$ when $a_{11} = a_{22}$ and thus may be unphysical for other strain geometries. When $E_2 = \frac{1}{2}$, the Reynolds stresses K_{12}, K_{11} and K_{22} are given by $K_{\alpha\beta}^0 \exp((-a_{\alpha\alpha} - a_{\beta\beta})t)/h(t)$. The choice $E_3 = 1$ results in the same expression for K_{33}.

Note that when $E_2 = 0$, the similarity solution (2.55) may also have some internal consistency limitations, because in this case the first term of equation (2.56) is zero. If $E_2 = 0$, the viscous term must be constant, which is not possible for $a_{22} < 0$, only possible when $a_{22} = 0$ if $E_1 = 0$, and only true for large times if $a_{22} > 0$. Even though the first term of equation (2.56) is also zero when $E_1 = 0$, a balance between the remaining two terms in this case is always possible because then $h(t) = 1$.

Table 1 summarizes the predicted self-similar behaviour of the wake half-width for all the strain geometries simulated. Also shown are schematics of the strain geometry for each case, with arrows indicating the directions of compression and expansion. Columns are included for the classical self-similar solution (2.45), the similarity solution (2.54), the similarity solution (2.55), including an additional column with the solution (2.55) evaluated for $E_2 = \frac{1}{2}$, and, for later comparison, the observed behaviour in the numerical simulations. The first two similarity solutions are not applicable to all the strain geometries; in such instances the entries are marked with an asterisk. The equilibrium similarity solution given by equation (2.55) is sustainable for all strain geometries and for $E_2 = \frac{1}{2}$ the viscous terms scale with the rest of the terms in the equations for all values of viscosity.

It should be emphasized that the existence of the above similarity solutions does not imply that actual strained wakes will exhibit such self-similar behaviour. Simple free shear flows, such as wakes and mixing layers, do indeed evolve self-similarly

---

† Strictly speaking, for the similarity predictions of the normal Reynolds stresses $\overline{u_2'^2}$ and $\overline{u_3'^2}$ to be the same for large times it is required that either $a_{11} > 0$ or $D_2 = D_3 = 0$. However, as noted above, if the pressure–strain terms only scale when combined with the turbulent transport and dissipation terms, then no restrictions need to be imposed on the behaviour of $\overline{u_2'^2}$ and $\overline{u_3'^2}$ to maintain self-similarity and the solution (2.54) can be further generalized, permitting agreement with solution (2.55) even when $a_{11} \leqslant 0$ and D_2 and D_3 are not zero.

Case	a_{11}/a	a_{22}/a	a_{33}/a	(2.45)	(2.54)	(2.55)	(2.55), $E_2 = 1/2$	DNS
A	0	−1	+1	$−1/2^*$	$−1^*$	$2E_2 − 1$	0	0
B	0	+1	−1	+1/2	+1	+1	+1	+1
C/SC/FC	−1	+1	0	$+1^*$	+1	+1	+1	+1
D	+1	−1	0	$−1^*$	$−1^*$	$2E_2 − 1$	0	0
E	−1	0	+1	+1/2	0	$(at)^{E_2}$	$(at)^{1/2}$	$(at)^{1/2}$
F	+1	0	−1	$−1/2^*$	0	$(at)^{E_2}$	$(at)^{1/2}$	$(at)^{1/2}$
G	−1/2	−1/2	+1	0	$−1/2^*$	$E_2 − 1/2$	0	0
H	+1/2	+1/2	−1	0	+1/2	+1/2	+1/2	+1/2

TABLE 1. Exponents n for exponential growth e^{nat} of δ/δ^0 predicted by similarity analysis and observed in the simulations. The predictions of equation (2.55) are for the asymptotic exponential behaviour at large times, and have have been evaluated in a second column for $E_2 = \frac{1}{2}$, the value suggested by physical arguments when $a_{22} < 0$. In cases E and F, the long-time predictions of equation (2.55) and the observed behaviour in the simulations are not exponential, but grow like $(at)^{1/2}$. Asterisks indicate predictions in which the similarity analysis is either internally inconsistent (cases C/SC/FC) or in which the viscous terms cannot be balanced at large times for any choice of the available parameters. Arrows indicate directions of compression and expansion for each case.

once developed, but the flows considered here are notably more complex, with two competing mechanisms of turbulent kinetic energy production. Additionally, even in simple free shear flows, self-similarity may require significant flow development to be achieved. As will be seen, certain orientations of mean strain can rapidly reduce the wake velocity deficit. In such flows the remnants of the original wake are negligible and a pure straining flow results prior to any self-similar equilibrium. Alternatively, other orientations of mean strain may result in an increasing wake deficit, which ultimately dominates the strain. The likelihood of achieving the self-similar strained wake state predicted by the classical solution (2.45), in which the wake shear and mean strain remain in balance, may thus be small.

Self-similar solutions are also possible for certain time-varying strain rates, as derived in Appendix A. The classical similarity solutions (2.45) and (A 5), derived here and in Appendix A, can also be obtained by a general Lie group analysis (Oberlack 2000) and their spatially developing analogues have been derived differently by Reynolds (1962) (note that his m is equal to our $−2m/(m−1)$), Gartshore (1967) and Narasimha & Prabhu (1972). However, these analyses do not predict the alternative equilibrium similarity solutions that are more relevant to the observed evolution of strained wakes.

3. Generating the simulations

3.1. *The numerical method*

The Galerkin spectral numerical method described in Spalart, Moser & Rogers (1991) was used by Moser *et al.* (1998) to generate simulations of unstrained temporally evolving plane wakes. Because these flows are temporally evolving, both the streamwise and spanwise directions are homogeneous and the spatial variations of the simulated variables in these directions can be represented by Fourier expansions.

The basis functions in the infinite inhomogeneous cross-stream direction are mapped Jacobi polynomials and a few 'extra' functions (two per k_x, k_z wavenumber pair) that exactly represent the far-field behaviour of quantities exhibiting slowly decaying potential tails (such as the velocity). These extra functions are precomputed once for each computational mesh used.

With the addition of uniform global strain, the simulation of the turbulence (equations (2.13) and (2.14) or analogous vorticity fluctuation equations) is complicated by the fluctuating velocity derivative term with a coefficient that has explicit dependence on the spatial coordinates x_i. In the laboratory reference frame, the problem is no longer periodic and homogeneous. However, if the problem is transformed to a computational coordinate system that moves with the mean strain, the streamwise and spanwise directions again become periodic and homogeneous. This transformation was developed by Rogallo (1977, 1981) for simulating strained homogeneous turbulence, but has also been used by Coleman, Kim & Spalart (2000) to simulate strained channel flow for a study of three-dimensional boundary layers. In order to simulate strained free shear flows it would thus be desirable to combine this transformation with the numerical method of Spalart *et al.* (1991). Unfortunately, this would require recomputing the 'extra' basis functions at every time step, which would be prohibitively time consuming for the computation. Thus, for the purposes of simulating strained wakes, the method of Corral & Jimenez (1995) was used to represent spatial variation in the cross-stream inhomogeneous direction, rather than the method of Spalart *et al.* (1991). Instead of mapping an infinite cross-stream domain onto a finite interval, Corral & Jimenez (1995) simulate the vorticity field in a truncated domain, with the domain boundaries being outside the vortical region of the flow. Periodicity is assumed in the cross-stream direction for the purposes of time advancing the vorticity field, but the effect of the undesired periodic image flows is removed by using an appropriately corrected velocity field when computing the nonlinear terms.

The numerical method used to generate all the simulations described in this paper combines the transformation developed by Rogallo (1977, 1981) with the method of Corral & Jimenez (1995) to simulate strained inhomogeneous free shear flows. The mathematical details of this method are outlined in Appendix B. It is a non-trivial task to recover the 'standard' Reynolds stress balance terms in equation (2.15) from the vorticity formulation used in the computations. Because of this, many useful formulas in the 'moving' coordinate system that aid in computing these quantities are included in Appendix B. By substituting $B_{ij} = \delta_{ij}$ and $a_{ij} = 0$, the corresponding 'unstrained' equations can be recovered.

In the computational 'moving' coordinates, the self-similar analysis presented in §2.2 is modified. In general, each term acquires the appropriate B_{ij} associated with differentiation and there is a one-to-one correspondence between terms in the transformed equations and the equations presented in §2.2. However, the terms with the $a_{22}x_2$ coefficients in equations (2.9a) and (2.16) and the corresponding terms with $a_{22}\eta$ coefficients in (2.27) and (2.29) are absorbed into the time-derivative terms in the transformed set of equations. Since the balance terms are computed in the computational variables they are presented with these two terms combined (see Appendix D). Of course the actual similarity solutions derived in §2.2 remain unchanged.

3.2. *The initial conditions*

Free shear flows are known to be sensitive to their initial conditions, and the task of choosing appropriate initial conditions for the simulations thus requires care. In many practical situations, such as the flow over a multicomponent airfoil, the 'strain'

or pressure gradient associated with downstream components may influence the flow well before the wake of an upstream component is fully developed. Also, it is unlikely that the effective strain (or pressure gradient) will vary with downstream distance as is necessary for the self-similar solutions presented in §2.2 or Appendix A to apply. The simulations presented here are not designed to replicate any particular reported experimental situation, but more generally to clarify the effects of such global straining and to provide a database that will aid in turbulence model development for turbulent flows in which turbulence is produced both by strain and shear. In keeping with this simplified picture, here a uniform and constant strain rate is applied suddenly at a point where the wake is evolving self-similarly and the effects associated with the near-wall region of the wake-generating body are no longer significant (e.g. the mean velocity profile is no longer cusp-like, viscous diffusion terms are negligible, etc.). This is similar to the situation that Reynolds (1962) and Keffer (1965, 1967) tried to create in their experiments.

The initial conditions used here are instantaneous fields from the developed unstrained wake simulations of Moser *et al.* (1998). In order to have the largest sample of large-scale eddies present in the computational domain when the strain is applied, the first field that is deemed to be in the 'self-similar' period is used (at later times the wake has spread and there are fewer large-scale eddies in the computational domain, resulting in a poorer statistical sample). In Moser *et al.* (1998) three wakes were simulated, including an 'unforced' wake and two 'forced' wakes. These simulations were begun from two realizations of a turbulent boundary layer simulation generated by Spalart (1988), but in the 'forced' cases additional energy was added (at time $t = 0$ only) to the two-dimensional modes of the computation. In the 'strongly forced' case, so much energy was added that the wake spreading rate is very high compared with experimental values and the wake only becomes approximately self-similar for a brief period before the evolution is limited by the computational domain size. This would thus be a poor case to use as an initial condition for the strained cases considered here. The 'weakly forced' and 'unforced' cases, which have longer periods of self-similar evolution and spreading rates that are in line with what is observed experimentally, are probably both acceptable as initial conditions. The addition of energy to the two-dimensional modes of the 'weakly forced' case results in initial wake turbulence that is not a solution of the Navier–Stokes equations. Much of this energy must be dissipated and diffused before an equilibrium between these terms and the turbulence production can be achieved. Presumably this has largely occurred by the time the wake becomes self-similar, but it is possible that transients associated with changes in initial conditions could be very long-lived. The faster spreading rate of the 'weakly forced' wake also results in a thicker wake during its self-similar period, and therefore a poorer statistical sample of large eddies in the given domain size. For these reasons, the 'unforced' case is used here to provide the initial conditions for the strained flows. As noted above, the initial field selected is at the start of the self-similar period, at $t_1 U_d^2/|A_w| = 42.8$ in this case (where U_d is the initial wake mean velocity deficit at $t = 0$, well prior to the straining, and A_w is constant for the unstrained wake). For this initial field, the wake mean velocity deficit is $U_m = 0.265 U_d$ and the wake half-width is $b = 3.59|A_w|/U_d$. Note that, as described in Moser *et al.* (1998), this unforced case has less organized large-scale structure than the forced wakes.

3.3. *Summary of flows simulated*

All of the simulated wake flows described in this paper evolve in the presence of a constant and uniform mean strain rate. Self-similar evolution of such flows is

Case	a_{11}/a	a_{22}/a	a_{33}/a	N_x^f	N_y^f	N_z^f	ab^0/U_m^0	$a\Delta t$	$e^{a\Delta t}$	CPU
A	0	−1	+1	320	200	448	0.271	2.10	8.2	222
B	0	+1	−1	280	560	16	0.271	2.30	10.0	62
C	−1	+1	0	32	700	64	0.271	1.90	6.7	107
SC	−1	+1	0	20	680	48	0.068	1.90	6.7	118
FC	−1	+1	0	96	768	112	1.084	1.82	6.1	60
D	+1	−1	0	1536	128	64	0.271	2.30	10.0	72
E	−1	0	+1	64	340	384	0.271	1.55	4.7	176
F	+1	0	−1	1536	300	12	0.271	2.30	10.0	74
G	−1/2	−1/2	+1	160	324	384	0.271	2.00	7.4	240
H	+1/2	+1/2	−1	768	300	16	0.271	2.30	10.0	53

TABLE 2. Strain geometry, number of modes at final remesh (initial values are $N_x^i = 512$, $N_y^i = 240$, and $N_z^i = 128$), strain rate, total strain ($\Delta t = t_f - t_1$, final time minus time at initiation of strain), and Cray C90 CPU hour requirement for each simulation.

mathematically possible, as has been described in §2.2. For the self-similar analysis, it was not necessary to precisely define the scales U_s and δ. At this point we will choose the peak magnitude of the velocity deficit U_m and the wake half-width b for these two scales, consistent with previous investigators. The half-width is here defined as the distance between the y-locations at which the mean velocity deficit is half of U_m (note that some investigators take the half-width to be half this distance). Because of the incompressibility condition (2.6), only two of the three constant strain rates a_{11}, a_{22}, and a_{33} can be chosen arbitrarily. Here both plane (one of the three a_{ij} being zero) and axisymmetric (two of the three a_{ij} being equal) irrotational mean strains are considered.

In the case of plane strain, one direction is stretched, another is compressed, and the third is unstrained. There are six possible plane strain geometries in which the strain is aligned with the coordinate directions. All six cases have been simulated at a strain rate of $ab^0/U_m^0 = 0.271$, where a corresponds to the magnitude of the strain rate in each of the two strained coordinate directions, and b^0 and U_m^0 are the wake width and velocity deficit, respectively, at the time t_1 at which the strain is initially applied. These six cases are listed in table 2, along with some details of the computation for each case.

The value of the strain rate for the plane strain simulations was chosen to be of the same order as the initial ($t = t_1$) inverse turbulence time scale ϵ/q^2, with the initial value of the dimensionless ratio aq^2/ϵ being 1.06 at the centreline. In the experiments of Reynolds (1962) and Keffer (1967) (on the spatially evolving flows analogous to cases A and B of table 2, respectively) no measurements of the Reynolds stresses or dissipation rate are given to compute the time scale q^2/ϵ. The experiments of Keffer (1965) include some Reynolds stress measurements and a 'strained isotropic turbulence' estimate of ϵ at one location in one of his strained wakes, but no estimates of ϵ at the duct inlet are given. It is thus difficult to compare the computational initial value of aq^2/ϵ to those of the experiments.

The above experiments do, however, provide information on both b and U_m at the distorting duct inlet. Thus the strain rate used in the experiments can be compared to the wake shear, and these values can be compared with the same dimensionless ratio in the computations. Reynolds (1962) reported values of b and U_m for a 1/2 in. cylinder placed with its axis 20.75 inches upstream of the distorting duct that yield $ab^0/U_m^0 =$

0.46. This value is 70% larger than that in the simulations. Using an empirical correlation relating wake velocity deficit to downstream distance for unstrained wakes, he expected only slightly smaller values for the smaller diameter cylinders. For a 3/16 in. cylinder placed 10 in. upstream of the same distorting duct, Keffer (1965) measured $ab^0/U_m^0 = 0.17$, a value 36% less than that used in the simulations, suggesting perhaps a greater sensitivity to cylinder diameter than anticipated by Reynolds (1962). With the distorting duct rotated to change the strain geometry to that of case B, Keffer (1967) reported values that give $ab^0/U_m^0 = 0.41$ for a 1/2 in. cylinder placed 20 in. upstream of the distorting duct inlet. The simulation value of $ab^0/U_m^0 = 0.271$ thus falls within the range of experimental values.

The spatially evolving flows analogous to cases C and D of table 2 are wakes evolving in the presence of streamwise pressure gradients. Because of the interest in studying wakes in adverse pressure gradients for multi-element airfoil design, additional strain rates have been simulated for the strain geometry of case C. These flows are also listed in table 2 (case FC with a strain rate four times larger than case C and case SC with a strain rate four times smaller than case C).

Experimental data for the strain geometries of cases E and F apparently do not exist for wake flows. Tucker & Reynolds (1968) did use a 'longitudinally distorting tunnel' with the strain geometry of case F in their study of strained homogeneous turbulence, but for initially isotropic turbulence the orientation of the straining is irrelevant and these results were used simply to confirm features seen in their 'laterally distorting tunnel' (in which the strain was oriented as in case A). Perhaps more relevant, Sreenivasan (1985) applied 'longitudinal' strain (as case F) to developed homogeneous turbulent shear flow in which the shear was oriented as for the wakes considered here.

There are also six possible orientations of coordinate-aligned axisymmetric strain. For these axisymmetric cases, one direction is stretched or compressed at a given strain rate and the other two directions are compressed or stretched, respectively, at half that rate. Only the two cases with $a_{11} = a_{22}$ (and magnitude $a/2$) have been simulated here. The classical self-similar analysis presented in §2.2.1 indicates the possibility of a self-similar statistically stationary flow for these cases. The strain rate for these cases has been chosen such that $a_{33}b^0/U_m^0 = \pm 0.271$, the same as the magnitude of a in the plane strain cases.

For all the simulations in this paper, the initial number of modes in each coordinate direction is $N_x^i = 512$, $N_y^i = 240$, and $N_z^i = 128$. This is because the required grid size is determined by the initial conditions, which are the same for all the cases. As each flow evolves, it becomes necessary to 'remesh' the simulation to maintain adequate resolution in some coordinate directions. In particular, directions that are stretched eventually require additional modes to adequately resolve the flow variation in those directions. Conversely, compressed directions may become adequately resolved with fewer modes, although this is not always the case when compression is in the cross-stream y-direction. In such cases the flow eventually resists the mean compression and the wake width becomes roughly constant (cases A, D, and G). Additionally, stretching in the spanwise z-direction intensifies the spanwise vorticity and this may require additional y-modes to resolve. Each simulation is remeshed several times to minimize the CPU time required for an accurate simulation (the number of different 'grids' used for each calculation varied from 7 in case F to 14 in case A). The number of modes used to resolve each coordinate direction after the final remesh is given in table 2. To fully dealias the results, the 'physical space' grids used to compute nonlinear products contain 3/2 as many grid points as the number of Fourier modes

listed for each of the coordinate directions. As seen in table 2, the number of Cray C90 CPU hours required for the different strain geometries is variable.

Most of the simulations had to be terminated when the domain size became too small to support an adequate (for statistical purposes) sample of eddies. This sample of eddies is not large to begin with, and compressing the domain soon reduces it to the point where the simulation is no longer a good model of the infinite-domain problem. As noted in table 2, some simulations were run until a total strain of $\exp(a\Delta t) = 10.0$, where Δt denotes the amount of time the strain is applied. For cases A and D, in which the cross-stream y-direction is the only direction being compressed, this is justified because the extent of the (x, z) computational domain increases in time as a result of the mean strain. Cases B, F and H were run to this point simply because the CPU requirements for the late-time results were small, owing to the limited spanwise domain size. The relevance of the late-time results in these cases is questionable, however. The computational effort required to run case E to similar total strains would have been significant and this run was terminated at a lower total strain of 4.7. Case C is particularly constrained by the domain size because the wake width is increasing rapidly in a shrinking streamwise domain; the wake width is several times the streamwise extent of the computational domain by the end of the simulation, limiting the aspect ratio of any large eddies that might be trying to develop. In case G, the streamwise domain extent is reduced at only half the rate of case C ($a_{11}b^0/U_m^0 = -0.136$) and the width of the wake is roughly constant, allowing more meaningful results at later times.

4. Results from the simulations

Turbulence statistics and flow visualizations from the simulated flow fields are examined in this section. Of particular interest is whether the flow evolutions are consistent with any of the similarity solutions presented in §2.2. If this is not the case, then the terms in the Reynolds stress balance can be examined to address in what ways the evolutions are departing from the predicted similarity.

4.1. *Plane strain cases*

4.1.1. *The wake mean velocity*

Although the area under the wake mean velocity profile A_w must grow exponentially (equation (2.12)), the Reynolds number $Re_m = bU_m/\nu$ grows exponentially only if the mean wake profiles are self-similar (equation (2.32)). The time evolution of Re_m for the six plane strain cases with $ab^0/U_m^0 = 0.271$ is shown in figure 1, plotted in log-linear coordinates to facilitate determination of exponential behaviour. The time coordinate has been non-dimensionalized as $\tau = tU_m^0/b^0$. Also plotted is the evolution of the Reynolds number of the unstrained wake, denoted by '$a = 0$'. The strain is applied at $\tau_1 = 3.16$ and at this time the evolutions for the various cases diverge. The Reynolds number evolutions are close to exponential from the instant the strain is applied onward, indicating that the mean velocity profiles for all these cases must indeed be similar when scaled by b and U_m. This is confirmed later by direct examination of the profiles. Defining the dimensionless exponential growth rates

$$n_{Re} = \frac{1}{Re_m}\frac{\mathrm{d}Re_m}{\mathrm{d}(at)}, \quad n_b = \frac{1}{b}\frac{\mathrm{d}b}{\mathrm{d}(at)}, \quad n_U = \frac{1}{U_m}\frac{\mathrm{d}U_m}{\mathrm{d}(at)}, \tag{4.1}$$

it can easily be verified that the value of n_{Re} for each simulation is the same as that predicted by the self-similar analysis, namely $(a_{22} - a_{11})/a$ (see table 3).
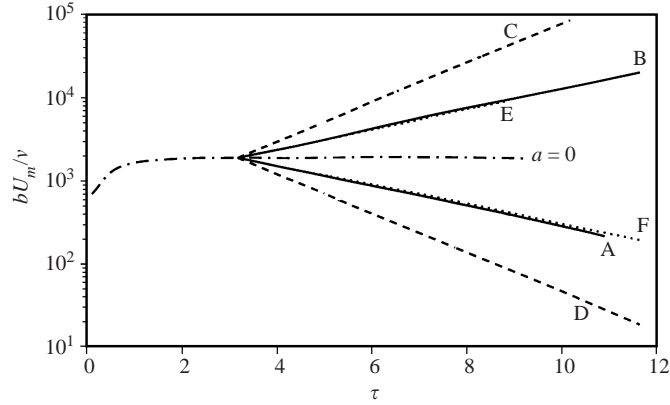
FIGURE 1. Evolution of the Reynolds number $Re_m = bU_m/v$ for the plane strain cases: ——, cases A (lower) and B (upper); – – – –, cases C (upper) and D (lower); ······, cases E (upper) and F (lower); and —·—, unstrained wake.

Case	a_{11}/a	a_{22}/a	a_{33}/a	$(a_{22} - a_{11})/a$	n_{Re}	n_b	n_U	$n_U - n_b$
A	0	−1	+1	−1	−1	0	−1	−1
B	0	+1	−1	1	1	1	0	−1
C/SC/FC	−1	+1	0	2	2	1	1	0
D	+1	−1	0	−2	−2	0	−2	−2
E	−1	0	+1	1	1	$1/4^*$	$3/4^*$	$1/2^*$
F	+1	0	−1	−1	−1	$1/3^*$	$-4/3^*$	$-5/3^*$
G	−1/2	−1/2	+1	0	0	0	0	0
H	+1/2	+1/2	−1	0	0	1/2	−1/2	−1

TABLE 3. Exponents n for exponential growth e^{nat} of Re_m, b, U_m, and the wake shear U_m/b observed in the simulations. Asterisks indicate values used to approximate apparent $(at)^{1/2}$ behaviour by exponentials.

According to the classical self-similar solution (2.45), the growth rate n_{Re} is shared equally between the wake width and the wake velocity deficit such that $n_b = n_U = n_{Re}/2$. In order to assess whether this is the case in the simulations, the evolutions of b and U_m must be examined individually.

The time evolution of the wake width b for the same six plane strain cases considered above is shown in figure 2, again plotted in log-linear coordinates and again with the unstrained wake results included for comparison. Cases B and C, for which the cross-stream direction is being expanded ($a_{22} > 0$), exhibit wake widths that become proportional to $\exp(a_{22}t)$, corresponding to $n_b = 1$. In cases A and D, for which the cross-stream direction is compressed ($a_{22} < 0$), the wake widths become roughly constant ($n_b \approx 0$). For the two cases E and F, in which the y-direction is unstrained, the wake spreading rate is similar to the $\tau^{1/2}$ evolution of the unstrained case (but can also be reasonably described by exponentials with $n_b \approx 0.3$). The observed values of n_b are listed in table 3 and also in the 'DNS' column of table 1 to facilitate comparison with the similarity analysis predictions.

The rapid spreading of the wakes in cases B and C limits the total strain that can be achieved in the numerical simulations. For these cases, either the streamwise (case C) or spanwise (case B) directions are being compressed while the wake width is
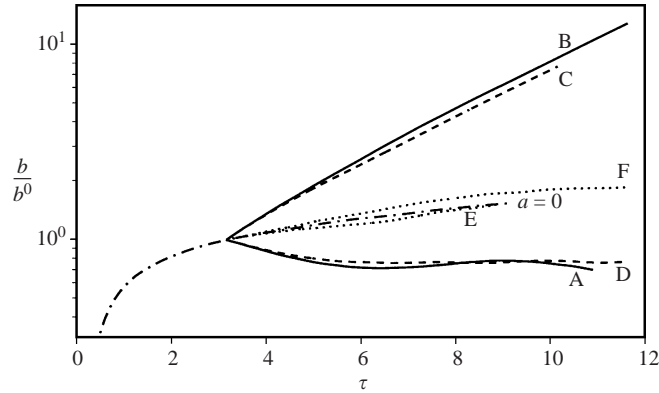
FIGURE 2. Evolution of the wake width b for the plane strain cases. Line styles as figure 1 but with E and F reversed.
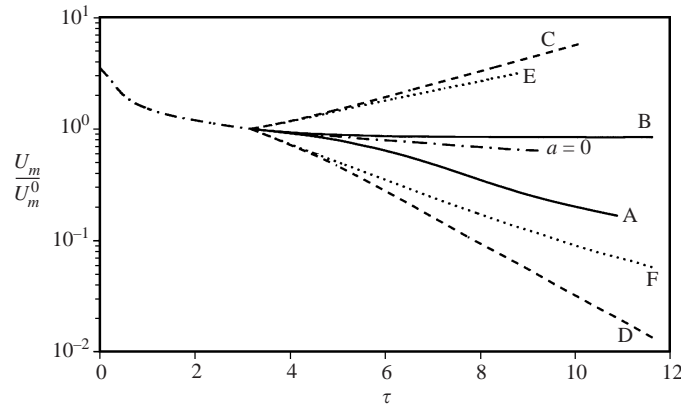

FIGURE 3. Evolution of the peak velocity deficit U_m for the plane strain cases.
Line styles as figure 1.

growing exponentially. Thus the aspect ratio of the computational domain is far from unity by the end of the simulation and roughly 'spherical' large turbulent eddies are prevented from forming, as noted in §3.3. Interestingly, in these cases such eddies are apparently not forming, even prior to the time when the domain size becomes limited. The turbulence in these two cases is characterized by many small-scale turbulent motions (see §4.4) and the limited domain size may not be affecting the simulations as strongly as might be anticipated. Nevertheless, for large enough times these two numerical simulations are undoubtedly affected by the computational domain size. The shrinking (x, z)-domain also results in a reduced sample of eddies for computing turbulence statistics. Combined with the numerous small-scale motions spread out over a large cross-stream extent, this leads to noisy statistical profiles at large times for these cases (see figures later in this section).

The peak velocity deficit U_m shown in figure 3 also evolves at least approximately exponentially after a developmental period, as expected since both b and the product bU_m ultimately grow exponentially. It is also clear that cases D and F, and to some extent also case A, exhibit rapidly decaying velocity deficits, indicating that the wake component of these flows is disappearing.

The exponential evolution of b and U_m once the flows are developed suggests
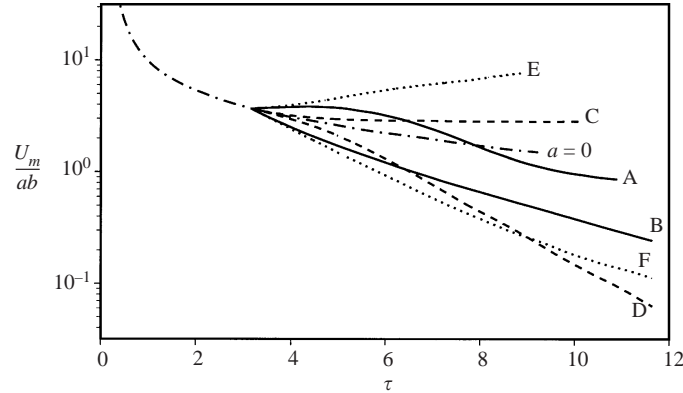
FIGURE 4. Ratio of wake shear rate to applied strain rate $U_m/(ab)$ for the plane strain cases: ——, cases A (upper) and B (lower); – – – –, cases C (upper) and D (lower); · · · · · ·, cases E (upper) and F (lower); and — · —, unstrained wake (with same value of a).

that the mean flow does ultimately evolve self-similarly. The observed values of n_b and n_U from the simulations are given in table 3. Although it is true that $n_b + n_U = n_{Re} = (a_{22} - a_{11})/a$, as seen in figure 1, n_b and n_U are not equal, except for case C (and case G, which is discussed later in §4.2). Note that when $n_b \neq n_U$, the shear rate associated with the wake profile does not remain in balance with the constant applied strain rate and therefore such flows will ultimately no longer be 'strained wakes', with either the strain or the wake component of the flow becoming irrelevant. Although the classical analysis does predict the observed value of n_b for case C, the analysis used to derive equation (2.45) is internally inconsistent for this case because the time-derivative and advection terms in the mean momentum equation (2.52) are zero when $a_{11} + a_{22} = 0$. Thus the classical self-similar solution (2.45) does not describe the mean flow evolution of any of the plane strain cases.

Examination of table 1 indicates that the observed mean flow behaviour in the simulations is in agreement with the equilibrium similarity solution (2.55), assuming that $E_2 = \frac{1}{2}$ when $a_{22} \leqslant 0$. For cases with $a_{22} < 0$, this value of E_2 was anticipated on physical grounds (§2.2.2). For the cases in which $a_{22} > 0$, both solutions (2.54) and (2.55) correctly describe the observed mean flow behaviour. In these cases, the examination of the Reynolds stress evolution in §4.1.3 may provide further evidence as to which solution better describes the computational results.

From equation (2.24) the wake shear rate can be written as

$$\frac{\partial \overline{U}_w}{\partial y} = \frac{-U_m(t)}{b(t)} \frac{\mathrm{d}f}{\mathrm{d}\eta}. \tag{4.2}$$

The ratio of the wake shear rate to the applied strain rate is thus characterized by $U_m/(ab)$, which is plotted in figure 4. Note that this ratio is of order 1 when the strain is first applied because the strain rate was chosen such that the shear and strain were of comparable importance. For cases B, D and F the relative strength of the wake shear has dropped by over an order of magnitude by the end of each simulation. Only for case C does this ratio reach a constant (a value of 2.82). Note that since both b and U_m eventually evolve exponentially, the ratio plotted in figure 4 should also grow roughly exponentially with an exponential growth rate of $n_U - n_b$ at large time. The difference $n_U - n_b$ is also listed in table 3 and the values are in good agreement with the slopes of the plotted curves. For a Gaussian profile
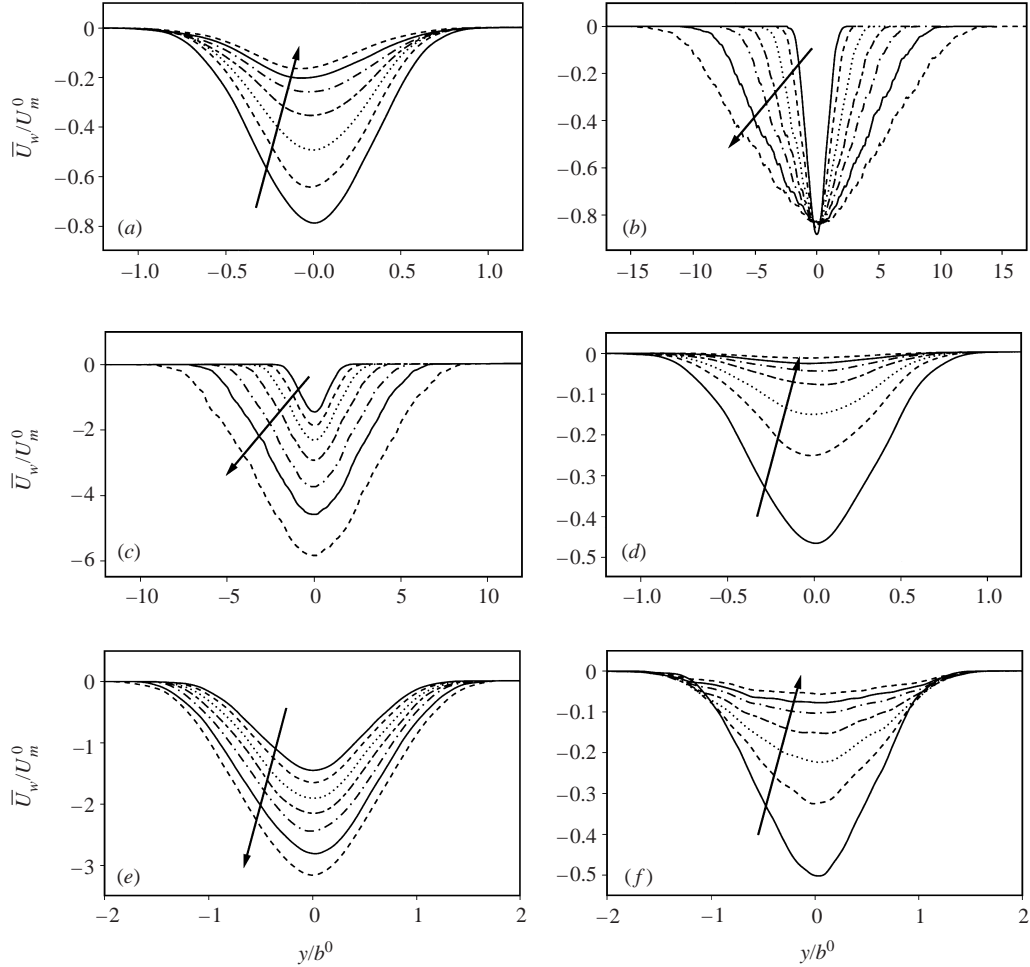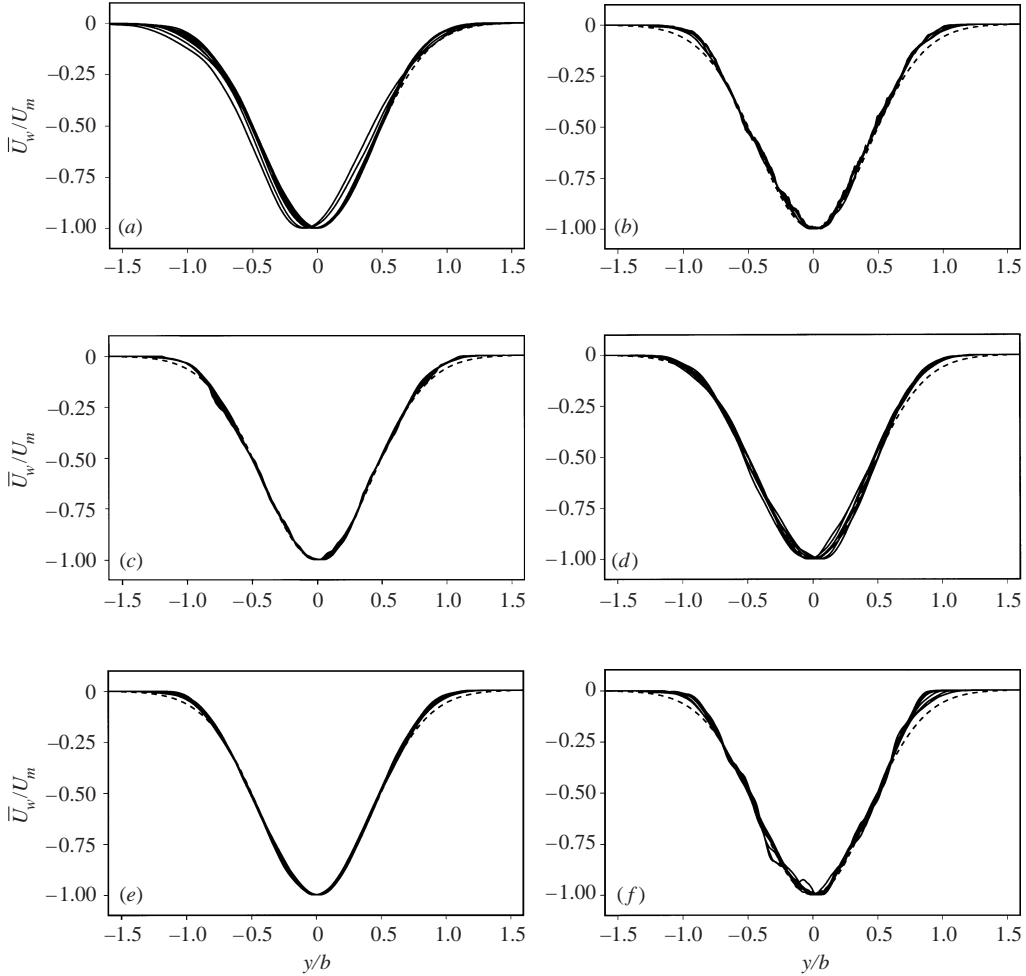
FIGURE 5. Wake mean velocity profiles at seven roughly equally spaced times between $\tau - \tau_1 = 1.8$ and the end of each simulation for (a) case A, (b) case B, (c) case C, (d) case D, (e) case E, and (f) case F. The arrows indicate the direction of change in time.

$f(\eta) = \exp(-4 \ln 2\eta^2)$, the maximum magnitude of $df/d\eta$ occurs where $\eta^2 = (8 \ln 2)^{-1}$ and equals $\sqrt{8 \ln 2/e} = 1.428$ (the maximum value is 1.509 for the Wygnanski *et al.* (1986) profile given below). The maximum shear rate to strain rate ratio is thus roughly 50% larger than the plotted values of $U_m/(ab)$.

The sign of the spanwise strain affects the initial response of the wake shear to the applied strain. For positive (expansive) spanwise strain (cases A and E) the wake shear suddenly increases relative to the unstrained wake (the slope is discontinuous in time). Conversely, for negative (compressive) spanwise strain (cases B and F) it suddenly decreases. The wake shear in the cases with no spanwise strain (cases C and D) initially evolves like that of the unstrained wake. This initial response to the applied strain should be predictable by rapid distortion theory.

The wake mean velocity profiles at seven roughly equally spaced times between $\tau - \tau_1 = 1.8$ and the end of each simulation are shown in figure 5. From this figure it is again apparent that the wake width for cases A and D is roughly constant, that the deficit for case B is roughly constant, and that the deficits for cases D and F are small

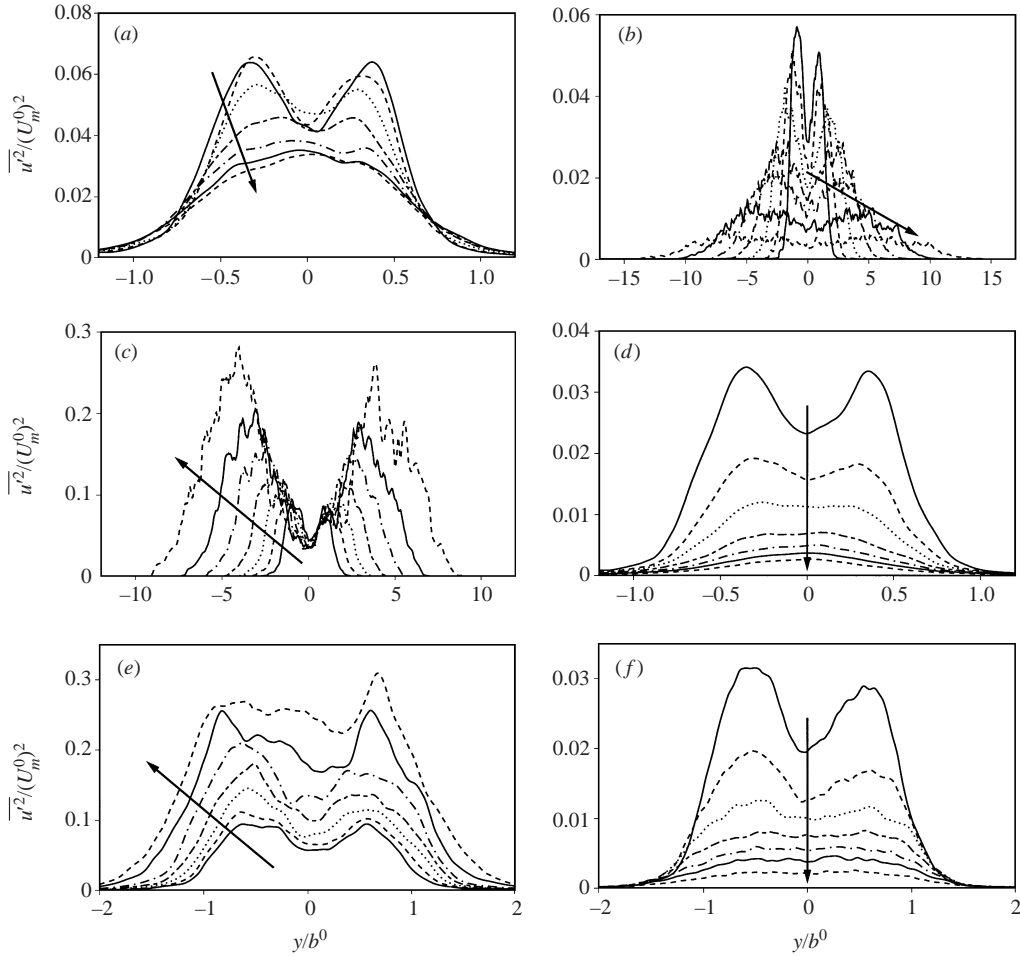FIGURE 6. Scaled wake mean velocity profiles at seven roughly equally spaced times between $\tau - \tau_1 = 1.8$ and the end of each simulation for (*a*) case A, (*b*) case B, (*c*) case C, (*d*) case D, (*e*) case E, and (*f*) case F. The dashed curve is the Gaussian $-\exp(-(4\ln 2)(y/b)^2)$.

at large times. It can also be seen that the shear associated with the wake profile in case C is constant (the curves are parallel) and that it is increasing in case E.

As noted previously, the exponential growth of Re_m for the strained wakes indicates that the mean velocity profiles for these cases are similar in shape. Normalizing the magnitudes of the mean velocity profiles by $U_m(t)$ and scaling their widths by $b(t)$ results in the profiles illustrated in figure 6. The collapse for all six cases is good. The dashed line in these figures represents a Gaussian profile. The strained wake profiles are indeed close to Gaussian in shape, except that they decay to zero slightly faster at the edges of the wake, as is the case with the mean profiles of unstrained wakes. Scaling by U_m and b collapses not only the mean profiles from a single simulation, but also those of all the simulations. By comparing the simulation profiles with the Gaussian curve for each case, it can be seen that the profile shape $f(\eta)$ (see equation (2.24)) is independent of the strain geometry and essentially the same as that of an unstrained wake, corresponding very well to the fit $f(\eta) = -\exp(-2.548\eta^2 - 0.896\eta^4)$ given by Wygnanski *et al.* (1986). Several investigators (e.g. Hill *et al.* 1963; Gartshore 1967;
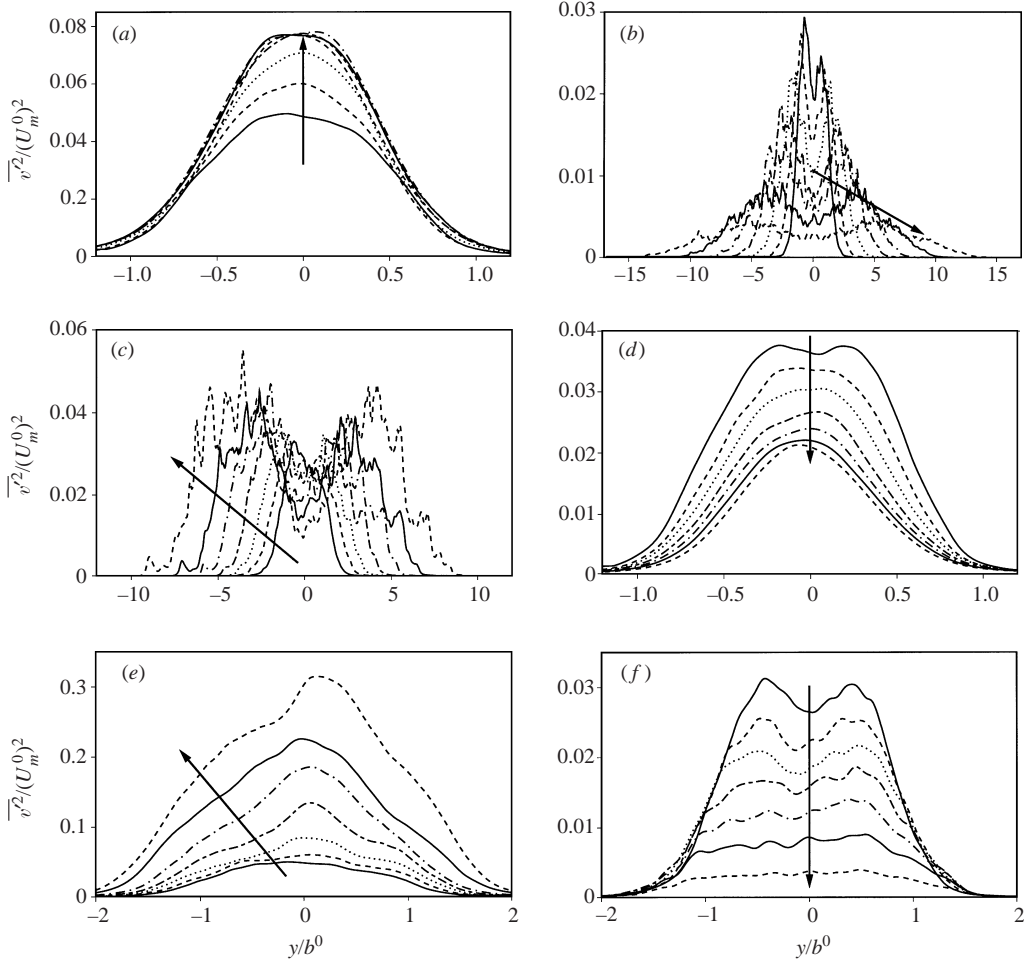
FIGURE 7. Mean $\overline{u'^2}$ profiles at seven roughly equally spaced times between $\tau - \tau_1 = 1.8$ and the end of each simulation for (*a*) case A, (*b*) case B, (*c*) case C, (*d*) case D, (*e*) case E, and (*f*) case F. The arrows indicate the direction of change in time.

Narasimha & Prabhu 1972; Prabhu & Narasimha 1972; Nakayama 1987; Nayeri *et al.* 1996; and Beharelle *et al.* 1996) have found a similar insensitivity of the mean velocity profile shape to streamwise pressure gradients, streamwise curvature and cross-plane shear.

4.1.2. *The Reynolds stresses*

The time evolution of the $\overline{u'^2}$ profiles for each of the six plane strain geometries is shown in figure 7. For cases A, B, D and F this Reynolds stress decreases as the flow evolves and, with exception of case B, the profiles for these cases change from the double-humped shape typical of unstrained wakes to a single-humped profile with a maximum near the centreline. As seen in figure 4, for these four flows the wake shear rate continually diminishes relative to the applied strain rate. For cases C and E, the cases in which $a_{11} < 0$, $\overline{u'^2}$ increases and the double-humped character of the profiles is maintained, as is the relative importance of the wake shear relative to the applied

FIGURE 8. Mean $\overline{v'^2}$ profiles at seven roughly equally spaced times between $\tau - \tau_1 = 1.8$ and the end of each simulation for (*a*) case A, (*b*) case B, (*c*) case C, (*d*) case D, (*e*) case E, and (*f*) case F. The arrows indicate the direction of change in time.

strain. Despite the three-fold increase in the peak levels of $\overline{u'^2}$ for case C over the time shown, the value at the centreline actually decreases by about 20%.

Profile evolutions for $\overline{v'^2}$ are shown in figure 8. Again the profile levels for cases C and E are increasing in time, whereas those for the other cases are generally decreasing. An exception to this is the $\overline{v'^2}$ profile evolution for case A, which initially is increasing before becoming constant for the last four times shown. As will be discussed later, this results from the production of $\overline{v'^2}$ by the global strain, which is large enough, at least during the time period simulated, to counteract the general downward trend of the Reynolds stresses in this case. The $\overline{v'^2}$ profile of an unstrained wake is single-peaked with a maximum near the centreline. This form is maintained in cases A, D and E, but cases B, C and F become double-peaked as a result of the applied strain (although case F may be reverting to a single-peaked profile at late times). This is especially pronounced in case C, where the value of $\overline{v'^2}$ at the centreline decreases in time (by about 65% over the time interval in the figure) despite
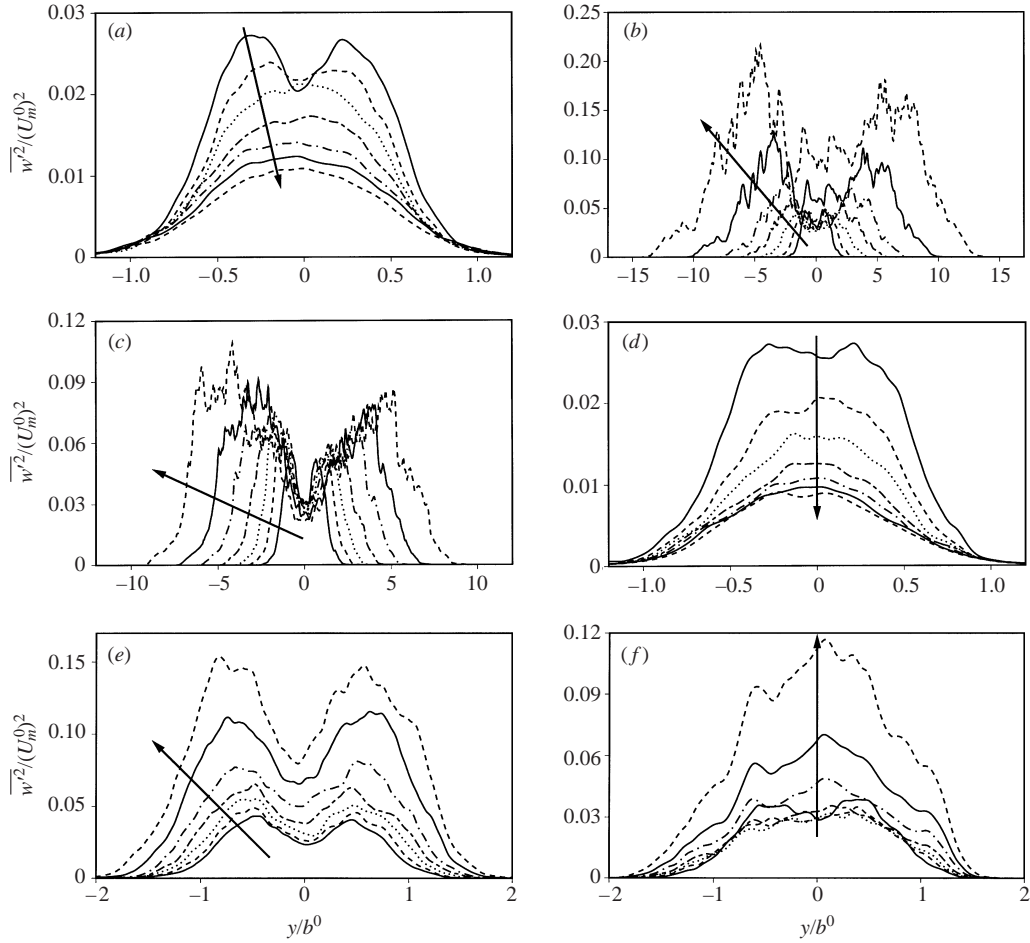
FIGURE 9. Mean $\overline{w'^2}$ profiles at seven roughly equally spaced times between $\tau - \tau_1 = 1.8$ and the end of each simulation for (*a*) case A, (*b*) case B, (*c*) case C, (*d*) case D, (*e*) case E, and (*f*) case F. The arrows indicate the direction of change in time.

the general increase in the profile levels. Indeed it appears that case C is evolving towards a flow that consists of two active regions away from the centreline, separated by a relatively weakly turbulent zone in between. This is also apparent in the flow visualizations shown in §4.4 and becomes more prevalent at later times (quantified later in figure 22).

The $\overline{w'^2}$ profiles are shown in figure 9. Unlike for the other two normal stresses, the $\overline{w'^2}$ levels are increasing in cases B and F (the two cases with compression in the spanwise direction, and therefore with production of $\overline{w'^2}$ by the mean strain) as well as in cases C and E. For cases B and F, $\overline{w'^2}$ becomes the only significant Reynolds stress at large total strains. The $\overline{w'^2}$ profiles of unstrained wakes are typically double-peaked. As observed for $\overline{u'^2}$, in Cases B, C and E the double-peaked character of the $\overline{w'^2}$ profile is maintained, whereas in cases A, D and F the profiles become single-peaked. As with $\overline{u'^2}$ and $\overline{v'^2}$, the centreline value of $\overline{w'^2}$ for case C decreases in time (by about
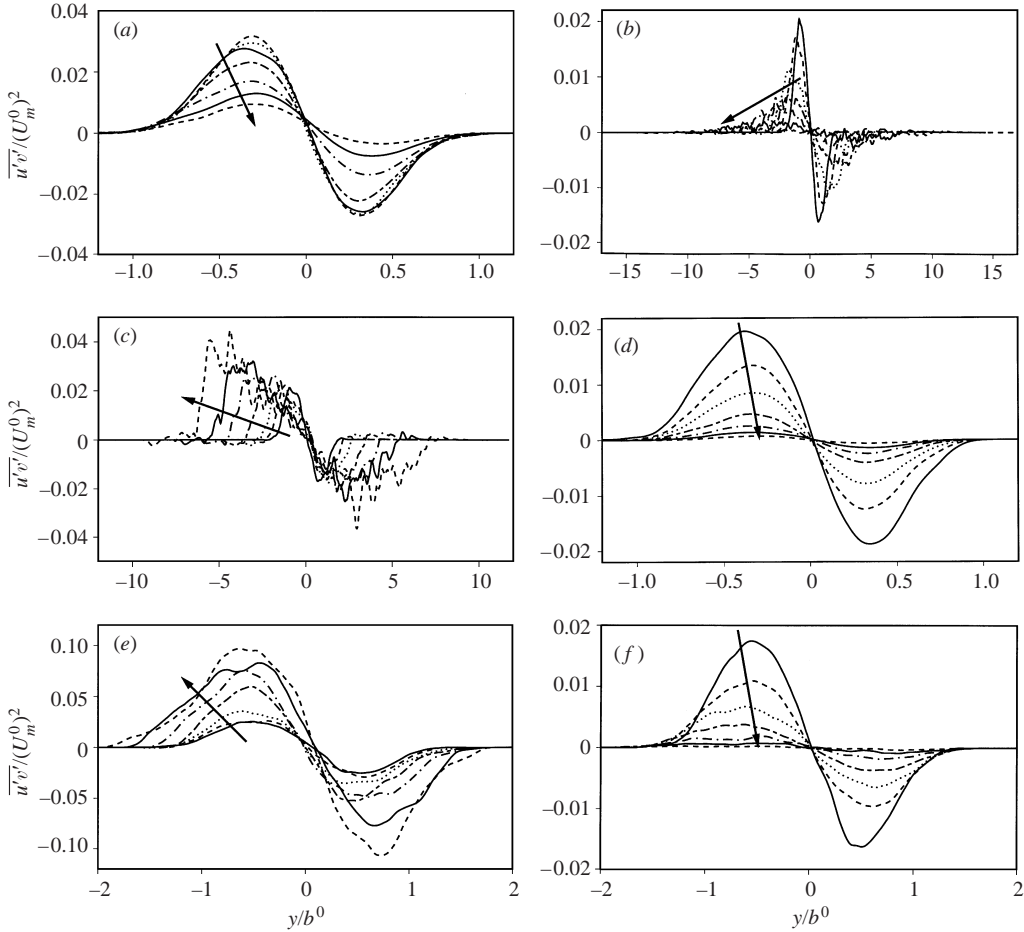
FIGURE 10. Mean $\overline{u'v'}$ profiles at seven roughly equally spaced times between $\tau - \tau_1 = 1.8$ and the end of each simulation for (*a*) case A, (*b*) case B, (*c*) case C, (*d*) case D, (*e*) case E, and (*f*) case F. The arrows indicate the direction of change in time.

25% over the period shown) despite the generally increasing level of this Reynolds stress at other y-locations.

Like all the normal stresses, the Reynolds shear stress $\overline{u'v'}$ increases with time for cases C and E (figure 10). For the other four flows (in which $a_{11} \geqslant 0$), the shear stress decays, as expected from the decay of the wake shear for these cases (see figure 4). For cases B, D and F, $\overline{u'v'}$ decays essentially to zero by the end of each simulation. For case A the decay is slower owing to a delay in the initiation of this decay. The level of $\overline{u'v'}$ does not begin to drop until $\tau - \tau_1 \approx 4$, presumably because for this case the shear stress is produced by the global strain as well as by the wake shear. This delayed decay is also apparent in the wake shear rate plotted in figure 4.

From the above examination it is clear that the form of the Reynolds stress tensor varies widely between the different cases. In order to more easily visualize the relative amplitudes of the Reynolds stress components at large total strain, all four stresses are plotted together for each case at the final time t_f of each simulation in figure 11. The relative amplitudes can also be assessed by examining the Reynolds stress anisotropies plotted in figure 30 of Appendix D. As noted previously, for cases B and F (the cases
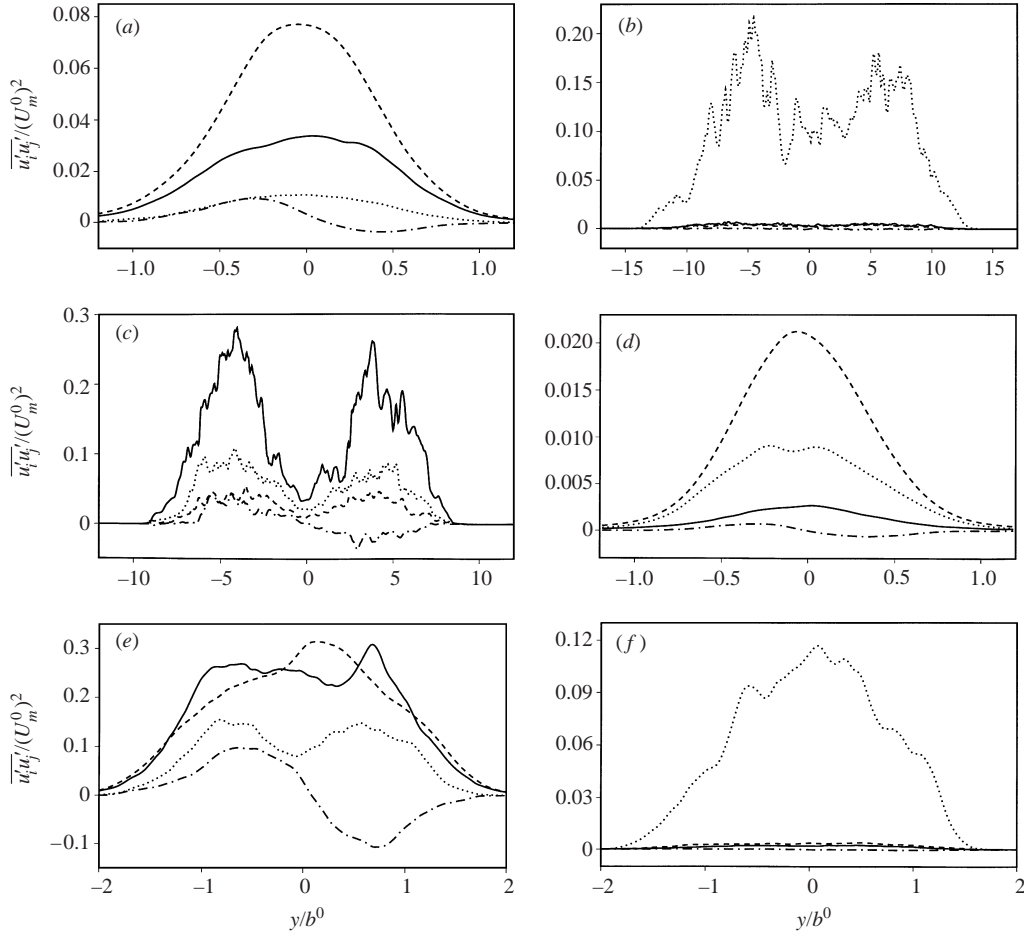
FIGURE 11. Reynolds stress profiles: ——, $\overline{u'^2}$; –––, $\overline{v'^2}$; ······, $\overline{w'^2}$; —·—, $\overline{u'v'}$ at the final time t_f of each simulation for (a) case A ($\tau - \tau_1 = 7.75$), (b) case B ($\tau - \tau_1 = 8.49$), (c) case C ($\tau - \tau_1 = 7.01$), (d) case D ($\tau - \tau_1 = 8.49$), (e) case E ($\tau - \tau_1 = 5.72$), and (f) case F ($\tau - \tau_1 = 8.49$).

with compression in the spanwise direction) the only non-negligible component of the Reynolds stress tensor at late times is $\overline{w'^2}$. These two cases have evolved to pure straining flows with no significant wake shear or Reynolds shear stress. For cases C and E (compression in the streamwise direction) all components of the Reynolds stress tensor grow and all remain significant throughout the simulations. Cases A and D (compression in the cross-stream direction) exhibit qualitatively similar profiles, but with the roles of $\overline{u'^2}$ and $\overline{w'^2}$ interchanged. For these two flows, $\overline{v'^2}$ is produced by the global strain and this term dominates the Reynolds stress tensor. The decay of the wake shear rate in these two cases suggests that $\overline{u'v'}$ will continue to decay to insignificant levels with further straining, again resulting in pure straining flows. Also apparent in these late-time profiles is the poor statistical sample for cases B and C (stretched in the cross-stream direction) and, to some extent, cases E and F (no strain in the cross-stream direction) as mentioned in §3.3 and in the discussion of figure 2.

For three of the six strain geometries, the growth or decay of some of the Reynolds stresses $\overline{u'_i u'_j}$ does not follow the behaviour of U_m. In particular, in case A, $\overline{v'^2}$ increases

while U_m decreases, for case F, $\overline{w'^2}$ increases while U_m decreases, and for case B, U_m is constant but all of the Reynolds stresses decrease except for $\overline{w'^2}$, which increases markedly. The strain production of Reynolds stress is responsible for this. From equations (2.22) it can be seen that compression in a particular coordinate direction will result in production of velocity fluctuations in that direction and, conversely, stretching will reduce the fluctuation intensity. Spanwise stretching will produce Reynolds shear stress $\overline{u'v'}$, whereas spanwise compression will destroy it. For cases A, B and F, the strain production of the Reynolds stresses outpaces the Reynolds stress decay associated with unstrained wakes and, for at least some time after the application of the strain, the trends in R_{ij} for these cases are predicted by the sign of the strain production.

It should be noted that the small-scale turbulence is more isotropic. All the components of the enstrophy tensor $\overline{\omega_i'\omega_j'}$ for cases C and E increase in time (although only modestly for case C), whereas those for the other cases all decay (here the enstrophy is denoted by ω^2, where $\omega^2 = \overline{\omega_i'\omega_i'}$). For each case the normal components of $\overline{\omega_i'\omega_j'}$ are comparable, with none being more than a few times larger than the others. The more isotropic character of the small scales is also apparent in the relatively weak anisotropy of the dissipation-rate tensor, the components of which are plotted in figure 31 of Appendix D.

4.1.3. *Similarity predictions for the Reynolds stresses*

The evolution of the Reynolds stresses for most of the cases described in § 4.1.2 clearly cannot be predicted by classical self-similar analysis. The different Reynolds stress components do not all grow or decay at the same rate and their evolutions are not characterized by the square of the single velocity scale U_m. The more general equilibrium similarity solutions, however, do predict that the various components of the Reynolds stress tensor evolve differently. These components are not all assumed to scale as U_m^2 as part of the similarity analysis.

Despite this added generality of the equilibrium similarity solutions, the Reynolds stress profiles cannot be self-similar throughout the entire periods simulated because the single-peaked or double-peaked character of at least one of the normal Reynolds stress profiles changes during the evolution (except for case E). Therefore these profiles cannot be collapsed by a rescaling of magnitude and width, as required by equation (2.28a). However, in other self-similar flows it is often observed that self-similar evolution of the Reynolds stress profiles requires a longer flow development time to become established than that required for similarity of the mean velocity profile. From figures 2 and 3 it appears that self-similar evolution of the mean velocity profile width and deficit does not occur until $\tau \approx 6$. Changes in the overall shape (single-peaked or double-peaked) of the Reynolds stress profiles are generally complete not long after this ($\tau \approx 8$ or 9), suggesting that continued evolution may indeed ultimately result in similarity of the Reynolds stress profiles for all cases.

For cases C and E, all the Reynolds stresses increase in magnitude as time progresses, as does the deficit U_m. It might thus be anticipated that the classical similarity solution (2.45) applies for these cases. Examination of figure 12 suggests that all the Reynolds stresses in case E do indeed scale like U_m^2, but the exponential $e^{at/2}$ growth predicted for the wake width in this case is inconsistent with the observed $t^{1/2}$ behaviour in the computations. The Reynolds stresses in case C are not increasing as rapidly as predicted by the classical self-similar analysis. The exponents C_{ij} in equation (2.39) are closer to a than to the predicted value of $2a$ during the simulated
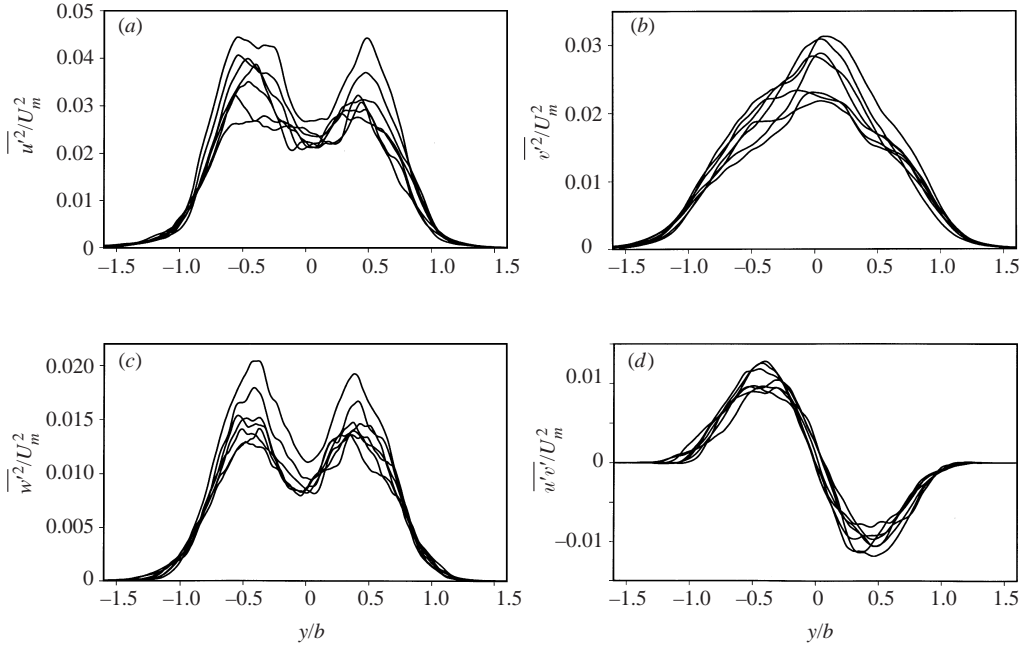
FIGURE 12. Scaled Reynolds stress profiles (a) $\overline{u'^2}/(U_m)^2$, (b) $\overline{v'^2}/(U_m)^2$, (c) $\overline{w'^2}/(U_m)^2$ and (d) $\overline{u'v'}/(U_m)^2$ at seven roughly equally spaced times between $\tau - \tau_1 = 1.8$ and the end of the simulation ($\tau - \tau_1 = 5.72$) for case E.

period. Additionally, the classical analysis is internally inconsistent for this case with $a_{11} + a_{22} = 0$, as discussed previously.

Case E is the only case in which the wake shear rate increases in time, increasing in importance relative to the constant applied strain rate. As such, this case could perhaps be expected to ultimately evolve like an unstrained wake, albeit one with an increasing wake deficit and shear rate rather than decreasing as for an unstrained case. Indeed there are similarities between the observed evolution in case E and that of unstrained wakes. The wake spreading rate for case E is better described by $\tau^{1/2}$ behaviour like that of unstrained wakes, rather than by exponential growth (see figure 2). Note, however, that such $\tau^{1/2}$ behaviour is also predicted by the equilibrium similarity solution (2.55) and is thus not only associated with unstrained wakes. The Reynolds stress profiles for this case maintain the same double-peaked ($\overline{u'^2}$ and $\overline{w'^2}$) or single-peaked ($\overline{v'^2}$) character exhibited by the corresponding profiles in an unstrained wake. Additionally, scaling the Reynolds stresses by U_m^2 for this case (as for an unstrained wake) does a reasonable job of collapsing the case E profiles in figures 7 to 10, particularly for late times (see figure 12). Although the shapes of the profiles in figure 12 are similar to those observed in unstrained wakes, the levels of these profiles are a factor of two or more lower than the corresponding levels in the unstrained case (see Moser *et al.* 1998). This is presumably due to the time lag between the change in the wake velocity deficit and the resulting change in Reynolds stress levels. Because the wake deficit is increasing in case E, the ratio $\overline{u'_i u'_j}/U_m^2$ is smaller than in an unstrained wake, in which the wake deficit decreases.

Given that the equilibrium similarity solution (2.55) was found to describe the wake mean velocity profile evolution in all of the cases, it is of interest to determine whether the observed Reynolds stress behaviour is predicted by this solution as well.

Because similarity of the Reynolds stress profiles requires longer evolution times than those required for similarity of the mean velocity profile, incomplete agreement with the simulations might be anticipated, particularly given that for several of the cases the computational domain size may be affecting the results for long times. Additionally, it has already been pointed out above that, at least in some of the flows, qualitative changes in the character of the Reynolds stress profiles may still be occurring, preventing the similarity assumption (2.28*a*) from being completely accurate. Thus complete similarity through to the level of the Reynolds stress profiles may not be achieved in all of the computations.

Comparing the Reynolds stress predictions of the similarity solutions (2.55) and (2.54) to the observed behaviour in the computations is not trivial. Even if appropriate values of E_1, E_2 and E_3 (or D_1, D_2 and D_3) have been determined, a virtual origin for the initiation of self-similar evolution and the initial values b^0, U_m^0 and K_{ij}^0 at that time still need to be chosen. The similarity solution can be more easily compared to the computational results if the asymptotic long-time behaviour is considered, the drawback of this being that the simulation data are probably not in such an asymptotic state by t_f. Nevertheless, the long-time behaviour of the Reynolds stresses predicted by the equilibrium similarity solutions (2.54) and (2.55) can be compared with the long-time trends in the computations, providing further insight into which solution, if any, applies in each case. As will be seen below, for all the cases it is possible to find an equilibrium similarity solution that predicts the observed mean flow behaviour and gives reasonable predictions of whether a particular Reynolds stress component will ultimately increase, decrease, or tend to a constant value.

The evolution of the Reynolds shear stress $\overline{u'v'}$ given by the similarity solution (2.55) is independent of the chosen values of E_2 and E_3. Similarly, the $\overline{u'v'}$ predictions of equation (2.54) do not depend on D_1, D_2 and D_3. For this component of the Reynolds stress tensor, the observed long-time behaviour in all the cases is qualitatively described well by equation (2.55), although for case C, $\overline{u'v'}$ is still weakly increasing at the end of the simulation, whereas it should ultimately become constant according to the similarity solution. However, the solution (2.54) also does a reasonable job of describing the observed long-time behaviour of $\overline{u'v'}$ for all cases except A and D. In fact, the long-time predictions of these two similarity solutions are the same when $a_{22} > 0$ and nearly the same when $a_{22} = 0$ (a factor of t difference between the predicted exponential behaviours for non-zero E_1), indicating that the long-time behaviour of $\overline{u'v'}$ cannot be used to determine which equilibrium similarity solution better describes the observed evolution when $a_{22} \geqslant 0$.

The values of E_2 and E_3 do affect the self-similar behaviour of the normal Reynolds stresses predicted by equation (2.55), but only have an impact on the leading-order long-time behaviour of these stresses when $a_{22} < 0$ (and, exceptionally, for $\overline{v'^2}$ when $a_{22} = 0$). Likewise, the values of D_1, D_2 and D_3 affect the normal Reynolds stress evolution in equation (2.54), but only change the predicted long-time trends by a multiplicative constant. Thus to compare the long-time equilibrium similarity solution predictions to the observed computational behaviour or to each other, it is only necessary to select E_2 and E_3 when $a_{22} < 0$ (or when $a_{22} = 0$ for $\overline{v'^2}$ comparisons).

For the cases in which $a_{22} < 0$ (cases A and D), only solution (2.55) with $E_2 = \frac{1}{2}$ describes the observed mean profile evolution accurately. It is thus of great interest to determine whether the Reynolds stress evolution for these cases is also predicted well by solution (2.55). Both $\overline{u'v'}$ and U_m are predicted to decay ultimately like e^{-at} for case A and like e^{-2at} for case D. Their ratio should thus approach a constant, as observed
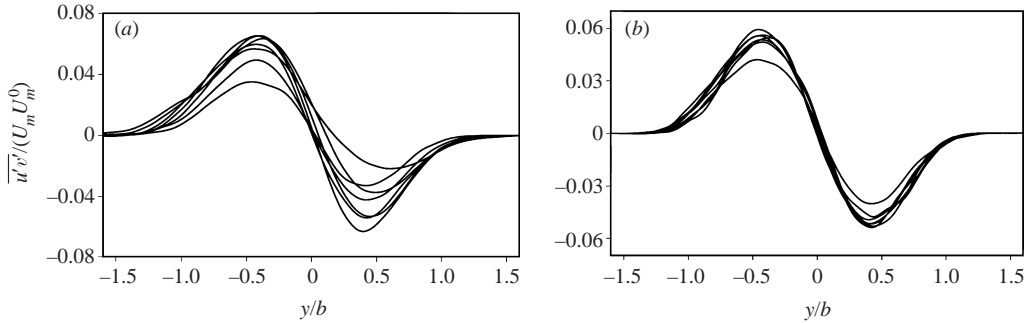
FIGURE 13. Alternatively scaled Reynolds shear stress profiles $\overline{u'v'}/(U_m U_m^0)$ for (*a*) case A and (*b*) case D at seven roughly equally spaced times between $\tau - \tau_1 = 1.8$ and the end of each simulation.

in the simulations (figure 13). For these two cases, the compressive straining in the vertical direction results in the dominance of $\overline{v'^2}$, which is predicted to approach a constant by the similarity solution (despite decaying U_m). For case A, $\overline{v'^2}$ does indeed approach a constant, while in case D it is decaying only slowly at the end of the simulation. In fact, if one takes $E_3 > -1$ for case A and $E_3 \geqslant 0$ for case D, then the long-time behaviour of all four non-zero Reynolds stresses is qualitatively predicted well by the general equilibrium similarity solution (2.55). These results are in contrast to the Reynolds stress predictions of solution (2.54), which indicate growing (case A) or constant (case D) $\overline{u'v'}$ and rapidly growing $\overline{v'^2}$ (cases A and D), in complete disagreement with the simulation results.

With $\overline{v'^2}$ approximately constant and the other Reynolds stresses decaying in cases A and D, the pressure–strain condition (2.44) $C_{11} = C_{22} = C_{33}$ cannot be satisfied. Because none of the pressure–strain terms is negligible, this can only occur if the pressure–strain profiles (see Appendix D) are not self-similar. Direct examination of these profiles shows that this is indeed the case. For example, in case A the pressure–strain is transferring energy out of $\overline{u'^2}$ and into $\overline{v'^2}$ and $\overline{w'^2}$ at $\tau = 3.75$ but transferring energy out of $\overline{v'^2}$ and into $\overline{u'^2}$ and $\overline{w'^2}$ by the end of the simulation at $\tau = 7.75$, when $\overline{v'^2}$ has become the largest R_{ij} component. Thus a critical assumption used in deriving the classical similarity solution is not valid during much of this simulation. The general similarity solution (2.55), on the other hand, does not require that the pressure–strain terms evolve self-similarly, but rather that they combine with the turbulent transport and dissipation terms to scale like other combinations of terms in the governing equations.

For the cases in which $a_{22} > 0$ (cases B and C), the mean profile evolution is described well by both similarity solutions (2.54) and (2.55). Both equilibrium similarity solutions predict the same leading-order long-time behaviour for all four Reynolds stresses for case B. These predictions are in reasonable agreement with the computations, although the levels of $\overline{u'^2}$ are still increasing at the end of the simulation and have not yet reached the predicted constant value. Since the long-time Reynolds stress predictions are the same for this case, they cannot be used to determine which solution better describes the computational results.

For case C, the long-time Reynolds stress predictions of the two equilibrium similarity solutions are the same for $\overline{u'v'}$ and $\overline{u'^2}$, but different for $\overline{v'^2}$ and $\overline{w'^2}$. The similarity solution (2.55) predicts the ultimate decay of $\overline{v'^2}$, whereas the computations

indicate an increase, perhaps approaching the constant value $-D_2 K_{22}^0$ predicted by solution (2.54). The continued increase of $\overline{w'^2}$ observed in the computations is in better agreement with the linear increase $K_{33}^0(1 + D_3 t)$ predicted by solution (2.54) than with the constant value predicted by solution (2.55). In this case, the computational results are perhaps better described by the solution (2.54), although this conclusion should be drawn tentatively, given the uncertainty regarding the applicability of 'long-time' predictions to the computational data.

When $a_{22} = 0$ the solution (2.54) predicts that the wake width should become constant. This is not too different from the observed slowly varying $t^{1/2}$ behaviour, so the applicability of this solution to cases E and F should perhaps not be ruled out, although the similarity solution (2.55) apparently better describes the evolution of the mean velocity profile. The mean flow results for cases E and F suggest that E_2 should be about $\frac{1}{2}$, as was the case when $a_{22} < 0$. For case E, the exponential long-time behaviour predicted for $\overline{u'^2}$ and $\overline{u'v'}$ by both solutions (2.54) and (2.55) is the same (up to a factor of t or t^2), but solution (2.54) predicts exponential growth for $\overline{v'^2}$ and $\overline{w'^2}$ when D_2 and D_3 are not zero, whereas solution (2.55) predicts the ultimate decay of these Reynolds stresses (albeit a potentially delayed decay for $\overline{w'^2}$ when E_1 is large (positive) and E_3 is negative). The computational results, which indicate that all the Reynolds stresses increase like U_m^2, are thus in better agreement with solution (2.54).†

For case F, both solutions (2.54) and (2.55) predict the same long-time exponential behaviour for all the Reynolds stresses except $\overline{v'^2}$ (again up to factors of t, t^2 or t^{E_3}). The stresses $\overline{u'v'}$ and $\overline{u'^2}$ are expected to decay, whereas $\overline{w'^2}$ should ultimately grow rapidly, as observed in the simulations. Solution (2.54) requires that $\overline{v'^2}$ approach a constant, while from solution (2.55) a $1/t$ decay is expected when $E_2 = \frac{1}{2}$. The sustained decay of $\overline{v'^2}$ in the computations (figure 8f) suggests that the behaviour in this case is better described by solution (2.55). However, it should be remembered that solution (2.54) can be generalized if the pressure–strain terms are not required to separately scale like the other terms in the equation. In this case, all time-evolution behaviours of $\overline{v'^2}$ and $\overline{w'^2}$ satisfy the self-similar constraints and this generalized form of similarity solution (2.54) could apply in case F.

In summary, the observed flow evolution in the simulations is very different from that predicted by classical self-similar analysis. The evolution of the wake mean velocity profile is well described for all the cases by the equilibrium similarity solution (2.55) (with $E_2 = \frac{1}{2}$ when $a_{22} \leqslant 0$) as well as by the equilibrium similarity solution (2.54) for the cases in which $a_{22} \geqslant 0$. By the end of the simulations, complete similarity of the Reynolds stress profiles has probably not been attained for most of the cases considered. Despite this, the predictions of the solution (2.55) for the Reynolds stress components are overall quite good, being much more accurate than the U_m^2 scaling for all components predicted by classical self-similar analysis. However, cases C and E may be better described by solution (2.54), and case B can apparently be described by either of these two solutions. As pointed out in §2.2.2, for the similarity solution (2.54), cases C and E are the only two cases in which the viscous diffusion of $\overline{w'^2}$ can

† Note that for case E solution (2.54) predicts that the normal Reynolds stresses scale like U_m^2, but that the Reynolds shear stress $\overline{u'v'}$ increases like U_m. However, normalizing the data in figure 12(d) by $U_m U_m^0$ as in figure 13, rather than by U_m^2, also results in reasonable collapse of the curves at long times. Given the smaller value of t_f for case E, it is difficult to determine which of these normalizations better fits the long-time results.
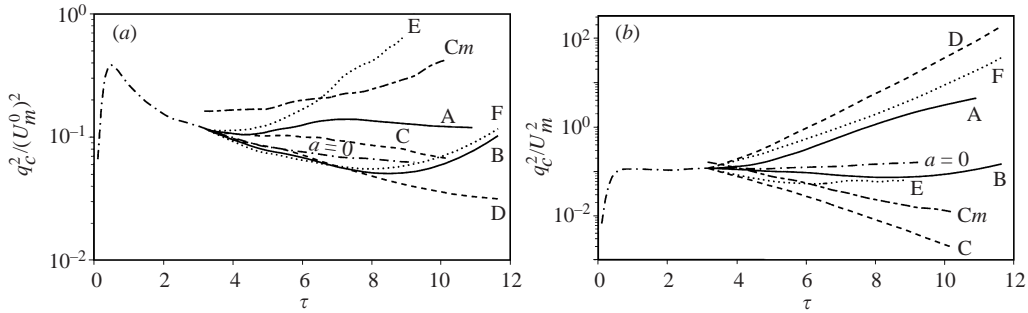
FIGURE 14. Time evolution of (twice the) turbulence kinetic energy at the wake centreline: (a) $q_c^2/(U_m^0)^2$ and (b) q_c^2/U_m^2. ——, Cases A (upper curve) and B (lower curve); ————, cases C (upper curve in (a) and lower curve in (b)) and D (other dashed curve); ······, cases E (upper curve in (a) and lower curve in (b)) and F (other dotted curve); and —·—, unstrained wake. Also shown for case C are the same quantities calculated with q_m^2 instead of q_c^2 (—–—). Note the higher initial value of the curves involving q_m^2.

be balanced by the other terms in the Reynolds stress evolution equation while still satisfying the pressure–strain condition (2.43).

For long times, only case C maintains a balance between the wake shear and the applied strain, and thus perhaps sustained 'strained wakes' are only possible for this strain configuration (the temporally evolving analogue of a wake developing in an adverse pressure gradient). The other flows are apparently moving towards alternative similarity states (that of an unstrained wake with increasing velocity deficit for case E, pure straining flows with only spanwise velocity fluctuations for cases B and F, and pure straining flows dominated by vertical velocity fluctuations for cases A and D). This change in character during the flow evolution, even if in accord with an equilibrium similarity solution, is likely to make modelling the turbulence in such flows difficult.

4.1.4. *Time evolution of other turbulence statistics*

Because the strained wakes are not evolving in accordance with the classical self-similar solution, the time evolutions of the Reynolds stresses (and therefore also of q^2) do not, in general, scale with U_m^2. The lack of complete self-similarity of the Reynolds stress profiles implies that these profiles cannot be characterized by a single velocity scale. Nevertheless, it is useful to examine the time evolution of some representative level of the profiles and for this purpose the centreline values (indicated by a subscript c) are used. For case C, where the centreline values evolve differently from the peak levels, the evolutions at the location of maximum q^2 are also tracked. This maximum value of q^2 is denoted by q_m^2. How well the centreline and maximum values represent the general level of the various profiles can be assessed by examining figures 7 to 10. Note that for cases A, D and F the maximum value of q^2 eventually occurs at the centreline because the normal Reynolds stress profiles become single-peaked. The profiles remain double-peaked for cases B and E (only moderately so for case E), but the trends for both q_c^2 and q_m^2 are similar in these cases. The profiles for case C are also double-peaked, but the evolutions of the values at the peak and at the centreline are different, as noted previously and discussed further in §4.3.

The time evolutions of various turbulence statistics are shown in figures 14 to 17. Results are shown for the unstrained wake (chain-dotted line) as well as for the six strained cases. For case C, statistics computed with both the centreline values (q_c^2, ϵ_c
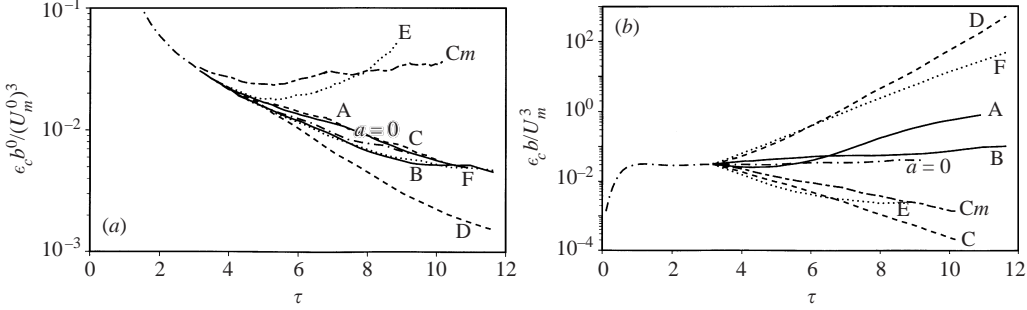
FIGURE 15. Time evolution of turbulence kinetic energy dissipation rate at the wake centreline: (*a*) $\epsilon_c b^0/(U_m^0)^3$ and (*b*) $\epsilon_c b/U_m^3$. ——, Cases A (upper curve) and B (lower curve); – – – –, cases C (upper curve in (*b*) and lower curve in (*B*)) and D (other dashed curve); · · · · · ·, cases E (upper curve in (*a*) and lower curve in (*b*)) and F (other dotted curve); and — · —, unstrained wake. Also shown for case C are the same quantities calculated with ϵ_m instead of ϵ_c (— · —).

and ω_c^2) and the values at the location of maximum q^2 (q_m^2 and ϵ_q) and maximum ω^2 (ω_m^2) are plotted.

The evolution of twice the turbulent kinetic energy (per unit mass) q^2 is shown in figure 14. The value of q^2 typically does not vary as rapidly as that of U_m^2, with at most about a factor of five change in q^2 over the course of each simulation (figure 14*a*). The strongest growth occurs in case E and at late times for cases B and F. The ratio q_c^2/U_m^2 is constant for the classical self-similar solution (2.45) derived in §2.2. Examination of figure 14(*b*) confirms that the strained wakes are generally not evolving in accordance with this solution. The ratio q_c^2/U_m^2 is roughly constant for case E (as expected from the results presented in figure 12) and the unstrained wake, but not for the other flows. The ratio is roughly constant in case B, but this is a temporary situation, resulting from the growth of $\overline{w'^2}$ offsetting the decay of $\overline{u'^2}$ and $\overline{v'^2}$; once these two Reynolds stresses become insignificant near the end of the simulation $\overline{w'^2}$ and q_c^2/U_m^2 begin to grow rapidly, with C_{33} approaching $2a$. The remaining cases A, C, D and F exhibit periods of apparent exponential change in the ratio q_c^2/U_m^2. Note that the cases with decreasing velocity deficits (D, F and A) exhibit increasing q_c^2/U_m^2, whereas those with increasing deficits (E and C) have decreasing q_c^2/U_m^2 (or nearly constant for late times in case E). This indicates that, except possibly for case E, the net turbulence production or dissipation cannot keep pace with the rapidly changing mean flow.

Although q^2 is not changing as rapidly as U_m^2, it is changing at a rate consistent with the general equilibrium similarity predictions. When $a_{22} \geqslant 0$, the q^2 evolutions predicted by solutions (2.54) and (2.55) are the same, being proportional to e^{2at} (with perhaps extra factors of t when $a_{22} = 0$). The long-time behaviour of cases B, C, E and F shown in figure 14(*a*), although perhaps not yet fully in the asymptotically large time limit, is consistent with such exponential growth (where for case C the maximum levels, representative of the overall profile levels, are considered). The predictions of the two similarity solutions are not the same when $a_{22} < 0$, as discussed in §4.1.2. For these cases (A and D), only solution (2.55) with $E_2 = \frac{1}{2}$ describes the observed behaviour in the simulations, predicting that q^2 should approach a constant (assuming that $E_3 \geqslant -1$ for case A and $E_3 \geqslant 0$ for case D) rather than grow like e^{2at} as predicted by solution (2.54).

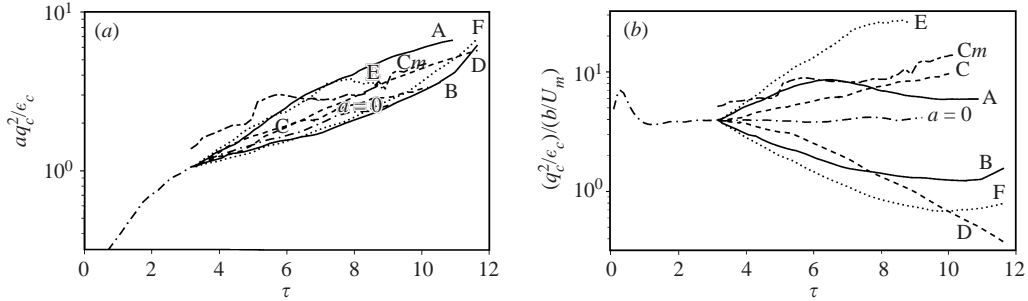The dissipation rate ϵ is plotted in figure 15(*a*). For the four strained flows in

FIGURE 16. Time evolution of the turbulence time scale at the wake centreline: (*a*) aq_c^2/ϵ_c and (*b*) $(q_c^2/\epsilon_c)/(b/U_m)$. ——, Cases A (upper curve) and B (lower curve); – – – –, cases C (upper curve in (*b*) and early times in (*a*), lower curve at late times in (*a*)) and D (other dashed curve); ······, cases E (upper curve) and F (lower curve); and —·—, unstrained wake (using same value of *a* in (*a*)). Also shown for case C are the same quantities calculated with q_m^2 and ϵ_q instead of q_c^2 and ϵ_c (—··—). Note the higher initial value of the curves involving q_m^2.

which the wake shear decays, ϵ decreases roughly as for the unstrained wake. Both the wake shear and ϵ increase in case E and both are about constant in case C (the peak value ϵ_m showing a slight increase and the centreline value ϵ_c decreasing for this latter case). It should be noted, however, that while these values may not differ from their unstrained counterparts in many cases, these levels are sustained across strained wakes of very different widths than that of the unstrained wake.

The evolution of the dissipation rate normalized by the local wake width and velocity deficit is shown in figure 15(*b*). In general, the ordering of the different cases is the same as that observed for q^2/U_m^2 in figure 14(*b*). Again, several of the flows have periods of approximate exponential growth. According to classical self-similar scaling, the ratio $\epsilon b/U_m^3$ should be constant for similarity. In case B it is roughly constant, but this is a temporary situation, as noted above. The value in case E approaches a constant during the latter part of the simulation, as seen for q^2/U_m^2. For the other cases ϵ does not scale like U_m^3/b at any time during the evolution.

The centreline value of the turbulence time scale q^2/ϵ is compared to the time scale of the constant and uniform strain rate $1/a$ and to the time scale associated with the mean wake shear rate b/U_m in figures 16(*a*) and 16(*b*) (these two mean time scales were compared to each other in figure 4). Because *a* is constant, the time scale q_c^2/ϵ_c evolves like the ratio aq_c^2/ϵ_c shown in figure 16(*a*). The value of the turbulence time scale increases for all the flows examined and is relatively similar to the value in the unstrained wake (although the value in case A approaches twice the unstrained value). Note that the relative insensitivity of the time scale to the orientation of the strain results in curves in figure 16(*b*) that are in the same relative order as those in figure 4. From figure 16(*a*) it can also be seen that the time scale evolutions for cases A and E, the flows with expansive strain in the span, are very similar for much of the flow evolution and slightly higher than the other curves. Likewise, cases B and F, with compressive strain in the span, exhibit similar evolution at slightly lower values of the time scale ratio (close to that of the unstrained wake). Note that the dimensionless quantity aq_c^2/ϵ_c can be written as

$$\frac{aq_c^2}{\epsilon_c} = \frac{q_c^2}{U_m^2}\frac{U_m^3}{\epsilon_c b}\frac{ab}{U_m}, \qquad (4.3)$$

and is therefore a combination of results already presented in figures 14(*b*), 15(*b*) and figure 4.
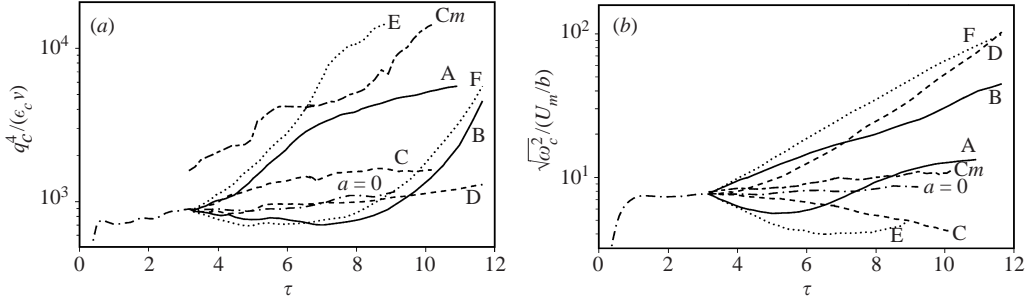
FIGURE 17. Time evolution of (*a*) turbulence Reynolds number $q_c^4/(\epsilon_c v)$ and (*b*) relative strength of vortical fluctuations $\sqrt{\omega_c^2}/(U_m/b)$ at the wake centreline. ——, Cases A (upper curve in (*a*) and lower curve in (*b*)) and B (other solid curve); ————, cases C (upper curve in (*a*) and lower curve in (*b*)) and D (other dashed curve); ······, cases E (upper curve in (*a*) and lower curve in (*b*)) and F (other dotted curve); and —·—, unstrained wake. Also shown for case C are the same quantities calculated with q_m^2, ϵ_q, and ω_m^2 instead of q_c^2, ϵ_c, and ω_c^2 (—·—). Note the higher initial value of the curve involving q_m^2.

For an unstrained wake the turbulence time scale quickly comes into equilibrium with the wake shear (figure 16*b*). The ratio $(q_c^2/\epsilon_c)/(b/U_m)$ reaches a constant value of about 3.9 (note that this corresponds to $(\partial \overline{U}/\partial y)_{max}(q_c^2/\epsilon_c) = 5.6$ for a Gaussian mean profile). This is not the case for the strained wake flows, which, at least initially, exhibit roughly exponential evolution of $(q_c^2/\epsilon_c)/(b/U_m)$. During this initial exponential period, the curves are paired symmetrically around the unstrained case. Changing the sign of the global strain changes the sign of the exponential growth rate. For $\tau - \tau_1$ of less than about 2, the exponential growth rates n, defined analogously to those given in equation (4.1), are about ± 1.5 for cases E and F, ± 1.0 for cases A and B, and ± 0.5 for cases C and D. At late times, cases A, B, E and F are perhaps coming into equilibrium, with $(q_c^2/\epsilon_c)/(b/U_m)$ becoming roughly constant. The expected further rapid increase of $\overline{w'^2}$ in cases B and F, however, will presumably result in the ultimate increase of this ratio at later times. Cases C and D maintain exponential growth throughout their evolution, although for case D the exponential decay rate n becomes about 2.5 times larger than its initial value when $\tau - \tau_1$ exceeds about 2.5. Thus, unlike for the other flows in which $(q_c^2/\epsilon_c)/(b/U_m)$ ultimately increases or approaches a constant, for case D the wake shear is decaying faster than the turbulent time scale is increasing.

The turbulence Reynolds number $q_c^4/(\epsilon_c v)$ is shown in figure 17(*a*). It increases for all the cases, despite the decreasing wake Reynolds number Re_m for cases A, D and F (see figure 1). Turbulence is thus sustained for all orientations of the applied strain. From this plot it is also clear why the computational cost to continue cases E and C to larger total strains is prohibitive (see §3.3).

In an unstrained wake, the r.m.s. vorticity fluctuation level is in balance with the wake shear rate and $\sqrt{\omega^2}b/U_m$ becomes constant. For all the free shear flows examined here, $\epsilon = v\omega^2$ to within a few percent (a result of relatively weak inhomogeneity) and

$$\sqrt{\overline{\omega^2}}\,\frac{b}{U_m} \approx \sqrt{\frac{\epsilon b}{U_m^3}}\sqrt{\frac{bU_m}{v}}. \tag{4.4}$$

Thus, according to classical similarity theory, the ratio $\sqrt{\omega^2}b/U_m$ should evolve as $Re_m^{1/2}$. The observed evolution of $\sqrt{\omega_c^2}b/U_m$ is shown in figure 17(*b*). As expected
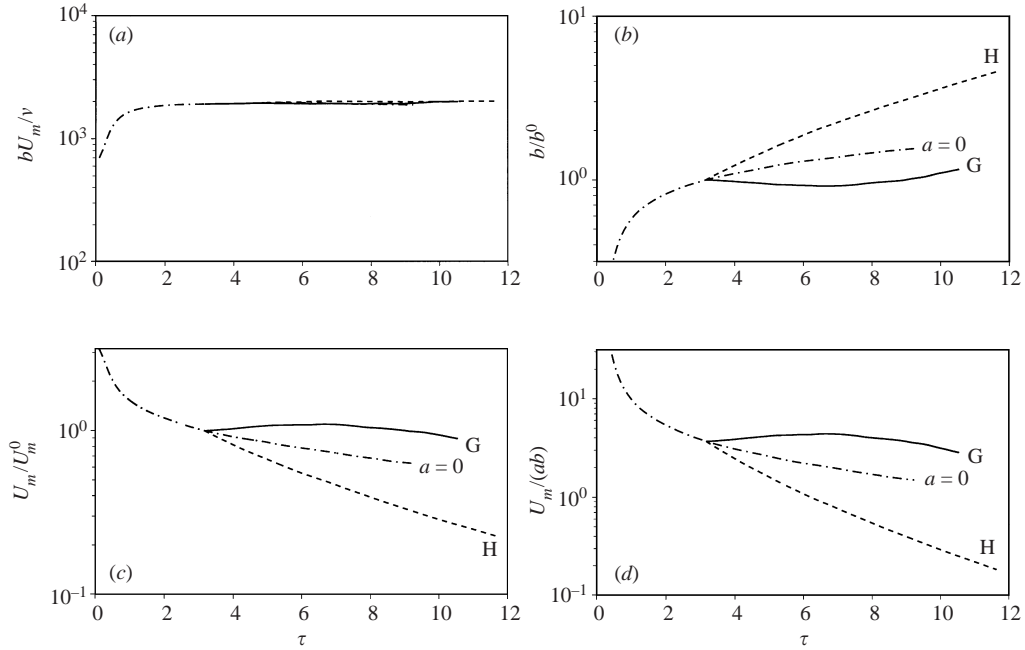
FIGURE 18. Evolution of the (*a*) Reynolds number $Re_m = bU_m/\nu$, (*b*) wake width *b*, (*c*) peak velocity deficit U_m, (*d*) ratio of wake shear rate to applied strain rate $U_m/(ab)$ for the axisymmetric cases: ———, case G; – – – –, case H; and — · —, unstrained wake (with same value of *a*).

from the previous discussion, none of the flows is evolving in accordance with the classical self-similar prediction, except possibly case E at late times. For all cases, the strength of the vorticity fluctuations ultimately increases relative to the wake shear (considering ω_m^2 for case C rather than the decaying centreline value ω_c^2). In contrast, this ratio would decay in cases A, D and F if the evolution followed the classical self-similar solution. Like q_c^2/ϵ_c and U_m/b, the initial response of $\sqrt{\omega_c^2}b/U_m$ to the strain is determined by a_{33}. Note that the relationship $\epsilon \approx \nu\omega^2$ can also be used to cast $\sqrt{\omega^2}(q^2/\epsilon)$, the other time scale ratio involving ω^2, as approximately $\sqrt{q^4/(\epsilon\nu)}$.

4.2. *Axisymmetric strain cases*

Examination of the classical self-similar solution (2.45) suggests the possibility of a self-similar evolution with both constant wake width and constant wake velocity deficit when $a_{22} - a_{11} = 0$ (*a* is taken here as $a = |a_{33}| = 2|a_{11}| = 2|a_{22}|$). In order to verify whether this solution describes the actual flow evolution, two cases with such axisymmetric strain, cases G and H ($a_{33} > 0$ and $a_{33} < 0$, respectively), were run. The evolutions of the wake width, velocity deficit, and the product and ratio of these quantities are shown in figure 18. The scaled wake mean velocity profiles for these two cases are similar to those shown in figure 6, i.e. they decay slightly faster than a Gaussian at the edges of the wake. This self-similarity of the mean velocity profiles results in constraint (2.35) holding for these flows (as it did for the plane strain cases) and the Reynolds number Re_m is constant, as seen in figure 18(*a*). According to the classical self-similar solution both *b* and U_m should also be constant. Although this is approximately the case for case G (especially given the limited sample of large-scale eddies at late times), it is not so for case H (figures 18*b* and 18*c*). In case H the wake
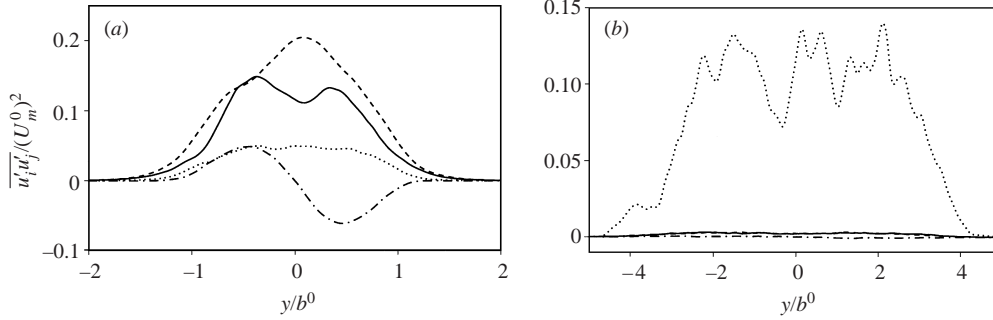
FIGURE 19. Reynolds stress profiles: ——, $\overline{u'^2}$; –––, $\overline{v'^2}$; ·····, $\overline{w'^2}$; and —·—, $\overline{u'v'}$ at the final time t_f of each simulation for (a) case G ($\tau - \tau_1 = 7.38$) and (b) case H ($\tau - \tau_1 = 8.49$).

shear rate decays and does not remain in balance with the constant applied strain rate.

There is no choice of applied strain for which the equilibrium similarity solution (2.54) predicts statistically stationary turbulence. For both the wake width and deficit to be constant, this solution would require both a_{22} and a_{11} to be zero, which is not possible for non-zero applied strain. On the other hand, the equilibrium similarity solution (2.55) does predict constant wake width, wake deficit and Reynolds stresses when $a_{11} = a_{22}$, $E_1 = -1$, $E_2 = \frac{1}{2}$ and $E_3 = -2$ (it reduces to the classical solution (2.45) in this instance). For other non-zero values of E_1 the solution (2.55) approaches statistical stationarity at long times if E_2 and E_3 have these values and the strain rates $a_{11} = a_{22}$ are negative (e.g. case G).

Although the roughly constant evolutions of b and U_m for case G are in agreement with both the classical self-similar solution (2.45) and the equilibrium similarity solution (2.55) (with $E_2 = \frac{1}{2}$ as expected for flows with $a_{22} < 0$), the Reynolds stresses increase in amplitude throughout most of the simulation and therefore do not exhibit statistical stationarity. The vertical velocity fluctuation intensity $\overline{v'^2}$ increases most rapidly and becomes the dominant Reynolds stress by the end of the simulation (see figure 19a). The other three non-zero Reynolds stresses do approach a constant magnitude beyond $\tau \approx 6$, suggesting that further evolution may possibly lead to statistical stationarity. Since the similarity solution (2.55) only approaches stationarity at long times, it is possible that this solution may be able to describe the observed Reynolds stress behaviour sooner than the classical self-similar solution (2.45). The equilibrium similarity solution (2.54) predicts exponentially decaying wake width, exponentially increasing wake deficit, and increasing Reynolds stresses for case G. These mean flow predictions are clearly inconsistent with the simulation results.

Case H is clearly not evolving in accordance with the classical self-similar solution. The wake width is increasing, the wake deficit is decreasing, and the Reynolds stresses are decreasing except for $\overline{w'^2}$, which ultimately increases rapidly after being roughly constant until $\tau \approx 5$. However, the width b and velocity deficit U_m are evolving exponentially, at least for times after $\tau \approx 6$. The exponential growth rates are about $C_\delta = a_{22}$ and $C_M = -a_{22}$, consistent with the predictions of both the similarity solutions (2.54) and (2.55). Both of these similarity solutions also predict the correct behaviour of all of the Reynolds stresses, the predicted exponential growth or decay rates of both solutions being the same at large times.

Thus, as with the plane strain cases examined in §4.1, when the cross-stream

direction is expanded, the flow width ultimately increases as if being simply stretched by the mean strain, not at the rate predicted by classical self-similar analysis. Case G is also in agreement with the plane strain results, in that compression of the cross-stream direction results in a (roughly) constant wake width. The apparent agreement with the classical self-similar solution for case G is then forced by constraint (2.35) and the chosen values of a_{11} and a_{22}.

The strain geometry of case G can be created by combining the strains of cases A and E (at half their amplitude) and indeed the relative amplitudes of the Reynolds stresses shown in figure 19(a) are intermediate between those for case A and case E, shown in figure 11. The strain geometry of case H can be generated by combining the strains of cases B and F and it is therefore not surprising that $\overline{w'^2}$ becomes dominant, as it does for those two flows that also have compressive spanwise strain (see figure 19b).

The quantities q_c^2/U_m^2, $\epsilon_c b/U_m^3$, aq_c^2/ϵ_c, $(q_c^2/\epsilon_c)/(b/U_m)$, $q_c^4/(\epsilon_c \nu)$ and $\sqrt{\omega_c^2}b/U_m$ (not shown) and $U_m/(ab)$ (figure 18d) are also generally intermediate between those of cases A and E for case G and intermediate between those of cases B and F for case H (the exceptions being the late-time behaviour of the three quantities involving both ϵ_c and q_c for case H, in which the ratios exceed those of both cases B and F). As noted before, aq_c^2/ϵ_c is generally insensitive to the orientation of the strain, with some variation depending on the sign of the spanwise strain. Up to $\tau - \tau_1 \approx 4.3$, the values for cases A, E and G (expansive spanwise strain) are very similar, as are those for cases B, F and H (compressive spanwise strain). The initial responses of $U_m/(ab)$ and $\sqrt{\omega_c^2}b/U_m$ to the strain are also determined by a_{33}. As with the plane strain cases, the initial behaviour (up to $\tau - \tau_1 \approx 3$ in these flows) of $(q_c^2/\epsilon_c)/(b/U_m)$ is approximated well by an exponential, where the sign of the growth rate depends on the sign of the applied strain.

4.3. *Other strain rates*

As noted previously, the strain rate a was chosen so that the time scale of the strain closely approximated the turbulence time scale at the wake centreline, q_c^2/ϵ_c. In order to assess the impact of the rate of straining, two additional cases were run with strain rates a factor of four smaller and larger than the baseline value. The geometry of case C was chosen for these additional runs because of its relevance to the aircraft industry. As listed in table 2, for the slowly strained case SC, $ab^0/U_m^0 = 0.068$, whereas for the more rapidly strained case FC, $ab^0/U_m^0 = 1.084$.

Combining these two simulations with case C and the results for the unstrained wake ($a = 0$) yields four simulations, identical at $\tau_1 = 3.16$, that evolve with the same strain geometry, but with the strain applied at different rates. The evolutions of various dimensionless mean flow quantities for these four flows are shown in figure 20. Increasing the strain rate a increases the rate at which the wake spreads, the rate at which the deficit increases, and the rate at which the Reynolds number Re_m increases. The equilibrium value of the wake shear rate also increases with a, although it remains lower than the value at τ_1.

The strained wake curves in figure 20 are evolving exponentially, as was seen for case C previously. In an effort to collapse the different evolutions, the same quantities have been plotted against $a(t - t_1)$, the logarithm of the total strain, in figure 21. Note that the results for the unstrained wake ($a = 0$) have been replaced by analytical exponential curves. Also, in figure 21(d) the wake shear has been non-dimensionalized by the strain rate a rather than by its initial value. As predicted by equation (2.32), the
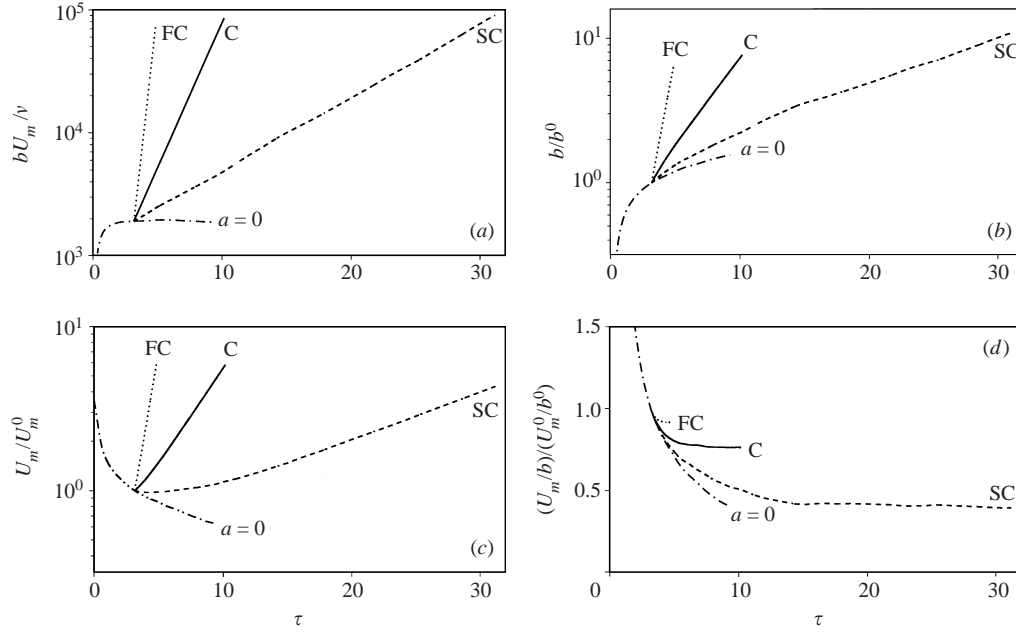
FIGURE 20. Evolution of the (a) Reynolds number $Re_m = bU_m/\nu$, (b) wake width b, (c) peak velocity deficit U_m, and (d) wake shear U_m/b for the cases with different strain rates: – – – –, case SC; ———, case C; $\cdots\cdots$, case FC; and — · —, unstrained wake.
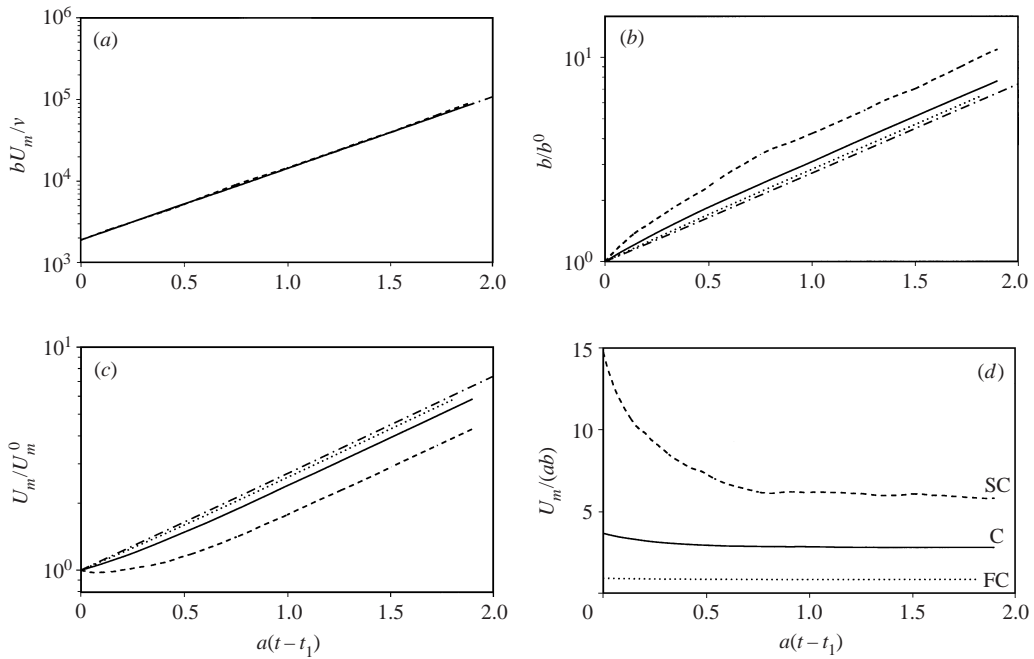
FIGURE 21. Evolution of the (a) Reynolds number $Re_m = bU_m/\nu$, (b) wake width b, (c) peak velocity deficit U_m, (d) ratio of wake shear rate to applied strain rate $U_m/(ab)$ for the cases with different strain rates versus $a(t - t_1)$: – – – –, case SC; ———, case C; $\cdots\cdots$, case FC; and — · —, $\exp(a(t - t_1))$ for (b) and (c), $(b^0 U_m^0/\nu)\exp(2a(t - t_1))$ for (a).
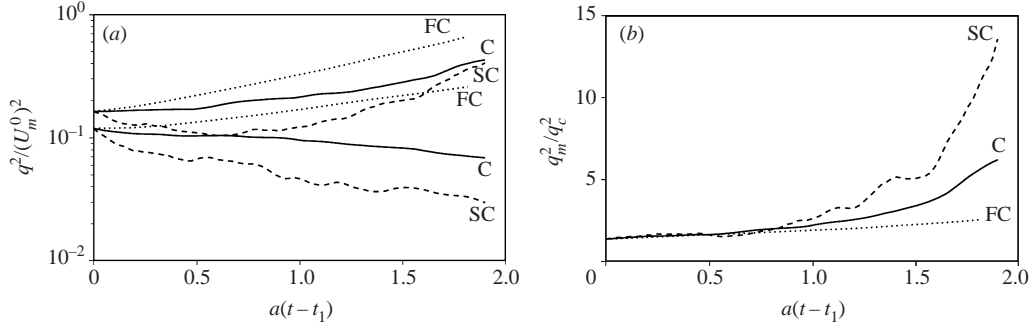
FIGURE 22. Evolution (*a*) of the maximum (upper curve) and centreline (lower curve) value of twice the turbulent kinetic energy and (*b*) the ratio q_m^2/q_c^2 for – – – –, case SC; ——, case C; and $\cdots\cdots$, case FC.

collapse of Re_m for the various cases is excellent. The slight deviations are a result of small differences in the shape of the scaled mean velocity profiles. Once the flows are developed, both the wake width and peak velocity deficit grow exponentially at the same rate as for case C in these coordinates, being proportional to e^{at}. As the strain rate increases, the time required to reach this asymptotic exponential growth rate becomes shorter. For case FC with the largest strain rate, the width and deficit begin growing exponentially almost immediately after the strain is applied. This suggests that this case is close to the rapid distortion limit in which the turbulence does not have time to respond to the straining and is simply distorted in accordance with the mean strain. As was noted in figure 20(*d*), the wake shear for these strained wakes approaches a constant, although this constant is a function of the strain rate *a*. The ratio of the strain time scale to the shear time scale in case FC is about 0.84. Apparently the rapid distortion limit noted above is reached when these time scales are of the same order.

As discussed in §4.1, for the strain geometry of case C the turbulence is more energetic away from the wake centreline. In order to investigate whether this trait is dependent on the strain rate, the evolutions of both q_m^2 and q_c^2 have been plotted in figure 22(*a*) for all three cases. Note that the centreline value q_c^2 decays for cases C and SC but increases for case FC. In contrast, q_m^2 ultimately increases for all three cases. For the rapidly strained case FC, the growth is close to exponential throughout the entire evolution, scaling approximately like $\exp(a(t-t_1)/2)$ for q_c^2 and $\exp(0.85a(t-t_1))$ for q_m^2. For the other two cases, the growth is less convincingly exponential and there is a delay before q_m^2 increases. The net result is that the ratio q_m^2/q_c^2 becomes much larger in the slowly strained flow than in rapidly strained flow (figure 22*b*). The corresponding value of this ratio during the self-similar period of the unstrained wake is about 1.4 (the initial level at $t = t_1$). Note that for all cases the ratio q_m^2/q_c^2 is fairly constant (and equal to the unstrained value) until about $a(t-t_1) \approx 0.8$, suggesting that the q^2 profiles are similar in shape until this time. The evolution of the enstrophy ratio ω_m^2/ω_c^2 (where the subscript *m* indicates the peak profile level) is similar to that of the kinetic energy ratio q_m^2/q_c^2 for all three strain rates.

Similar plots of q_m^2/q_c^2 can be made for the other strain geometries. This ratio approaches 1.0 for cases A, D, E and F because the profile maxima are at the centreline. It grows to close to 2.0 in case B for $a(t-t_1) > 1.0$ (ω_m^2/ω_c^2 is also about
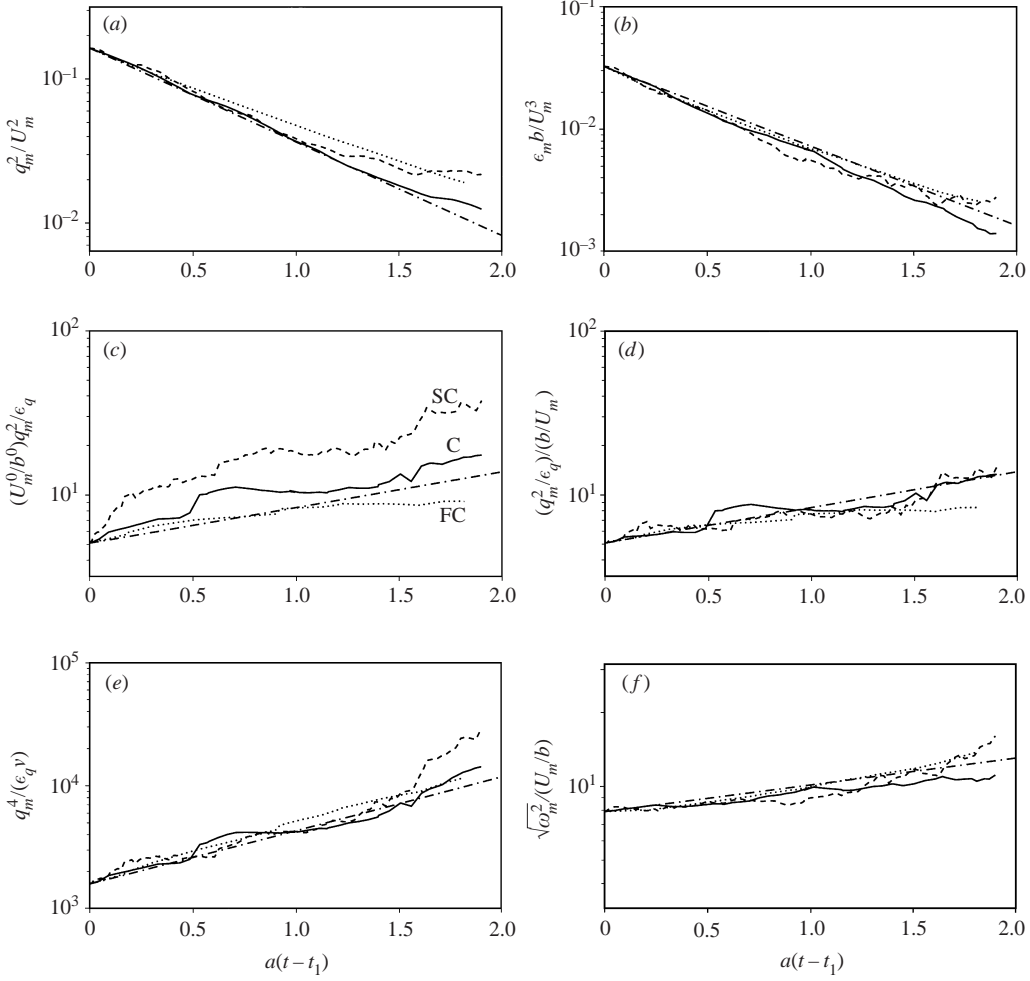
FIGURE 23. Evolution of the maximum values of dimensionless quantities: (a) q_m^2/U_m^2, (b) $\epsilon_m b/U_m^3$, (c) $(U_m^0/b^0)q_m^2/\epsilon_q$, (d) $(q_m^2/\epsilon_q)/(b/U_m)$, (e) $q_m^4/(\epsilon_q \nu)$, and (f) $\sqrt{\omega_m^2}/(U_m/b)$ for the cases with different strain rates versus $a(t - t_1)$. $----$, Case SC; $\rule{1.5em}{0.4pt}$, case C; $\cdots\cdots$, case FC; and $-\cdot-$, $(q_m^2/U_m^2)^0 \exp(-3a(t - t_1)/2)$ for (a), $(\epsilon_m b/U_m^3)^0 \exp(-3a(t - t_1)/2)$ for (b), $(U_m^0/b^0)(q_m^2/\epsilon_q)^0 \exp(a(t - t_1)/2)$ for (c) and (d), $(q_m^4/(\epsilon_q \nu))^0 \exp(a(t - t_1))$ for (e), and $(\sqrt{\omega_m^2})^0/(U_m^0/b^0) \exp(a(t - t_1)/4)$ for (f).

2.0 for this case). Thus, unlike in case C, the level of the turbulent kinetic energy at the centreline in case B remains in proportion to the peak level.

For the case-C-type strain geometry, the centreline values of the mean profiles of the various turbulence statistics are not representative of the overall profile levels beyond $a(t - t_1) \approx 0.8$, particularly for slow strain rates. Thus, for comparing the turbulence in these cases with varying strain rate, the quantities q_m^2, ϵ_q, ϵ_m and ω_m^2 will be used instead of the corresponding centreline values.

As noted in the discussion of case C previously, the growth rates observed for the mean flow quantities for this strain geometry are the same as those predicted by both equilibrium similarity solutions (2.54) and (2.55), as well as those predicted by the internally inconsistent classical self-similar solution (2.45). Variation of the strain rate has not changed the observed exponential growth behaviour of δ and U_m. The
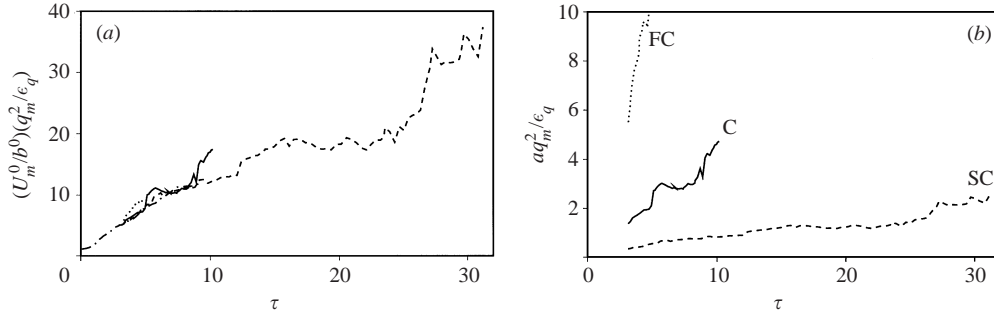
FIGURE 24. Evolution of the scaled turbulence time scale: (*a*) $(U_m^0/b^0)(q_m^2/\epsilon_q)$ and (*b*) aq_m^2/ϵ_q for the cases with different strain rates. ––––, Case SC; ——, case C; ·····, case FC; and —·—, unstrained wake.

classical self-similar analysis predicts that the Reynolds stresses (and therefore q^2) should scale like U_m^2 and that the ratio q^2/U_m^2 should be constant. As can be seen in figure 23(*a*), this is not the case for any strain rate (the ratio at the location of maximum q^2 is shown in the figure, but the ratio at the wake centreline yields the same result). The turbulent kinetic energy cannot keep pace with the exponentially increasing velocity deficit and the ratio q_m^2/U_m^2 decays roughly like $\exp(-3a(t-t_1)/2)$ (somewhat slower for case FC). Turbulent kinetic energy is produced by both the mean strain and the wake shear, but at a rate that cannot keep pace with the rapidly increasing deficit. Similarly, the dissipation rate ϵ_m grows less rapidly than U_m^3/b (figure 23*b*). The equilibrium predicted by the classical self-similar analysis cannot be achieved in the presence of exponentially growing mean flow width and velocity deficit. As with case C, the behaviour of $\overline{v'^2}$ and $\overline{w'^2}$ is better described by the equilibrium similarity solution (2.54) than by (2.55).

The evolution of the turbulence time scale q_m^2/ϵ_q (and also q_c^2/ϵ_c) does not collapse when plotted against $a(t-t_1)$, as can be seen in figure 23(*c*). In fact the curves collapse better when plotted simply against the time τ as is done in figure 24(*a*), which also includes the time scale evolution for the unstrained wake flow (there is even less scatter for the q_c^2/ϵ_c curves). This is remarkable, indicating that the turbulence time scale evolution is mostly independent of the strain rate as well as the strain geometry (see §§4.1 and 4.2) and suggests that its evolution is reasonably well predicted by that in an unstrained wake. Because the time scale evolution is nearly independent of the strain rate, the dimensionless ratio aq_m^2/ϵ_q differs roughly by a constant multiple for the different cases, as shown in figure 24(*b*). Although the straining has a pronounced effect on the mean flow evolution it is less strongly coupled to the turbulence.

The collapse of the time scale ratio $(q_m^2/\epsilon_q)/(b/U_m)$ when plotted against $a(t-t_1)$ is good, however (figure 23*d*). As with q_m^2/U_m^2, the value for the rapidly strained case FC changes more slowly than those for the other two cases. The evolutions of the dissipation $\epsilon_m b/U_m^3$, turbulence Reynolds number $q_m^4/(\epsilon_q \nu)$, and time scale ratio $\sqrt{\omega_m^2}b/U_m$ all are fairly independent of the strain rate when plotted against $a(t-t_1)$. Note that the evolutions of these quantities for the various cases are very different when plotted against τ, unlike the time scale q_m^2/ϵ_q examined above. Again, using the centreline values q_c^2 and ϵ_c does not change these conclusions.

Examination of figures 21 and 23 suggests that many characteristics of the strained wakes are similar when compared at the same value of total strain $\exp(a(t-t_1))$. In figures 25 and 26 profiles of the mean wake velocity deficit and Reynolds stresses
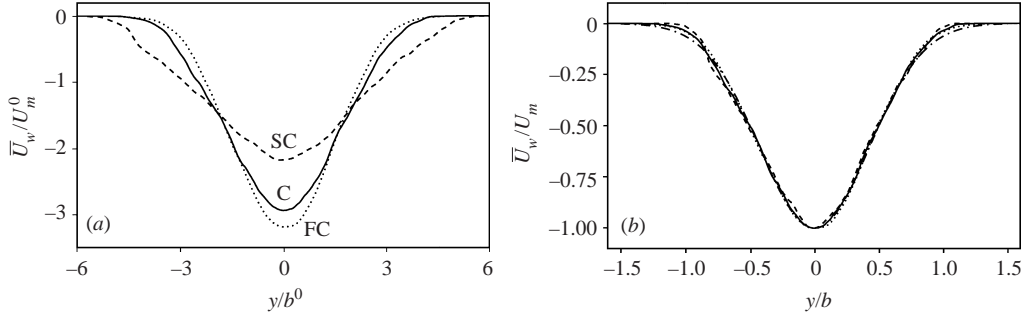
FIGURE 25. Unscaled (*a*) and scaled (*b*) wake mean velocity profiles at $a(t - t_1) = 1.2$ for the cases with different strain rates. – – – –, Case SC; ——, case C; $\cdots\cdots$, case FC; and — $\cdot$ —, Gaussian $-\exp(-(4\ln 2)(y/b)^2)$.
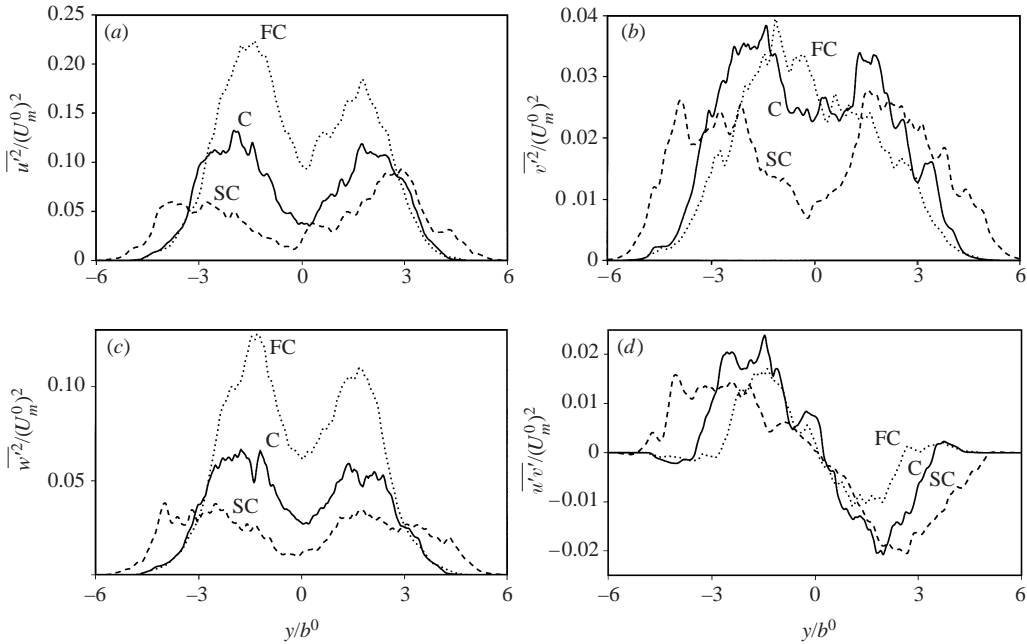

FIGURE 26. Reynolds stress profiles: (*a*) $\overline{u'^2}$, (*b*) $\overline{v'^2}$, (*c*) $\overline{w'^2}$, and (*d*) $\overline{u'v'}$ at $a(t - t_1) = 1.2$ for the cases with different strain rates. – – – –, Case SC; ——, case C; and $\cdots\cdots$, case FC.

are plotted at $a(t - t_1) = 1.2$, corresponding to a total strain of 3.3. This value (about half the total strain reached by the end of the simulations) was chosen to ensure that the flows were developed (in the asymptotic exponential growth periods for the wake width and velocity deficit) but still had adequate statistical sample (*x*-domain extent) to ensure reasonable mean profiles.

Consistent with the results presented in figures 21(*b*) and 21(*c*), the mean profiles plotted in figure 25(*a*) decrease in width and increase in peak deficit level as the strain rate is increased. The change from the baseline case C to the rapidly strained case FC is small, again suggesting that case FC is close to the rapid distortion limit. Scaling the mean wake velocity profiles by the peak deficit and width results in good collapse, again indicating that the shape of the mean profile is nearly universal (figure 25*b*). As noted previously, wake mean velocity profiles (both strained and unstrained) decay

slightly more rapidly to zero at the edges of the wake than is the case with a Gaussian profile. From figure 25(*b*) it is apparent that this effect possibly becomes slightly more pronounced as the strain rate decreases.

Examination of the Reynolds stress profiles in figure 26 again indicates that for a fixed value of total strain the wake narrows with increasing strain rate. Although the decrease in width between the baseline case C and the rapidly strained case FC is minimal, the increase in the level of both $\overline{u'^2}$ and $\overline{w'^2}$ between these two cases is large, with the peak levels of these profiles roughly doubling with each quadrupling of the strain rate. In contrast, the stress $\overline{v'^2}$ changes little between cases C and FC and the Reynolds shear stress $\overline{u'v'}$ decreases. This implies a substantial decrease in the shear correlation coefficient $\overline{u'v'}/\sqrt{\overline{u'^2}\,\overline{v'^2}}$, consistent with the Reynolds stress production being dominated by the mean strain rather than the wake shear (see figure 32 in Appendix D). The collapse of the various profiles in figure 26 is improved (particularly for the $\overline{u'^2}$ and $\overline{w'^2}$ profiles of cases SC and C) if the curves are scaled by U_m and b, suggesting that part of the differences in the Reynolds stress profiles are associated with the changes in these mean quantities with strain rate. The $\overline{v'^2}$ profile for case FC is not double-peaked and therefore cannot be scaled to match the profiles of the other two cases.

The growth of the $\overline{v'^2}$ and $\overline{w'^2}$ profiles in time for case SC is less pronounced than that for cases C and FC. This is more in line with the long-time behaviour of equation (2.55), which predicts the ultimate decay of $\overline{v'^2}$ and the approach of $\overline{w'^2}$ to a constant when $E_2 = \frac{1}{2}$ and $E_3 = 1$, rather than continued increase of these Reynolds stresses. Of course E_2 need not be $\frac{1}{2}$ when $a_{22} > 0$ and the Reynolds stress profiles for case-C-type straining are not yet completely self-similar anyway (see figure 22*b*), so this may be coincidental rather than the result of better equilibrium associated with slower straining.

4.4. *Flow visualization*

The structure of the turbulence in strained wakes depends strongly on the orientation of the strain relative to the wake. In this section, contours of spanwise vorticity are used to visualize the flow structure at the time $a(t - t_1) \approx 1.2$, corresponding to a total strain of about 3.3. This time was chosen, as in §4.3, to allow for significant straining without excessive loss of computational domain size. Instantaneous slices through the full computational domain at $z = 0$ for each of the ten strained wakes listed in table 2 are shown in fixed laboratory coordinates (not the moving computational coordinate system) in figures 27, 28 and 29. The strained wakes are grouped into the three figures according to the sign of their spanwise strain component. A visualization of the initial field used for all the computations is also included in figure 27(*a*). Other flow visualizations of the unforced wake simulation used to generate the initial conditions for the strained wake computations can be found in Moser *et al.* (1998).

The cases with expansive spanwise strain are shown in figure 27. The frames in the figure are drawn to scale (the distance between the tick marks being b^0) and each frame has the same contour levels (this is also true of the following two figures 28 and 29). For these cases, the spanwise domain size increases in time. For case A with $a_{11} = 0$, the statistical sample of eddies in the computational domain increases, while for case E, in which $a_{11} < 0$, the evolution is quickly constrained by the limited streamwise domain. The streamwise domain is also reduced in case G, although at only half the rate at which the spanwise domain extent is increased.
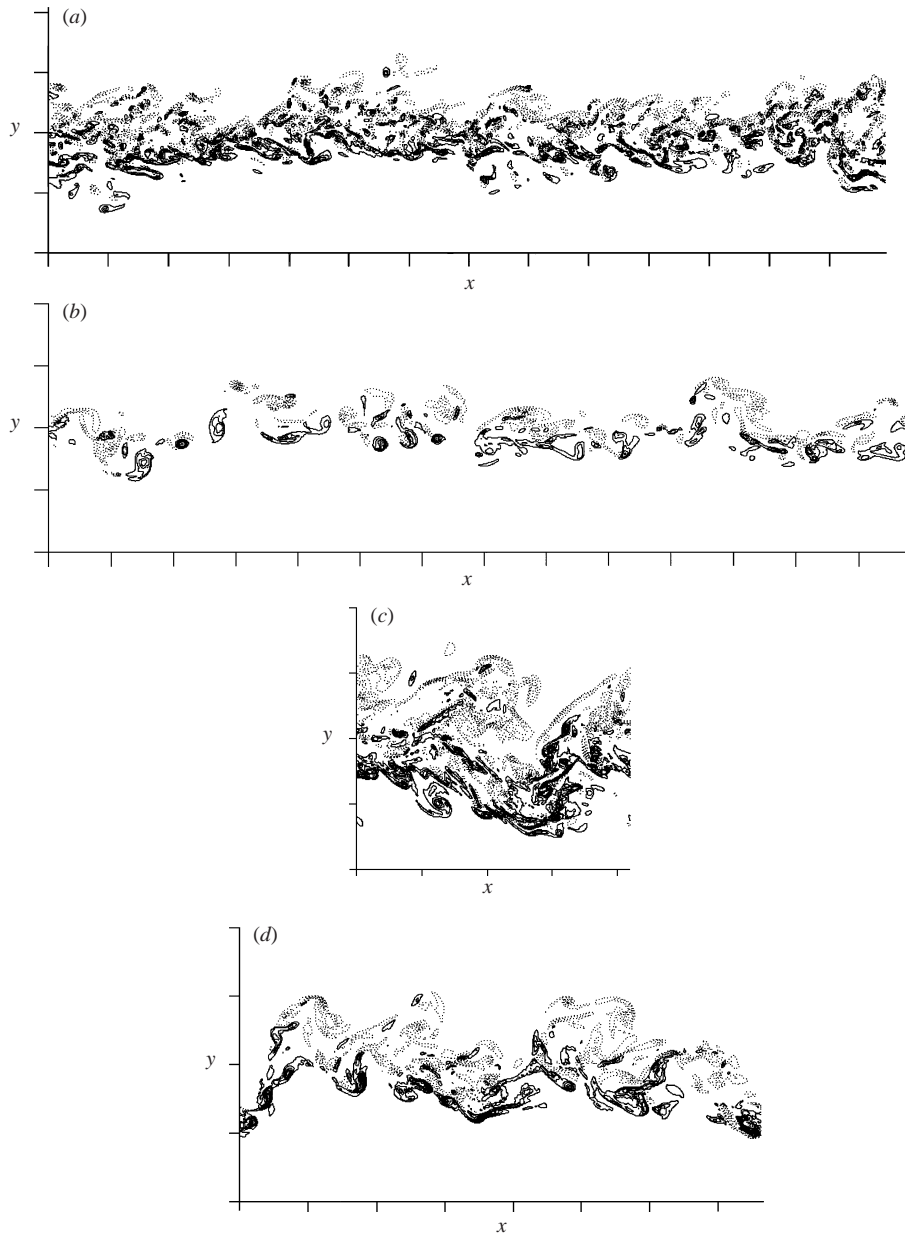
FIGURE 27. Contours of spanwise vorticity in the $z = 0$ plane at (a) $t = t_1$ for the unstrained wake, (b) $a(t - t_1) = 1.20$ for case A, (c) $a(t - t_1) = 1.20$ for case E, and (d) $a(t - t_1) = 1.20$ for case G. Negative contours are dotted, positive contours are solid, and the contour increment is $3.0U_m^0/b^0$. Tick marks are at b^0 intervals. Note that the strained wakes shown here all have expansive spanwise strain.

In case A (figure 27b) the wake width has reached a roughly constant value by the time shown, following a small initial decrease in width relative to the initial condition (figure 27a). The structure has become comparatively more organized, with fewer vortical eddies across the width of the layer and regions of apparently non-vortical fluid crossing the layer at several locations. As time progresses, the stretched vortical structures tend to amalgamate with other vortical regions of the same sign, further
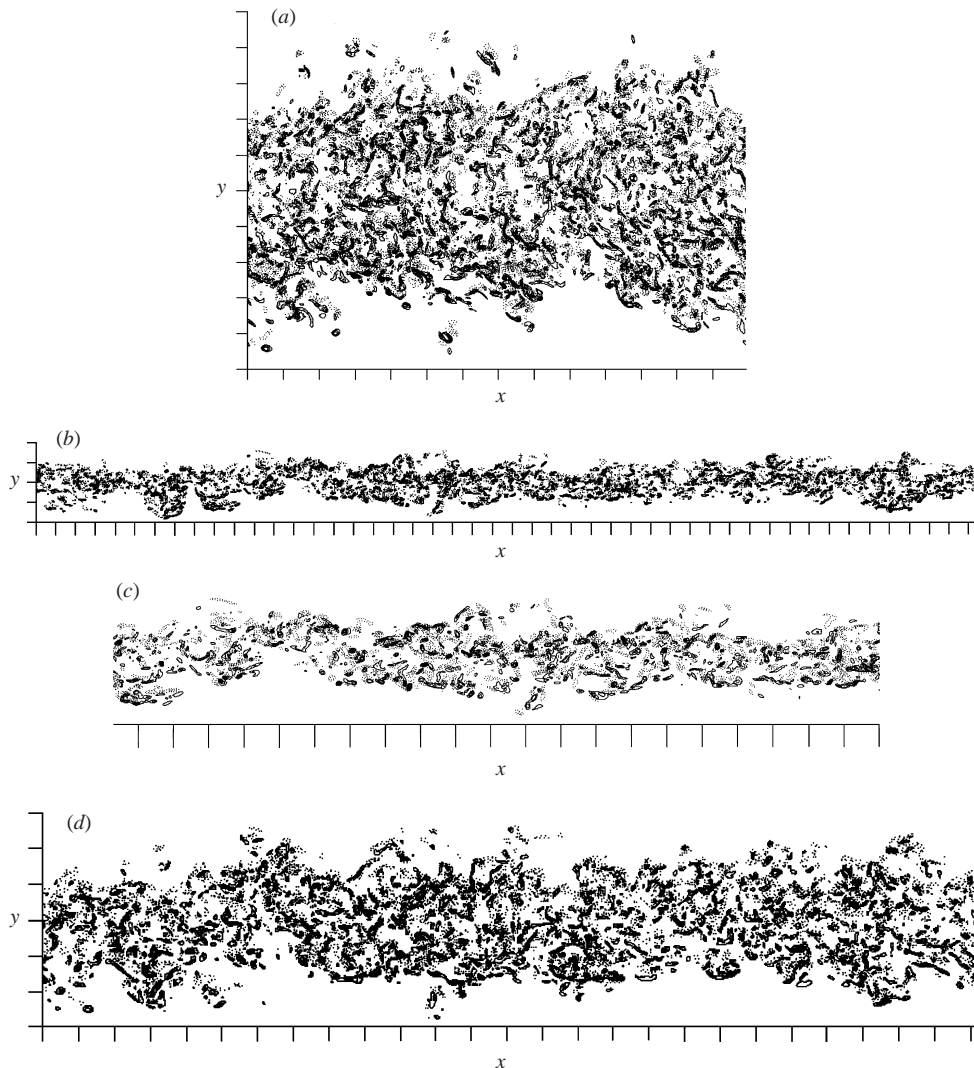
FIGURE 28. Contours of spanwise vorticity in the $z = 0$ plane at (*a*) $a(t - t_1) = 1.24$ for case B, (*b*) $a(t - t_1) = 1.22$ for case F, (*c*) enlargement of a central portion of (*b*) to achieve same scale as in (*a*) and (*d*), and (*d*) $a(t - t_1) = 1.26$ for case H. Negative contours are dotted, positive contours are solid, and the contour increment is $1.5U_m^0/b^0$. Tick marks are at b^0 intervals. Note that all cases shown here have compressive spanwise strain.

increasing the organization of the flow. This 'collapse' of strained vorticity is similar to that observed in the model problem described by Lin & Corcos (1984). Indeed, some of the vortical eddies (such as those at $x \approx 1.5b^0$ and $x \approx 2.8b^0$) are similar in cross-section to the 'collapsing' rib vortices in the strained 'braid' region of a mixing layer, which was the flow Lin & Corcos were seeking to model. Despite the exponentially decaying value of Re_m and the increasing organization of the vorticity, however, the turbulence Reynolds number $q^4/(\epsilon v)$ increases, and it is unlikely that this flow will relaminarize.

Case E (figure 27*c*) is compressed in the streamwise direction. The spanwise vorticity fluctuations intensify and the large-scale organization suggests one oscillation of a
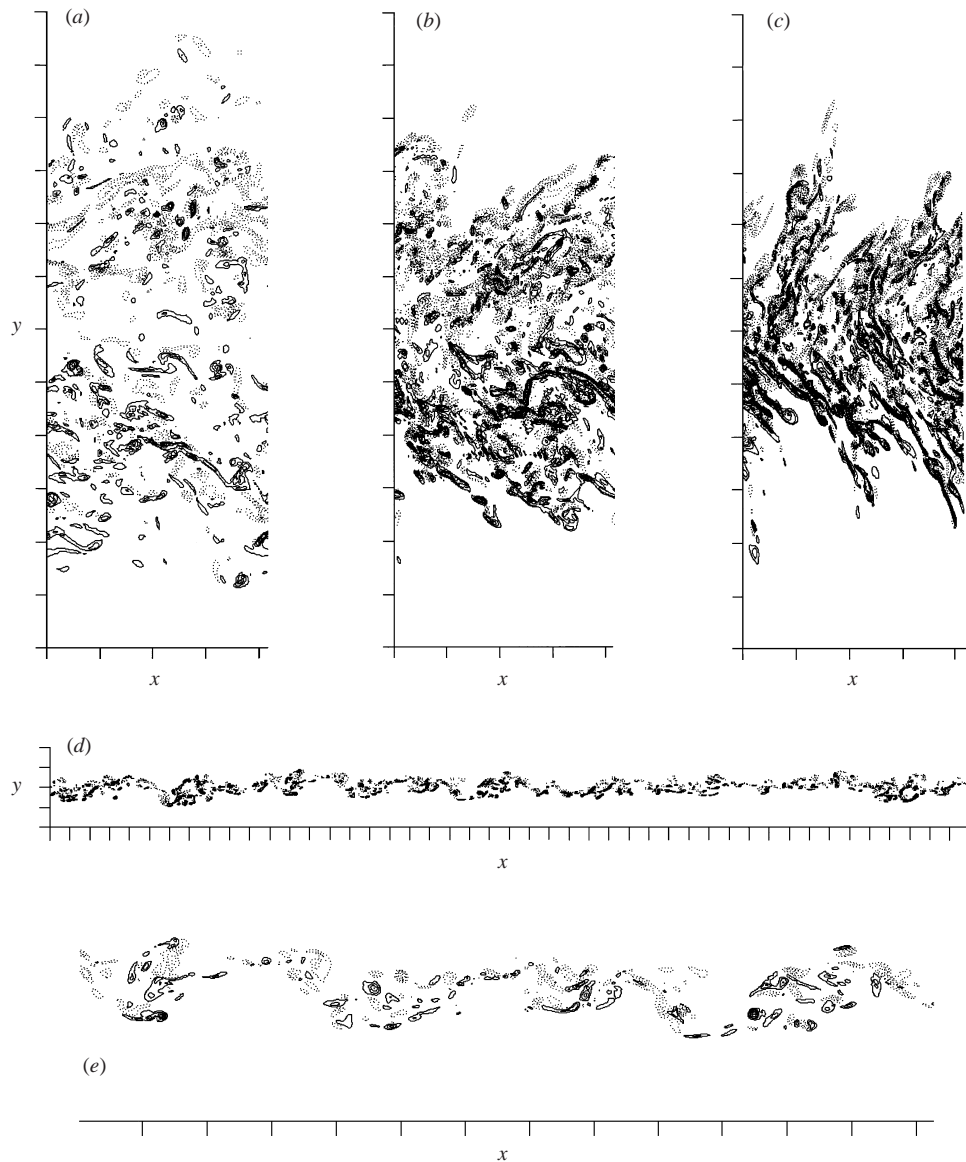
FIGURE 29. Contours of spanwise vorticity in the $z = 0$ plane at (a) $a(t - t_1) = 1.21$ for case SC, (b) $a(t - t_1) = 1.21$ for case C, (c) $a(t - t_1) = 1.20$ for case FC, (d) $a(t - t_1) = 1.20$ for case D, (e) enlargement of a central portion of (d) to achieve same scale as in (a), (b) and (c). Negative contours are dotted, positive contours are solid, and the contour increment is $2.0U_m^0/b^0$. Tick marks are at b^0 intervals. Note that all cases shown here have no spanwise strain.

Kármán vortex street. Relative to the increasing wake shear, the strain becomes less and less significant and some features of this flow resemble those of an unstrained wake. As noted previously, this case is probably constrained by the streamwise domain size after the time shown. Case G (figure 27d) is compressed equally in both the streamwise and cross-stream directions and is intermediate between the above two cases.

The cases with compressive spanwise strain (cases B, F and H) are shown in figure 28. At late times these flows are dominated by spanwise velocity fluctuations,

which do not directly contribute to the spanwise vorticity visualized (note that the contour interval in figure 28 is half that used in figure 27). For these cases, the spanwise domain size decreases in time; the flows ultimately are forced to be nearly two-dimensional because no large-scale spanwise variations can develop. These three cases exhibit many small-scale vortical eddies with little overall large-scale coherence or organization; this is especially true for cases B and H, which are stretched in the cross-stream direction.

Cases SC, C, FC and D, all without spanwise strain, are shown in figure 29. In case D, the computational domain size continually increases and the statistical sample of eddies improves in time. The wake has reached a nearly constant width roughly equal to that of case A, the other flow with cross-stream compression. Without spanwise stretching, however, the vortical eddies apparently do not amalgamate as in case A, instead becoming stretched in the streamwise direction as a result of the strain. To an even greater extent than in case A, there are large non-vortical regions penetrating the layer at later times.

The cases with the strain geometry of case C show marked variation in flow structure as a result of the varying strain rate, even when compared at the same value of total strain. As noted in § 3.3, the combination of vertical stretching and streamwise compression reduces the computational domain to a point where the streamwise eddy extent is prohibited from keeping pace with the flow width; the simulation may not represent the infinite-domain problem well for long times. However, these cases are dominated by many small-scale structures and this limitation may not be as severe as might be expected. As with cases B and H, which are also stretched in the cross-stream direction, large-scale organized motions (with their associated longer time scales) are apparently not able to develop or sustain themselves in the presence of this strain. Examination of the flow visualization suggests, as was found in § 4.3, that the straining in case FC is approaching the rapid 'box distortion' limit, with the small-scale vortical structures exhibiting coherence along steep inclination angles of about 60° to 70°. Readily apparent in figure 29(a) is the greater wake width and weaker spanwise vorticity for the slowly strained case SC.

4.5. *Comparison with experiments*

Experiments designed to subject wakes to uniform and constant strain rates can be compared directly to the numerical results. The experiments of Reynolds (1962) and Keffer (1965) are the spatially developing analogues of case A, whereas the tunnel orientation used in Keffer (1967) results in a strain field that corresponds to that of case B. The results of Elliott & Townsend (1981) can also be compared to case B, although streamwise mean velocity fluctuations of up to 20% in these experiments resulted in non-negligible values of a_{11}. Liu *et al.* (1999) subjected a plane wake to uniform and constant pressure gradients (both adverse and favourable). While this does not correspond to constant strain rate (see Appendix A), their tunnel wall profiles are not too different from those required to generate the spatially evolving analogues of cases C and D. No experimental data are available for comparison to cases E, F, G and H, although, as noted in § 3.3, a 'longitudinally distorting tunnel' that generated a strain geometry analogous to case F has been used to study strained homogeneous turbulence by Tucker & Reynolds (1968). Note that the total strain achieved in all these experiments is less than that attained in the simulations, although many of the late-time simulation results may be of questionable physical relevance because of computational domain size limitations.

It is difficult to set up an experiment that is a good approximation to the idealized strained wake. The streamwise flow development must be slow enough to ensure that streamwise inhomogeneity does not become significant. Also, the sudden change in tunnel cross-section causes flow separation near the entrance and exit of the distorting duct and this causes local acceleration of the streamwise free-stream velocity, resulting in an 'effective strain' that is not the same as that of the idealized problem. Reynolds (1962) proposed a linear 'graded imposition' of the strain rate over an interval equal to half the distorting duct length centred at the duct inlet. This 'graded imposition' was then used to make predictions of the wake width for comparison to the experimental results. It is unlikely that this could adequately account for the effects of the separation and the later studies listed above did not utilize such corrections.

Results reported by Reynolds (1962) include mean velocity profiles for the largest ($\frac{1}{2}$ in.) diameter cylinder (including the associated values of the half-width and deficit) and $\overline{u'^2}$ profile shapes for all three cylinders. Because of difficulties in measuring the mean velocity profiles for the two smaller cylinders, wake widths for these two cases were estimated from the width of the $\overline{u'^2}$ profiles. The velocity deficits are thus unavailable for these two cases. The wake widths from these two smaller cylinders, as estimated from the $\overline{u'^2}$ profiles, appear to decrease at the rate predicted by the classical self-similar analysis over a limited central portion of the distorting duct. The corresponding evolution of the wake velocity deficit cannot be confirmed as it was not measured for these cases. The wake width of the largest cylinder was found to decrease more slowly ($n_b \approx -0.2$) than the self-similar rate ($n_b = -0.5$). Consistent with this, the velocity deficit decays more rapidly than required for self-similarity. Reynolds (1962) ascribed this lack of similarity to the structure of this wake as it entered the straining duct relatively fewer diameters downstream from the cylinder. He also argued that self-similarity would only be observed for cases in which the production of turbulence associated with the wake shear was larger than that associated with the global strain. However, the experimental values of n_b and n_U for this cylinder are in line with the initial response to the distortion observed in case A, which is also not evolving as predicted by the classical self-similar analysis.

Despite the mean compression in the cross-stream direction, Reynolds (1962) measured rapidly growing wake widths near the inlet of the distorting section, with the spreading rate even outpacing that associated with an unstrained wake. Although several possible explanations for this are offered, it seems unphysical and disagrees with the numerical results presented in figure 2 and with the favourable pressure gradient cases of Liu *et al.* (1999), which also have $a_{22} < 0$. The use of a 'graded imposition' of the strain also cannot account for this. The separation at the distorting duct inlet results in a local increase and decrease of the mean convection velocity, and it is likely that the rapid wake spreading at this location is associated with this streamwise straining.

Reynolds (1962) found that the mean velocity profile shape was not significantly affected by the strain, as observed in the simulations. In particular, it was still close to Gaussian, decaying more rapidly at the edges of the wake. Despite this similarity of the mean profile shape, the Reynolds number Re_m does not decay at the appropriate exponential rate, indicating difficulties with the measurements (the values in the last column of table 1 in Reynolds (1962) should be constant). Although the shape of the $\overline{u'^2}$ profiles is roughly the same throughout the distorting duct, no magnitudes are given to assess whether $\overline{u'^2}/U_m^2$ is constant as expected for self-similarity.

Whether or not the strained wakes of Reynolds (1962) were actually evolving self-similarly was thus unclear, but further work in the same flow by Keffer (1965) indicated that self-similar evolution is not observed. Using the same cylinders placed at the same location upstream of the same distorting duct, Keffer observed $n_b = -0.35$ for the two smaller diameter cylinders and a value even closer to zero for the $\frac{1}{2}$ in. diameter cylinder. By the end of the distorting duct all three wake widths are approaching a constant, as observed in the simulations. When the smallest cylinder was moved closer to the distorting duct inlet values of $n_b = -0.162$ and $n_b = 0$ were obtained.

Keffer (1965) also made measurements of all non-zero components of the Reynolds stress tensor. The measured magnitudes of the normal Reynolds stresses are ordered as $\overline{v'^2} > \overline{u'^2} > \overline{w'^2}$, consistent with the results of the DNS presented in figure 11(a) for case A. However, the experimentally measured turbulent kinetic energy decreases monotonically (although not as rapidly as in an unstrained wake), in contrast to the numerical results, in which q^2 increases between $\tau = 4.4$ and $\tau = 7.3$ (figure 14a). This intermediate period of growth is attributable to $\overline{v'^2}$, which grows (doubling in magnitude) until becoming constant at about $\tau = 8.0$. The experimental value of $\overline{v'^2}$ decays monotonically (although slowly), presumably indicating that the strain in the experiments is relatively weaker than that in the computations.

Flow visualizations in the same study (Keffer 1965) 'indicate a predominantly strong motion of the large eddies' with 'a well-defined periodicity', and that 'the size and intensity of the motion become more pronounced as the total strain increases'. For large enough total strain 'gaps appear in the turbulent structure of the wake'. Measured energy spectra also indicate relatively more energetic large-scale motions and less small-scale activity. The increased large-scale organization observed in this flow is also in agreement with the DNS results presented in §4.4 (figure 27b).

In later experiments, Keffer (1967) reversed the sign of the applied strain (case B) by rotating the wake-generating cylinder 90° about the direction of the mean flow. Once again, the flow was found not to follow the self-similar evolution, with its evolution being better predicted by a 'box distortion model', at least for cases in which the wake had undergone a period of development before the strain was imposed. According to this 'box distortion model', the wake width follows the mean streamline distortion. This corresponds to $n_b = 1.0$ and is in agreement with the results of the DNS. Keffer noted a 'flattening' of the mean velocity profile for large total strains that differs from the universal velocity profile shape observed in the simulations. It seems likely that the measurements may have been affected by the proximity of the end of the distorting duct at this point.

The same strain geometry (expanding the wake in the cross-stream direction) was examined by Elliott & Townsend (1981). The distance between the sidewalls of their distorting tunnel changed by a factor of four throughout its length, similar to the duct used in Keffer (1967). However, flow separation at the duct inlet and exit was significant and the cross-sectional area was not constant, resulting in streamwise strain (although the total strain throughout the full length of the distorting section was small). Because of this, the strain rate in the Elliott & Townsend experiment is not constant and must be determined by experimental measurement. The results suggest that the strain is roughly constant for at least the central half of the distorting section and, given the small total strain over the full length of this section, this experiment is probably a reasonable approximation to the constant-strain-rate case B, at least away from the inlet and exit of the distorting section.

Unlike Keffer (1967), Elliott & Townsend (1981) do find the mean velocity deficit profiles to be self-similar, even for large total strain. These profiles are nearly Gaussian, but with a more rapid decay at the edges of the wake as observed in both the simulations and in unstrained wakes. Their strained wake spreads even more rapidly than the streamlines associated with their measured strain (and even faster than the rate of spreading of the tunnel walls). For case B the wake width initially increases more rapidly than the associated total strain, but for $a_{22}(t-t_1) > 1.0$ the two grow at the same rate, i.e. $n_b = 1$. At this point the experiment is already being affected by the downstream end of the distorting duct. After a slight decrease, the magnitude of the wake velocity deficit stays roughly constant in the experiment, as it does in the DNS. The behaviour of the Reynolds stresses in the experiments and computations is also similar. In both, the turbulent kinetic energy initially decays, but then becomes about constant before increasing. The cross-stream fluctuation intensity $\overline{v'^2}$ profiles become double-peaked and the spanwise fluctuation intensities $\overline{w'^2}$ increase significantly for large total strain. In the experiments, the turbulence length scales become relatively small compared to the flow width and eddies lose energy, with entrainment falling sharply. This is consistent with the flow visualization of case B in §4.4 (figure 28a).

Although not directly comparable to the constant-strain-rate cases considered here, the constant-pressure-gradient flows of Liu *et al.* (1999) have much in common with the simulation results. Liu *et al.* considered both adverse and favourable streamwise pressure gradients, corresponding roughly to cases C and D, respectively. Consistent with the previous experimental work and the present simulations, Liu *et al.* (1999) found that adverse pressure gradients resulted in larger wake deficits and wider wakes compared to the zero-pressure-gradient flow. Conversely, both the velocity deficit and wake width decayed more rapidly in the presence of favourable pressure gradients. The wake width in the mild favourable pressure gradient case approaches a constant near the end of the distorting tunnel section; that in the stronger favourable pressure gradient case is close to constant throughout the entire distorting section. The wake width in the adverse pressure gradient case grows rapidly, although not necessarily exponentially. The impact of the pressure gradient on the amplitude of $\overline{u'^2}$ is also similar to that of the strain in simulations, with favourable pressure gradients resulting in decreased fluctuation intensity levels compared to the zero-pressure-gradient case and vice versa for the adverse pressure gradient flow.

5. Conclusions

Ten direct numerical simulations of time-evolving turbulent plane wakes subjected to various constant and irrotational strains, both plane and axisymmetric, have been generated and analysed. The evolutions of the wake mean velocity, the Reynolds stresses, and various other turbulence statistics have been examined in detail and compared to the predictions of different similarity solutions. Additionally, flow visu-alizations of the numerical results have been used to investigate the vortical structure of the strained wakes.

Many free shear flows, once developed, are observed to evolve self-similarly, with the mean profiles of the various statistics maintaining the same shape as the flow evolves. The profiles can thus be collapsed when scaled by a varying magnitude and width. Scaled mean flow profiles are often fairly universal in shape, whereas those for turbulent statistics are found to be more dependent on the particular conditions used to generate the flow (e.g. Wygnanski *et al.* 1986; George 1989). Analysis of experimental measurements in strained wake flows by Reynolds (1962) and Keffer

(1965) indicates that while the profile shapes may be self-similar, magnitudes and widths of these profiles do not evolve as predicted by classical self-similar analysis.

Examination of the equations governing the evolution of time-developing strained plane wakes indicates the possibility of self-similar evolution. The classical self-similar analysis, which assumes that all of the terms in the governing equations are proportional to each other, leads to a unique self-similar solution if the viscous terms in the mean momentum and Reynolds stress evolution equations are neglected. For a given strain time history, the analytical integral mass flux deficit constraint (2.26) defines how the product of the wake peak mean velocity deficit, U_m, and the wake width, b, must evolve. For the classical self-similar solution, the ratio of these two quantities, the wake shear rate, must exhibit the same time-evolution behaviour as the applied strain rate. These two constraints then determine the behaviour required of U_m and b. Additionally, the classical self-similar solution requires that all components of the Reynolds stress tensor scale with the square of the velocity deficit U_m, the associated anisotropies being constant. For the constant applied strain rates considered here, this solution requires exponential evolution of the wake width b, the wake peak velocity deficit U_m, and the magnitude of the Reynolds stresses K_{ij}. This solution is completely analogous to that found by previous investigators studying spatially developing strained plane wakes.

Although intuitively appealing, this self-similar evolution is not internally consistent for all strain geometries and does not describe the flow evolution observed in the direct numerical simulations or in experimental work on the same flows. It is common practice in self-similar analyses of high-Reynolds-number free shear flows to neglect the viscous terms in the governing equations (there are no walls in the flow). For unstrained wakes this is not necessary because the flow Reynolds number is constant and the viscous terms scale like the other terms in the governing equations. For strained wakes, however, the classical self-similar solution results in viscous terms that have an exponential time dependence, as can be seen from equations (2.52) and (2.50). If the strain-rate difference $a_{11} - a_{22}$ is negative, initially small viscous terms will remain small relative to the other terms in the equation. On the other hand, if $a_{11} > a_{22}$, the viscous terms will grow exponentially and at some point a balance with the other terms will not be possible. The classical self-similar solution also fails if $a_{11} + a_{22} = 0$. In this case, the classical scaling yields time-derivative and advection terms in the mean momentum equation that sum to zero, with a balance between the remaining Reynolds shear stress derivative and viscous terms being impossible.

The above considerations make it clear that if a self-similar evolution is to be sustained for strained wakes, it must be different from the classical solution, at least for strain geometries with $a_{11} > a_{22}$ or $a_{11} + a_{22} = 0$. Thus solutions of greater generality must be found. The assumption that each of the terms in the various evolution equations grows at the same rate as each of the other terms is too limiting, and alternative similarity solutions must be sought that make a balance possible by grouping terms in the equations. Two such generalized 'equilibrium similarity solutions' are derived in §2.2.2.

Scaling the mean velocity profiles from each of the numerical simulations by the time-varying peak deficit magnitude and half-width indicates that the shape of the wake mean velocity profile is nearly universal and described well by the unstrained wake profile $f(\eta) = -\exp(-2.548\eta^2 - 0.896\eta^4)$ reported by Wygnanski *et al.* (1986), where $f(\eta)$ is the self-similar shape function defined by equation (2.24). This profile is similar to a Gaussian, but decays slightly faster to zero at the edges of the wake. Universality of the mean profile shape has also been found in a broad variety

of experimental measurements in 'strained' wake flows (e.g. Reynolds 1962; Hill *et al.* 1963; Gartshore 1967; Narasimha & Prabhu 1972; Elliott & Townsend 1981; Nakayama 1987; Nayeri *et al.* 1996; Beharelle *et al.* 1996 and others). Because this shape represents the form of the mean velocity profile well, the problem of describing the mean flow evolution is reduced to determining the time evolution of the peak velocity deficit magnitude U_m and the wake width b. The universality of $f(\eta)$ also implies that the product of the two scales U_m and b is well-described throughout the flow evolution by equation (2.26) or, for constant strain rate, equation (2.32).

Substituting the self-similar form (2.24) into the mean momentum equation makes it possible to combine all the terms arising from the time-derivative and advection terms into a time-evolving amplitude multiplied by a single function of the scaled cross-stream variable η. Thus, instead of requiring four terms to be proportional to the Reynolds shear stress derivative as in the classical self-similar analysis, only a single term must be balanced. Substitution of assumed similarity forms into the Reynolds stress equation also suggests groupings of terms that can be combined when seeking a balance. Part of the time-derivative term is grouped with the advection term, whereas the rest is lumped with the 'production' of Reynolds stress by the applied strain. These two combinations must then balance with the wake shear production, the viscous diffusion, and the combination of the turbulent transport, pressure–strain, and dissipation. Combining these groups of terms results in the removal of several constraints on the classical self-similar analysis and yields equilibrium similarity solutions that have free parameters (D_1, D_2 and D_3 for solution (2.54) and E_1, E_2 and E_3 for solution (2.55)), rather than unique similarity solutions.

The first equilibrium similarity solution (2.54) arises by considering a wake spreading rate that makes the combination of the time-derivative and advection terms zero. This necessitates a balance between the only remaining terms in the mean momentum equation: the shear stress derivative and the viscous term. By construction this similarity solution thus results in a viscous term that scales like the other term in the mean momentum equation. The other equilibrium similarity solution (2.55) results from assuming that the combination of the time-derivative and advection terms scales like the shear-stress-derivative term. For the choice $E_2 = \frac{1}{2}$ the viscous term in the mean momentum equation scales in the same way and it is therefore not necessary to assume this term is negligible. The viscous term also scales like the other terms at long times for any choice of E_2 if the strain rate a_{22} is positive. From the simulation results, it is found that $E_2 = \frac{1}{2}$ for cases with $a_{22} \leqslant 0$, suggesting that for physical similarity solutions it is important for the viscous terms to be retained in the analysis.

The viscous diffusion of Reynolds stress is found to be negligibly small in the simulated strained wakes, but the classical self-similar analysis has the same difficulties with this term as it did with the viscous term in the mean momentum equation, namely that exponential growth of the viscous diffusion terms prevents a balance at long times when $a_{11} > a_{22}$. For the equilibrium similarity solution (2.54) there are also limitations on the strain rates that will permit the viscous diffusion terms to be balanced by other terms in the Reynolds stress evolution equation. For the equilibrium similarity solution (2.55) the choice $E_2 = \frac{1}{2}$ (or any E_2 for $a_{22} > 0$) ensures that the viscous diffusion terms can always be balanced. As with the viscous term in the mean momentum equation, this choice of E_2 ensures that the viscous diffusion terms are proportional to the other terms in the equation, even if small.

For the second equilibrium similarity solution (2.55), the first bracketed time-evolution terms in both the mean momentum equation (2.49) and the Reynolds stress transport equation (2.50) are the same and not equal to zero. Thus all the terms in the

mean momentum equation and each of the Reynolds stress equations are proportional to each other for self-similarity. The viscous terms in both equations scale in the same way and ensuring that they balance in one equation will ensure that they balance in the other. If the turbulent transport, pressure–strain, and dissipation terms all individually scale like the other terms in the equation, then all of the pressure–strain terms $\Pi_{\alpha\beta}/K_{\alpha\beta}$ should scale in the same way. Combined with the pressure strain condition (2.42), this requires that the normal Reynolds stresses all scale in the same way. This is not, in general, observed in the simulations, suggesting that it is only the combination of the pressure–strain, turbulent transport, and dissipation terms that scales like the other groupings of terms in the Reynolds stress equation, not these terms individually.

This is not necessarily the case for the first equilibrium similarity solution (2.54), which results from the first bracketed time-evolution term in the mean momentum and Reynolds stress equations being zero. This uncouples the different equations from each other and the bracketed time-evolution terms from one equation do not scale like those in the other equations. Because of this, the $\Pi_{\alpha\beta}/K_{\alpha\beta}$ ratios are not necessarily proportional and the condition (2.42) does not force the different normal Reynolds stresses to all remain in proportion to each other. However, this equilibrium similarity solution also can be further generalized if the pressure–strain, turbulent transport, and dissipation terms are only required to scale when considered together rather than individually. In this case no constraint of any kind needs to be imposed on the form of two of the normal Reynolds stresses, K_{22} and K_{33}.

The mathematical existence of self-similar solutions does not ensure that they will be realized in practice, and the direct numerical simulation results must be used to determine which, if any, of the similarity solutions describes the observed flow evolution. As noted above, the scales U_m and b do not, in general, evolve as predicted by the classical solution. The Reynolds stresses for all the simulated flows do not scale with U_m^2 (except perhaps at long times for case E, in which the strain decreases in significance relative to the wake shear) and the Reynolds stress anisotropies are not constant, with individual Reynolds stress terms not even being in constant ratio with the turbulent kinetic energy, let alone with U_m^2. This continued variation of the Reynolds stress anisotropies is in agreement with experiments (Keffer 1965) and with results of strained homogeneous turbulence (Tucker & Reynolds 1968; Marechal 1972).

Instead of changing as predicted by the classical self-similar solution, the strained wake widths respond to the strain in the cross-stream direction. If the cross-stream direction is compressed, the wake width becomes approximately constant. If the cross-stream direction is stretched, then the wake ultimately spreads exponentially at the same rate as predicted by a simple 'box distortion' of the flow by the mean strain. If the cross-stream direction is unstrained, the wake spreads at about the same rate as in the corresponding unstrained flow. This behaviour is correctly predicted by the second equilibrium similarity solution (2.55) for all the cases examined and also correctly predicted by the first equilibrium similarity solution (2.54) when $a_{22} > 0$.

Given the above behaviour of the wake width and the similarity of the mean velocity profile, the integral constraint (2.26) can be used to determine the behaviour of the wake velocity deficit. Knowing how the wake width and velocity deficit evolve, one can predict the evolution of the wake shear. For most strain geometries this shear decays (e.g. $n_U - n_b < 0$, see table 3) and the flows approach pure straining flows. In one case simulated (case E), the shear increases and the constant applied strain should eventually become insignificant. This flow ultimately exhibits similarities to unstrained wakes, as discussed in §4.1.3. For two strain geometries (cases C and G),

the wake width and velocity deficit change at the same rate, implying a constant wake shear rate.

The mean strain has a strong impact on the evolution of the mean velocity profile, causing either the width or the deficit (or both) to change exponentially (the exception being case G, the axisymmetric strain case designed with the hope of achieving statistical stationarity). However, even at lower strain rates, the turbulence is unable to keep pace with the changing mean velocity deficit. The ratio of the turbulent kinetic energy to U_m^2 is not constant (except perhaps at late times for case E, in which the importance of the applied strain is decreasing in time). Although the kinetic energy levels do tend to increase or decrease along with the increase or decrease of U_m^2, they do not change as rapidly, and during the course of each simulation the turbulent kinetic energy varies at most by a factor of about five, compared to a factor of up to over 5000 (case D) for U_m^2.

The similarity analysis that leads to the above equilibrium similarity solutions also requires that the Reynolds stress profiles evolve self-similarly according to equation (2.28*a*), namely that the profile shapes are the same up to a time-dependent amplitude K_{ij} and have a width proportional to that of the mean velocity profile. While the latter assumption is found to accurately describe the results of both the numerical simulations and the experimental data, the first is not completely achieved by all the Reynolds stress components for all the various strain geometries considered. Despite this, equation (2.28*a*) does at least roughly describe the observed behaviour in nearly all instances by the end of the simulations. Given this poorer agreement with the basic similarity assumption, it is not surprising that the computational Reynolds stress results do not agree perfectly with the those predicted by similarity analysis. Nonetheless, the equilibrium similarity solutions do a reasonable job of describing the different evolutions of the various Reynolds stress components, at least asymptotically, in contrast to the classical self-similar solution, which incorrectly predicts that all the Reynolds stresses scale like U_m^2.

The relative magnitude of the dissipation rate of kinetic energy for the different cases is similar to that of the kinetic energy, resulting in turbulence time scales q^2/ϵ that are nearly independent of strain geometry and strain rate. During the course of the simulations, this time scale differs from that of the corresponding unstrained wake by less than a factor of two. Unlike the other turbulence statistics examined, the variation of this time scale with total strain shows wide scatter for flows strained at different rates. These data are better collapsed by simply plotting against the simulation time rather than total strain, again indicating that the turbulence time scale is only weakly affected by the imposed strain. This time scale cannot be too closely tied to the mean wake shear either, however, since this shear rapidly decreases in many cases without affecting the q^2/ϵ evolution. Apparently the initial conditions have a lasting impact on the turbulence, with the turbulence being slow to respond to the changes in the mean flow rapidly brought about by the applied strain. This slow response by the turbulence to the changes in the mean flow may partly explain why Townsend (1980) found that the linearized rapid-distortion equations do a good job in predicting the Reynolds stress anisotropy development in the strained wake experiment of Elliott & Townsend (1981).

As observed for strained homogeneous turbulence, compression in a particular coordinate direction leads to dominance of the velocity fluctuation component in that direction as a result of turbulence production by the applied strain. This is particularly apparent in flows with spanwise compression, which ultimately have virtually all of the turbulent kinetic energy in the spanwise component. It is less apparent in case E, in

which the mean wake shear increases in time and the strain becomes proportionately less significant. The strain 'production' term acts as a destruction term for velocity components in directions of mean expansion, and the relative magnitude of such components is reduced.

With the exception of the turbulence time scale, the response of the turbulence to different rates of strain is reasonably well collapsed by plotting against total strain, at least for the strain geometry considered in §4.3. For a given value of total strain, reducing the strain rate results in increased wake thickness, decreased mean velocity deficit, and decreased normal Reynolds stresses levels.

The vortical structure of the turbulence in the strained wakes depends on the geometry of the imposed strain. Compression in the cross-stream direction results in wakes of constant width, with relatively few vortical eddies spanning the width of the flow. Nearly irrotational fluid can be found across the entire flow at many streamwise locations. If the wake is also stretched in the spanwise direction, like-sign spanwise vorticity tends to amalgamate and create a more organized wake structure. Conversely, flows that are stretched in the cross-stream direction contain many small-scale vortical structures with little large-scale organization. When such flows are also compressed in the streamwise direction a relatively irrotational zone develops near the wake centreline, particularly for slower strain rates. The vortical structure of flows with no cross-stream strain is similar to that of the unstrained wake.

In summary, strained wakes apparently do evolve self-similarly, but in accordance with equilibrium similarity solutions that are more complicated than the classical self-similar solution, in which each term is required to scale like all the others. Profiles of the various statistical quantities do develop a self-similar shape and can be reasonably collapsed by scalings of magnitude and width. The observed behaviour in the numerical simulations suggests that groups of terms in the governing equations combine to make a balance possible. The pressure–strain term in the Reynolds stress transport equation apparently does not, in general, scale like the other terms in the equation, but rather scales only in combination with the turbulent transport and dissipation terms. The similarity solutions that are consistent with the numerical results have the property that the viscous terms can be retained in the similarity analysis because they scale like the other terms in the equations. Thus despite being small, these terms maintain the same relative importance throughout the self-similar evolution. The wake mean velocity profile shape is found to be universal and the fairly rapid changes in magnitude and width brought about by the applied strain are well-predicted by the generalized equilibrium similarity solutions. The impact of the applied strain on the turbulence, however, is slower to reach a self-similar state and less pronounced than the impact on the mean flow scales U_m and b. This suggests that the flow evolution may be affected by the initial conditions of the turbulence for a relatively long time.

Appendix A. Self-similarity for flows with time-varying strain rate

Although self-similar evolution will not be achieved if the strain rate varies arbitrarily in time, there are functional forms of $a_{ij}(t)$ that do permit the possibility

of self-similar evolution. These correspond to the temporally evolving analogues of spatially evolving plane wakes with free-stream velocities that vary as $U_1 \propto (1 - \xi x)^m$, with ξ being constant. The pressure gradient in such flows can be determined from the Bernoulli equation to be

$$\frac{dC_p}{dx} = \frac{d\bar{P}/dx}{\frac{1}{2}\rho(U_1^0)^2} = 2m\xi(1 - \xi x)^{2m-1}, \tag{A 1}$$

where U_1^0 is the positive free-stream velocity at $x = 0$.

Converting the above spatial variation of free-stream velocity to a temporal variation of strain by computing $a_{11} = \partial U_1/\partial x$ in a frame moving with velocity $U_1(x)$ we have

$$a_{11} = \frac{1}{((1-m)/m)t + t_0}, \quad t_0 = \frac{-1}{mU_1^0\xi}, \tag{A 2}$$

with $a_{22} = -a_{11}$ and $a_{33} = 0$. The sign of t_0 (and $m\xi$) depends on the sign of the pressure gradient, with positive t_0 (negative $m\xi$) associated with favourable pressure gradients and negative t_0 (positive $m\xi$) resulting from adverse pressure gradients. Substituting this time-varying strain into equation (2.26), one can show that

$$U_s(t)\delta(t) = U_s^0\delta^0 z(t)^{\frac{2m}{m-1}} \quad \text{where} \quad z(t) = 1 + \left(\frac{1-m}{m}\right)\frac{t}{t_0} = \frac{1}{t_0 a_{11}(t)}. \tag{A 3}$$

Not surprisingly, one can use the mean momentum equation (2.27) and the Reynolds stress transport equation (2.29) to show that

$$\delta(t) = \delta^0 z(t)^{D_\delta}, \quad U_s(t) = U_s^0 z(t)^{D_M}, \quad K_{ij}(t) = K_{ij}^0 z(t)^{D_{ij}}, \tag{A 4}$$

for the bracketed time-varying terms in these equations to be proportional. As with the case of constant strain rate considered in §2.2, the solution for the various exponents arises from the constraints provided by the integrated mean momentum equation, the Reynolds shear stress term in the mean momentum equation, the shear production terms in the $\overline{u_1'^2}$ and $\overline{u_1'u_2'}$ equations, and the pressure–strain condition (2.31b). For this form of time-varying strain rate, these constraints lead to a 'classical' self-similar solution of the form

$$D_\delta = \frac{3m-1}{2(m-1)}, \tag{A 5a}$$

$$D_M = \frac{m+1}{2(m-1)}, \tag{A 5b}$$

$$D_{11} = D_{22} = D_{33} = D_{12} = \frac{m+1}{m-1}. \tag{A 5c}$$

Note that, as in the constant-strain-rate case, the mean shear rate U_s/δ associated with the wake remains proportional to the time-varying strain rate and all the Reynolds stresses grow at the same rate. The solution (A 5) is invalid when $m = 1$. However, for $m = 1$ the strain given by equation (A 2) is constant and the appropriate solutions are given in §2.2. The case $m = 0$ corresponds to the classical solution for an unstrained wake.

For this case of time-varying strain rate, equations (2.49) and (2.50) remain unchanged except that a_{11} and a_{22} are not constant, but time-dependent and given by

equation (A 2). Substituting the solution (A 5) into equation (2.49) yields

$$\left[\frac{(1-m)a_{11}}{2m}\right]\eta f(\eta) + \left[\frac{K^0_{12}t_0 a_{11}}{U^0_s \delta^0}\right]k_{12}(\eta) = -\nu\left[\frac{1}{(\delta^0)^2}(t_0 a_{11})^{\frac{3m-1}{m-1}}\right]\frac{\mathrm{d}f}{\mathrm{d}\eta}. \qquad (A\,6)$$

Unlike the constant-strain-rate case, the first term of this equation cannot be zero because $m \neq 1$. The viscous term scales like the other terms in the equation only for the unstrained case $m = 0$. For favourable pressure gradients the viscous term grows faster than the other terms and no balance can be achieved for long times, indicating that this self-similar solution is not sustainable except for adverse pressure gradients ($a_{11} < 0$).

As with the constant-strain-rate case, an equilibrium similarity solution exists in which the first term in equations (2.49) and (2.50) is zero. In this case $D_\delta = D_M = m/(m-1)$ and $D_{12} = 0$, corresponding to the wake shear being constant. If the pressure–strain condition (2.42) is to be satisfied, then the $\Pi_{\alpha\alpha}$ terms are constant and the normal Reynolds stresses are given by the three-parameter family (F_1, F_2, F_3) of solutions given by

$$K_{11}(t) = F_1 z(t) + (K^0_{11} - F_1)z(t)^{\frac{2m}{m-1}}, \qquad (A\,7a)$$

$$K_{22}(t) = F_2 z(t) + (K^0_{22} - F_2)z(t)^{\frac{-2m}{m-1}}, \qquad (A\,7b)$$

$$K_{33}(t) = K^0_{33} + F_3 t/t_0. \qquad (A\,7c)$$

If the pressure–strain terms scale like the other terms in the normal Reynolds stress equations only when combined with the dissipation and/or transport terms, then $K_{22}(t)$ and $K_{33}(t)$ are completely undetermined by similarity constraints, while K_{11} retains the above form. Requiring that the viscous diffusion terms remain smaller than the other terms in the Reynolds stress equations limits the possible values of m and ξ for which sustained similarity solutions exist ($m \geqslant -1$ for $\xi > 0$ and $m \leqslant -1$ for $\xi < 0$).

A second equilibrium similarity solution, in which the first two terms of equations (2.49) and (2.50) are proportional, also exists. In this case, as with the constant-strain-rate flow, the pressure–strain rate terms must combine with the turbulent transport and dissipation terms to scale with the other terms in the equation. The generalized equilibrium similarity solution for this case is a two-parameter family (F_1, F_2) of solutions given by

$$q(t) = \frac{F_1 - 1}{F_1 z(t)^{\frac{m+1}{m-1}} - 1}, \quad a_{11} = -a_{22} = \frac{1}{t_0 z(t)}, \qquad (A\,8a)$$

$$\frac{\delta(t)}{\delta^0} = q(t)^{F_2}z(t)^{\frac{m}{m-1}}, \quad \frac{U_s(t)}{U^0_s} = q(t)^{-F_2}z(t)^{\frac{m}{m-1}}, \quad \frac{K_{12}(t)}{K^0_{12}} = q(t), \qquad (A\,8b)$$

$$\frac{K_{11}(t)}{K^0_{11}} = q(t)^{-2F_2}z(t)^{\frac{2m}{m-1}}, \quad \frac{K_{22}(t)}{K^0_{22}} = q(t)^{2F_2+2}z(t)^{\frac{-2m}{m-1}}, \quad \frac{K_{33}(t)}{K^0_{33}} = q(t). \qquad (A\,8c)$$

For this solution the wake shear does not scale like the applied strain rate and the Reynolds stresses scale differently from each other for non-zero strain. For the viscous terms to scale like the other terms in the equations, F_2 must equal $-\frac{1}{2}$. Note that this value of F_2 also makes the exponent on the $q(t)$ terms in all the Reynolds stress terms 1. This choice of F_2 is analogous to the selection $E_2 = \frac{1}{2}$ in the constant-strain-rate case, namely this is the only value of F_2 that ensures both a wake width reduction under compression ($a_{22} < 0$) as well as viscous terms that do not outgrow the other terms in the governing equations.

A case of practical interest occurs when $m = \frac{1}{2}$. For this value of m the pressure gradient given by equation (A 1) is constant, as in the spatially evolving flows studied experimentally by Liu *et al.* (1999). The strain rate evolution corresponding to this constant streamwise pressure gradient is

$$a_{11} = \frac{1}{t + t_0}, \quad a_{22} = -a_{11}, \quad a_{33} = 0. \tag{A 9}$$

Thus in these experiments the effective strain rate increases in magnitude (becomes more negative) with downstream distance in adverse pressure gradients ($t_0 < 0$), while for favourable pressure gradients ($t_0 > 0$) it decreases with downstream distance. The classical solution (A 5) reduces to

$$D_\delta = -\tfrac{1}{2}, \quad D_M = -\tfrac{3}{2}, \tag{A 10a}$$

$$D_{11} = D_{22} = D_{33} = D_{12} = -3, \tag{A 10b}$$

while the similarity solution (A 8) (with $F_2 = -\frac{1}{2}$) becomes

$$z(t) = \frac{t_0 + t}{t_0}, \quad q(t) = \frac{F_1 - 1}{F_1 z(t)^3 - 1}, \tag{A 11a}$$

$$\frac{\delta(t)}{\delta^0} = q(t)^{-1/2} z(t)^{-1}, \quad \frac{U_s(t)}{U_s^0} = q(t)^{1/2} z(t)^{-1}, \tag{A 11b}$$

$$\frac{K_{12}(t)}{K_{12}^0} = \frac{K_{33}(t)}{K_{33}^0} = q(t), \quad \frac{K_{11}(t)}{K_{11}^0} = q(t)z(t)^{-2}, \quad \frac{K_{22}(t)}{K_{22}^0} = q(t)z(t)^2. \tag{A 11c}$$

According to this similarity solution, δ should increase like $t^{1/2}$ for large times, whereas it is expected to decay like $t^{-1/2}$ for the classical solution. Examination of the experimental data shows that the wake widths increase in all cases, albeit minimally for the strong favourable pressure gradient case. Thus, at least for this time-varying strain-rate case, the equilibrium similarity solution (A 8) better describes the evolution of the mean velocity field, as was found for the constant-strain-rate cases.

REFERENCES

ATSAVAPRANEE, P. & GHARIB, M. 1994 A plane mixing layer with cross-shear. *Phys. Fluids* **6**, 2880–2882.

ATSAVAPRANEE, P. & GHARIB, M. 1997 Structures in stratified plane mixing layers and the effects of cross-shear. *J. Fluid Mech.* **342**, 53–86.

BEHARELLE, S., NAYERI, C. N., DELVILLE, J., BONNET, J. P. & FIEDLER, H. E. 1996 Influence of the transverse shear on the development of wake flows. In *Advances in Turbulence VI* (ed. S. Gavrilakis, L. Machiels & P. A. Monkewitz), pp. 511–512. Kluwer.

CASTILLO, L. & GEORGE, W. K. 2001 Similarity analysis for turbulent boundary layer with pressure gradient: outer flow. *AIAA J.* **39**, 41–47.

COLEMAN, G. N., KIM, J. & SPALART, P. R. 2000 A numerical study of strained three-dimensional wall-bounded turbulence. *J. Fluid Mech.* **416**, 75–116.

CORRAL, R. & JIMENEZ, J. 1995 Fourier/Chebyshev methods for the incompressible Navier–Stokes equations in infinite domains. *J. Comput. Phys.* **121**, 261–270.

ELLIOTT, C. J. & TOWNSEND, A. A. 1981 The development of a turbulent wake in a distorting duct. *J. Fluid Mech.* **113**, 433–467.

GARTSHORE, I. S. 1967 Two-dimensional turbulent wakes. *J. Fluid Mech.* **30**, 547–560.

GEORGE, W. K. 1989 The self-preservation of turbulent flows and its relation to initial conditions and coherent structure. In *Advances in Turbulence* (ed. W. K. George & R. Arndt), pp. 39–73. Hemisphere.

GEORGE, W. K. 1995 Some new ideas for similarity of turbulent shear flows. In *Turbulence, Heat and Mass Transfer* (ed. K. Hanjalic & J. C. F. Pereira), pp. 13–24. Begell House.

GEORGE, W. K. & CASTILLO, L. 1997 Zero-pressure-gradient turbulent boundary layer. *Appl. Mech. Rev.* **50**, 689–729.

GHOSAL, S. & ROGERS, M. M. 1997 A numerical study of self-similarity in a turbulent plane wake using large-eddy simulation. *Phys. Fluids* **9**, 1729–1739.

HILL, P. G., SCHAUB, U. W. & SENOO, Y. 1963 Turbulent wakes in pressure gradients. *Trans. ASME* E: *J. Appl. Mech.* **30**, 518–524.

HOFFENBERG, R., SULLIVAN, J. P. & SCHNEIDER, S. P. 1995 Wake measurements in a strong adverse pressure gradient. *AIAA Paper* 95-1912.

KAMBE, T. & MINOTA, T. 1983 Acoustic wave radiated by head-on collision of two vortex rings. *Proc. R. Soc. Lond.* A **386**, 277–308.

KEFFER, J. F. 1965 The uniform distortion of a turbulent wake. *J. Fluid Mech.* **22**, 135–159.

KEFFER, J. F. 1967 A note on the expansion of turbulent wakes. *J. Fluid Mech.* **28**, 183–193.

KEFFER, J. F., KAWALL, J. G., HUNT, J. C. R. & MAXEY, M. R. 1978 The uniform distortion of thermal and velocity mixing layers. *J. Fluid Mech.* **86**, 465–490.

LIN, S. J. & CORCOS, G. M. 1984 The mixing layer: deterministic models of a turbulent flow. Part 3. The effect of plane strain on the dynamics of streamwise vortices. *J. Fluid Mech.* **141**, 139–178.

LIU, X., THOMAS, F. O. & NELSON, R. C. 1999 An experimental investigation of wake development in arbitrary pressure gradients. *AIAA Paper* 99-677.

MARECHAL, J. 1972 Etude experimentale de la deformation plane d'une turbulence homogene. *J. Méc.* **11**, 263–294.

MOSER, R. D., ROGERS, M. M. & EWING, D. W. 1998 Self-similarity of time-evolving plane wakes. *J. Fluid Mech.* **367**, 255–289.

NAKAYAMA, A. 1987 Curvature and pressure-gradient effects on a small-defect wake. *J. Fluid Mech.* **175**, 215–246.

NARASIMHA, R. & PRABHU, A. 1972 Equilibrium and relaxation in turbulent wakes. *J. Fluid Mech.* **54**, 1–17.

NAYERI, C., BEHARELLE, S., DELVILLE, J., BONNET, J. P. & FIEDLER, H. E. 1996 Experimental investigation of the axisymmetric shear layer between coaxial jets with swirl. In *Advances in Turbulence VI* (ed. S. Gavrilakis, L. Machiels & P. A. Monkewitz), pp. 473–476. Kluwer Academic Publishers.

OBERLACK, M. 2000 Symmetrie, Invarianz und Selbstähnlichkeit in der Turbulenz. Habilitation Thesis, RWTH Aachen, Shaker Verlag.

PRABHU, A. & NARASIMHA, R. 1972 Turbulent non-equilibrium wakes. *J. Fluid Mech.* **54**, 19–38.

REYNOLDS, A. J. 1962 Observations on distorted turbulent wakes. *J. Fluid Mech.* **13**, 333–355.

REYNOLDS, A. J. & TUCKER, H. J. 1975 The distortion of turbulence by general uniform irrotational strain. *J. Fluid Mech.* **68**, 673–693.

ROGALLO, R. S. 1977 An ILLIAC program for the numerical simulation of homogeneous incompressible turbulence. *NASA TM* 73203.

ROGALLO, R. S. 1981 Numerical experiments in homogeneous turbulence. *NASA TM* 81315.

ROGERS, M. M. & MOSER, R. D. 1994 Direct simulation of a self-similar turbulent mixing layer. *Phys. Fluids* **6**, 903–923.

ROGERS, M. M., MOSER, R. D. & BUELL, J. C. 1990 A direct comparison of spatially and temporally evolving mixing layers. *Bull Am. Phys. Soc.* **35**, 2294.

SMITH, A. M. O. 1975 High-lift aerodynamics. *J. Aircraft* **12**, 501–530.

SPALART, P. R. 1988 Direct simulation of a turbulent boundary layer up to $Re_\theta = 1410$. *J. Fluid Mech.* **187**, 61–98.

SPALART, P. R., MOSER, R. D. & ROGERS, M. M. 1991 Spectral methods for the Navier–Stokes equations with one infinite and two periodic directions. *J. Comput. Phys.* **96**, 297–324.

SREENIVASAN, K. R. 1985 The effect of contraction on a homogeneous turbulent shear flow. *J. Fluid Mech.* **154**, 187–213.

TOWNSEND, A. A. 1954 The uniform distortion of homogeneous turbulence. *Q. J. Mech. Appl. Math.* **7**, 104–127.

TOWNSEND, A. A. 1980 The response of sheared turbulence to additional distortion. *J. Fluid Mech.* **81**, 171–191.

TUCKER, H. J. & REYNOLDS, A. J. 1968 The distortion of turbulence by irrotational plane strain. *J. Fluid Mech.* **32**, 657–673.

UBEROI, M. S. 1956 Effect of wind-tunnel contraction on free-stream turbulence. *J. Aero. Sci.* **23**, 754–764.

WYGNANSKI, I., CHAMPAGNE, F. & MARASLI, B. 1986 On the large-scale structures in two-dimensional, small-deficit, turbulent wakes. *J. Fluid Mech.* **168**, 31–71.

ZHOU, M. D. & SQUIRE, L. C. 1985 The interaction of a wake with a turbulent boundary layer. *Aero. J.* **89**, 72–81.